Liang Shao, M.Eng.

Tire-Road Friction Estimation based on Vehicle Lateral Dynamics

DOCTORAL THESIS

to achieve the university degree of
Doktor der technischen Wissenschaften
submitted to

Graz University of Technology
Institute of Automotive Engineering
Member of Frank Stronach Institute

Assessors:

Assoc.Prof. Dipl.-Ing. Dr.techn. Arno Eichberger
Graz University of Technology, Graz, Austria

Dr. Fredrik Bruzelius
Chalmers University of Technology, Göteborg, Sweden

Graz, November 2018

Acknowledgement

Time flies. After four years of PhD studies, I am on the end of my dissertation. I would like to thank my supervisor Assoc. Prof. Arno Eichberger, who has offered me great help and support during my dissertation. Besides, I also would like to thank Dr. Fredrik Bruzelius for his valuable suggestions on my dissertation.

About the colleagues in my institute, I would like to specially thank Dr. Cornelia Lex, who gives me huge suggestions and helps both in my research and life in Austria. Besides, I express my thanks to Andreas Hackl, Martin Schabauer, Branko Rogic, Sajjad Samiee for their help in my research and life.

I also would like to thank my friend Dr. Chi Jin for his regular discussions and suggestions in the research.

I also would like to thank Chinese Scholarship Council for supporting me to conduct my PhD in Austria.

Finally, I express my gratitude to my parents, girl friend and other friends for their great patience and encouragement.

Statutory Declaration

Ich erkläre an Eides statt, dass ich die vorliegende Arbeit selbstständig verfasst, andere als die angegebenen Quellen/Hilfsmittel nicht benutzt, und die den benutzten Quellen wörtlich und inhaltlich entnommenen Stellen als solche kenntlich gemacht habe.

Graz, am ....
(Unterschrift)

I declare that I have authored this thesis independently, that I have not used other than the declared sources / resources, and that I have explicitly marked all material which has been quoted either literally or by content from the used sources.

....
(date) (signature)

Abstract

Many traffic safety related investigations show a correlation between the tire-road friction coefficient (TRFC) and accidents probability. The accurate information of this TRFC can significantly enhance the performance and reliability of existing vehicle-safety related functions like Electric Stability Control (ESC). Besides, as automated vehicles develope, the automated systems, instead of the driver, should be responsible for adapting the driving style like braking, steering to the TRFC. Therefore, TRFC estimation is increasingly critical for modern vehicles. This dissertation describes the development of observers for estimating TRFC based on vehicle lateral dynamics with sensors available on the current mass-produced vehicles. The proposed observers should be real time capable and asymptotically stable in a wide range of vehicle operations.

This study presents two branches of methods for TRFC estimation depending on the availability of tire self-aligning torque (TSAT). The first branch contains two methods with TSAT information: the **method I** is a nonlinear adaptive observer with an indirect measurement based on estimated total aligning torque and front axle tire lateral force, while the **method II** proposes a more advanced nonlinear adaptive observer with no need to estimate front axle lateral force. In the second branch, a **method III** without TSAT information is presented. This method proposes an optimization based observer, with guarantee on real time capability and finding the global optima.

Simulations and experiments for the first branch among **method I** and **method II** as well as Extended Kalman Filter (EKF) (as a comparison), show that **method I** and **method II** can guarantee stability of TRFC estimation in a wider range of vehicle operations than EKF. Besides, in terms of root mean square of TRFC estimation error, **method I**, **method II** and EKF (in stable situations) have similar performance. In the second branch, **method III** and a linearization based observer (lbo) (as a comparison) illustrate that the **method III** performs better than lbo (in stable situations) w.r.t. root mean square of TRFC estimation error and can always guarantee stability in a wide range of vehicle operations while lbo cannot.

Kurzfassung

Verschiedene Studien zeigen einen Zusammenhang zwischen dem maximalen Kraftschluss zwischen Reifen und Fahrbahn und der Unfallwahrscheinlichkeit. Die Kenntnis des maximalen Kraftschlusses kann die Leistungsfähigkeit und die Zuverlässigkeit von bestehenden fahrsicherheitsrelevanten Funktionen wie der Elektronischen Stabilitätskontrolle (ESC) erheblich verbessern. Mit steigender Automatisierung von Fahrzeugen müssen diese, wie aktuell der Fahrer oder die Fahrerin, den Fahrstil beim Bremsen und Lenken an den maximalen Kraftschluss anpassen können. Daher nimmt die Schätzung des maximalen Kraftschlusses an Bedeutung für moderne Fahrzeuge zu. Diese Dissertation befasst sich mit der Entwicklung von Beobachtern zur Abschätzung des maximalen Kraftschlusses zwischen Fahrbahn und Reifen auf Basis der Fahrzeugquerdynamik mit verfügbaren Sensoren in aktuellen Serienfahrzeugen. Die vorgeschlagenen Beobachter sollen echtzeitfähig und in weiten Bereichen des Fahrzeugbetriebs asymptotisch stabil sein.

In der vorliegenden Arbeit werden zwei Gruppen solcher Methoden vorgestellt, die sich durch die notwendigen Signaleingänge unterscheiden. Bei der ersten Gruppe von Methoden wird die Verfügbarkeit von Informationen über das Reifenrückstellmoment vorausgesetzt. Zwei verschiedene Schätzer wurden entwickelt: Methode I verwendet einen nichtlinearen adaptiven Zustandsbeobachter mit der indirekten Messung des gesamten Rückstellmoments und der Querkraft an der Vorderachse, wohingegen Methode II einen erweiterten nichtlinearen adaptiven Beobachter verwendet, der keine Schätzung der Querkraft an der Vorderachse benötigt. In der zweiten Gruppe von Methoden, zu der die Methode III dieser Arbeit gehört, wird das Reifenrückstellmoment nicht benötigt. Hier kommt ein optimierungsbasierter Beobachter zum Einsatz, der garantiert echtzeitfähig ist und ein globales Optimum garantiert.

Simulationen und Experimente zeigen, dass Methode I und Methode II im Vergleich mit einem Extended Kalmanfilter (EKF) Stabilität in einem größeren Betriebsbereich garantieren können. Bei einem Vergleich des quadratischen Mittelwerts des Schätzfehlers zeigen sowohl Methode I, Methode II und die Schätzung mit dem EKF vergleichbare

Ergebnisse. Methode III wird mit einem linearisierten Beobachter verglichen. Hier ist der quadratische Mittelwert des Schätzfehlers der Methode III deutlich besser als der Vergleichswert. Stabilität kann bei Methode III immer, während das für die Vergleichsmethode nicht der Fall ist.

Abbreviations

ABS	Anti-Lock Braking System
AEB	Autonomous Emergency Braking
AFS	Active Front Steering
C2C	Car-to-Car
C2I	Car-to-Infrastructure
C2X	Car-to-X
CCO	Circle Criteria based Observer
CTO	Coordinate Transformation based Observer
DE	Differential Evolution
EKF	Extended Kalman Filter
EPS	Electric Power Steering
ESC	Electric Stability Control
FIR	Finite Impulse Response
GDP	Gross Domestic Product
GPS	Global Positioning System
HGO	High Gain Observer
IIO	Immersion and Invariance Observer
LBO	Linearization Based Observer
LMI	Linear Matrix Inequality
MHO	Moving Horizon Observer
MVE	Mean Value of estimation Error
NRLS	Nonlinear Recursive Least Squares
PDE	Partial Differential Equation
PE	Persistent Excitation
PF	Particle Filter
PSO	Particle Swarm Optimization
RLS	Recursive Least Squares
RMS	Root Mean Square
SPR	Strict Positive Real

SMO	Sliding Mode Observer
SQP	Sequential Quadratic Programming
SVM	Support Vector Machine
TRFC	Tire Road Friction Coefficient
TSAT	Tire Self-Aligning Torque
UIO	Unknown Input Observer
UKF	Unscented Kalman Filter
UN	United Nations
WHO	World Health Organization

Symbols

Conventional notations are used to denote estimates and error variables. For a vector z, $\hat{z}$ represents its estimate and $\tilde{z} = z - \hat{z}$ is an error variable. The norm operator $||\cdot||$ denotes the Euclidean norm for vectors and the induced Euclidean norm for matrices. The maximum and minimum eigenvalues of a symmetric matrix P are denoted $\lambda_{\max}(P)$ and $\lambda_{\min}(P)$. For a set $E \subset \mathbb{R}^n$, we write $(E - E) := \{z_1 - z_2 \subset \mathbb{R}^n | z_1, z_2 \subset E\}$.

List of Symbols

a_y	vehicle lateral acceleration
$a_{y,\text{thres}}$	threshold for vehicle lateral acceleration in tire-road friction coefficient estimation
c_z	tire vertical stiffness
d_c	mechanical trail of front tires which is assumed to be the same for both front left and right tires
dY_0	tire initial stiffness
f_f	vehicle front axle lateral force divided by tire-road friction coefficient
f_{fl}	vehicle front left lateral force divided by tire-road friction coefficient
f_{fr}	vehicle front right lateral force divided by tire-road friction coefficient
f_1	derivative of side slip angle
f_2	derivative of yaw rate
F_l	tie rod force in the left side
F_m	maximum horizontal force acting in the wheel ground contact plane
F_r	tie rod force in the right side
F_x	tire longitudinal force
F_y	tire lateral force
F_{yf}	vehicle front axle tire lateral force
F_{yfl}	vehicle front left tire lateral force
F_{yfr}	vehicle front right tire lateral force

$F_{\mathrm{yf,thres}}$	threshold for vehicle front axle lateral force in tire-road friction coefficient estimation
F_{yr}	vehicle rear axle lateral force
F_z	normal force in the wheel plane
F_{zfl}	front left wheel normal force
F_{zfr}	front right wheel normal force
F_{zrl}	rear left wheel normal force
F_{zrr}	rear right wheel normal force
$F_{z,nom}$	nominal tire load
$F_{z,2nom}$	an extra tire load
g	acceleration of gravity
g_f	vehicle front axle tire self-aligning torques divided by tire-road friction coefficient
g_{fl}	vehicle front left tire self-aligning torque divided by tire-road friction coefficient
g_{fr}	vehicle front right tire self-aligning torque divided by tire-road friction coefficient
h_g	height of gravity
I_z	vehicle yaw moment of inertial
J_s	rotational inertia coefficient in the steering system
k_a	observer gain
k_b	observer gain
k_c	positive constant
k_f	positive constant
k_s	damping coefficient in the steering system
k_{vy}	observer gain
$k_{y,low}$	positive constant
$k_{y,upp}$	positive constant
k_μ	observer gain
k_1	observer gain
k_2	observer gain
k_3	observer gain
k_4	observer gain
K_e	observer gain
K_{φ_1}	observer gain
K_{φ_2}	observer gain

l_f	distance between vehicle front axle to the center of gravity
l_{g2}	positive constant
l_r	distance between vehicle rear axle to the center of gravity
l_1	positive constant
l_2	positive constant
l_3	positive constant
l_4	positive variable
l_5	positive constant
l_6	positive variable
l_7	positive variable
l_8	positive variable
L	tire contact length
L_l	vertical distance between the tie rod to the kingpin in the left side
L_r	vertical distance between the tie rod to the kingpin in the right side
m	vehicle mass
m_f	static front axle tire loads
M_z	tire self-aligning torque
M_{zf}	vehicle front axle tire self-aligning torque
M_{zfl}	vehicle front left tire self-aligning torque
M_{zfr}	vehicle front right tire self-aligning torque
n	tire pneumatic trail
$\frac{n}{L}$	tire pneumatic trail divided by tire contact length
$(\frac{n}{L})_0$	initial value of tire pneumatic trail divided by tire contact length
p_1	derivative of vehicle front axle lateral force
p_2	derivative of vehicle rear axle lateral force
p_v	ratio of time when $\frac{p_2}{p_1}$ is within -1 and 3 to overall simulation time during one simulation
Q	covariance of the process noise in EKF
R	covariance of the observation noise in EKF
r_e	wheel effective radius
r_0	unloaded tire radius
s_y^0	overshot tire slip angle
s_y^E	saturated tire slip angle
v_x	vehicle longitudinal velocity
v_y	vehicle lateral velocity
$v_{\omega,x}$	longitudinal velocity component in the wheel contact patch

w_f	front track
w_r	rear track
x_f	front axle tire slip angle above tire-road friction coefficient
x_s	corresponding x_f when tire self-aligning torque comes to zero (not the origin)
x_0	corresponding x_f when tire self-aligning torque comes to the peak point
$x_{f,a}$	threshold for x_f in activating tire-road friction coefficient estimation
$x_{f,c}$	threshold for x_f in outputting estimation result of tire-road friction coefficient
$Y_{\max}$	tire maximum lateral force
Y_∞	tire saturation lateral force
α	tire slip angle
α_f	vehicle front axle tire slip angle
α_r	vehicle rear axle tire slip angle
α_1	positive constant
α_2	positive variable
β	side slip angle
β_l	low boundary of side slip angle
β_r	upper boundary of side slip angle
Γ_1	observer gain
Γ_2	observer gain
δ	front wheel steering angle
δ_a	amplitude of front wheel steering angle
$\Delta\beta_{11}$	discretization interval of side slip angle in Φ
$\Delta\beta_{12}$	discretization interval of side slip angle in Φ
$\Delta\beta_2$	discretization interval of side slip angle in Φ_1
$\Delta\mu_{\max,1}$	discretization interval of tire-road friction coefficient in Φ
$\Delta\mu_{\max,2}$	discretization interval of tire-road friction coefficient in Φ_1
Δt	update period of the optimization result
ϵ	positive constant
ϵ_1	positive constant
ϵ_2	positive constant
λ	wheel slip ratio
$\mu_{\max}$	tire-road friction coefficient
$\mu_{\max,\text{ave}}$	tire-road friction coefficient estimation based on method one
$\mu_{\max,\text{ekf}}$	tire-road friction coefficient estimation based on extended kalman filter

$\mu_{\max,\mathrm{l}}$	low boundary of tire-road friction coefficient
$\mu_{\max,\mathrm{lbo}}$	tire-road friction coefficient estimation based on linearization based method
$\mu_{\max,\mathrm{nao}}$	tire-road friction coefficient estimation based on method two
$\mu_{\max,\mathrm{opti}}$	tire-road friction coefficient estimation based on method three
$\mu_{\max,\mathrm{r}}$	upper boundary of tire-road friction coefficient
$\mu_{\max,\mathrm{real}}$	real tire-road friction coefficient
μ_0	nominal value of tire-road friction coefficient
ρ_1	positive constant
ρ_2	positive constant
ρ_3	positive constant
τ_g	aligning torque caused by tie rod forces
τ_{thres}	threshold for total aligning torque in tire-road friction coefficient estimation
τ_{zf}	total aligning torque in the steering system
φ	vehicle heading angle
Φ	domain of all possible values of side slip angle and tire-road friction coefficient
Φ_1	subset of Φ
ω	vehicle yaw rate
ω_a	wheel angular velocity

Contents

1. Introduction

1.1. Motivation

According to the World Health Organization (WHO), there were about 1.25 million road traffic deaths globally in 2013, with millions more sustaining serious injuries and living with long-term adverse health consequences [2]. Therein, the road fatalities per 100000 inhabitants spread not equally over the world as shown in Fig. 1.1. Actually, 90% of all traffic casualties occur in low- and middle-income countries [2]. Besides, traffic injuries are the leading cause of death among young people who are between 15 and 29 years old, and the economic damage costs governments approximately 3% of Gross Domestic Product (GDP) [2]. To promote solving this global road safety crisis, the lately adopted 2030 Agenda for Sustainable Development in United Nations (UN) has set an ambitious target of "halving the global number of deaths and injuries from road traffic crashes by 2020" (based on 2010) [3].

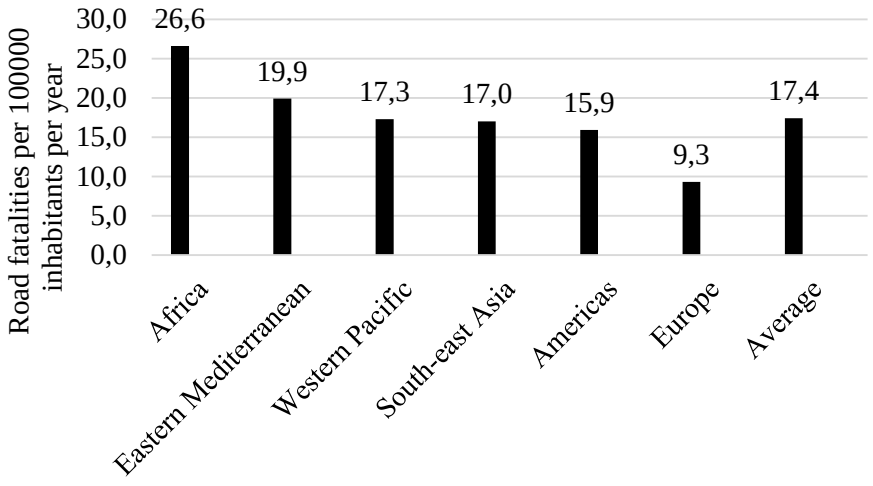

Figure 1.1.: Road fatalities per 100000 inhabitants per year in each area [2].

Traffic-safety related investigations from Wallman [124] demonstrate a correlation between the tire-road friction coefficient (TRFC) ($\mu_{\max}$) and accidents probability: the smaller the TRFC is, the higher the accident rate is. One of the important reasons for this is that the traditional vehicle functions like Autonomous Emergency Braking System (AEB) are developed to prevent accidents on dry road and cannot always avoid accidents under low friction road conditions. Besides, functions like Electronic Stability Control (ESC), Anti-Lock Braking System (ABS) can perform better on icy road if the TRFC can be identified in time. Therefore, the accurate information of the road friction condition can significantly enhance the performance and reliability of existing vehicle functions and thus reduce the accident rate on low friction road condition [26, 50, 79, 125].

Furthermore, with the development of automated vehicles, the responsibility to adapt the driving style like braking, accelerating and steering to the TRFC is transferred from the driver to the automated system. For instance, when the automated vehicle drives on an icy road and plans to conduct a lane change, the current TRFC should be immediately detected and considered by the trajectory planning and tracking process. Similarly, when a pedestrian is detected in the front, the vehicle should be able to brake in time according to the TRFC. As described in [126], for being accepted by society, the automated vehicles need to bring about less traffic accidents than human drivers. Therefore, it is necessary to obtain an accurate TRFC for the development of automated vehicles.

1.2. Thesis objective

The **objective** of this dissertation is the development of different observers for estimating tire-road friction coefficient based on vehicle lateral dynamics with the following criteria:

- Sensors utilized for observers should be based on mass-produced vehicles.
- The asymptotic stability of the observers for $\mu_{\max}$ should be mathematically guaranteed in a wide range of vehicle operations, otherwise, the observers may easily diverge and the TRFC may not be obtained accurately and reliably.
- The whole designed algorithms should be able to run in real time[1].
- The methods should be validated during a variety of driving conditions and maneuvers with simulations and experiments.

[1]The real time capability will only be guaranteed by proposing frameworks and not be systematically tested in this thesis.

The observers will be divided into two branches based on whether the tire self-aligning torque (TSAT) information, obtained by vehicles installed with Electric Power Steering system (EPS) or Active Front Steering system (AFS), is available or not. Such systems providing TSAT can deliver the TRFC information with less excitation from the vehicle than the lateral tire force does. The rest measurements used for all observers in this dissertation are consistently the same, which are the longitudinal velocity, the steering wheel angle and information from ESC (yaw rate, longitudinal and lateral acceleration).

1.3. Outline and contributions

Chapter 1 initially discusses the significance of TRFC estimation for conventional and automated vehicles. Then the objective, outline and contributions of this dissertation are presented.

Chapter 2 starts to describe some basics about TRFC. Then the state-of-the-art of TRFC is provided. Subsequently, based on the objective of this dissertation — TRFC estimation based on vehicle lateral dynamics, methods for nonlinear state and parameter estimation are summarized. After that the technical difficulties of designing observers for TRFC estimation are explained. Finally, the key ideas of how to tackle this nonlinear parameter estimation problem in this dissertation are presented. The main **contributions** of this chapter are:

- Summary of the methods of nonlinear state and parameter estimation.
- Explanation of the difficulties in TRFC estimation based on vehicle lateral dynamics.

Chapter 3 introduces the vehicle model, tire model, as well as the steering system utilized for TRFC estimation. Then, the process of how to implement strain gauge sensors installed on the tie rod to estimate front axle total-aligning torque is demonstrated.

Chapter 4 introduces two methods for estimating TRFC based on tire self-aligning torque.

Method I proposes a framework to estimate TRFC with asymptotic stability and robustness guarantee using the total aligning torque (containing tire self-aligning torque information). Firstly a strategy is adopted by innovatively implementing unknown input observer [94] (UIO) to estimate the front axle lateral force. Then, combined with an indirect measurement based on estimated total aligning torque and front axle lateral force,

a nonlinear adaptive observer is designed to estimate TRFC with asymptotic stability guarantee. To increase the robustness of the estimation result, criteria are proposed to decide when to update the estimated TRFC. The main **contributions** of this method are:

- The relationship between derivative of front axle and rear axle lateral force is analyzed by simulation, based on which an optimized estimation strategy for front axle lateral force is proposed.
- A nonlinear adaptive observer with stability guarantee is proposed to estimate TRFC based on the obtained total aligning torque and estimated front axle lateral force.
- Criteria are proposed to detect excitation level of lateral dynamics and thus used to decide when to update estimated TRFC reliably.

Method II, compared to **Method I**, proposes a nonlinear adaptive observer to observe TRFC with no need to estimate front axle lateral force. Firstly, the vehicle lateral dynamics model is transformed into a lower-triangular form. Then, for non-affine parametrized systems in such a form, a nonlinear adaptive observer is proposed with uniform exponential stability guarantee. Furthermore, the design procedure is applied to the TRFC estimation problem with proper modifications. The main **contributions** of method II are:

- For non-affine parametrized systems in lower-triangular form, a nonlinear adaptive observer is proposed and its estimation error is proved to be uniformly exponentially stable by constructing a strict Lyapunov function.
- The proposed nonlinear adaptive observer is universally applicable if other dynamic systems featuring the same system form (a lower-triangular form) satisfy the corresponding assumptions for this observer.

Finally, TRFC estimation results among **method I** and **method II** as well as Extended Kalman Filter (EKF) (as a comparison) are demonstrated and compared in both simulations and experiments.

Chapter 5 describes a **method III** to estimate TRFC without utilizing tire self-aligning torque information. This method firstly formulate the estimation of side-slip angle and TRFC as an optimization problem. Then, by interweaving discrete time solution of the optimization and continuous integration of sensor data, the proposed method has sufficient time for finding the global optima approximately through adaptive resolution

based grid-search. Finally, the estimation results from the proposed observer and a linearization based observer (lbo) for comparison are demonstrated under various road conditions with simulations and experiments. The main **contributions** of **method III** are:

- An observer is proposed to simultaneously estimate side slip angle and TRFC in real-time regardless of solving a non-convex optimization problem in the observation process.
- The stability of the observer can be guaranteed even when the vehicle lateral dynamics system lacks observability.

Chapter 6 summarizes the research and gives an outlook to enhance the applicability and reliability of TRFC estimation in the future.

2. Background

This chapter firstly describes the definition of tire-road friction coefficient. Then the state of the art about $\mu_{\max}$ estimation is provided. Subsequently, based on the objective of this research, an overview on nonlinear state and parameter estimation is summarized. After that the technical difficulties of designing observers for $\mu_{\max}$ estimation is explained. Finally, this chapter presents solutions about how to tackle this nonlinear parameter estimation problem in this research.

2.1. Basics on tire-road friction coefficient

The tire-road friction coefficient, usually referred as $\mu_{\max}$ in the automotive engineering field, is the ratio of the maximum horizontal force F_m acting in the wheel/ground contact plane to normal force F_z acting in the wheel plane [19], which is represented by

$$\mu_{\max} = \frac{F_m}{F_z}, \tag{2.1}$$

and limited by a friction circle as shown in Fig. 2.1 [14]. The tire road friction coefficient results from complex mechanisms and is normally dependent on some parameters and variables, such as sliding velocity between rubber and contact surface [100].

During purely longitudinal accelerating or braking, only longitudinal force is generated, which is caused by the relative motion between tire and road. Usually, slip ratio is utilized to describe this relative motion and is defined as follows [90]:

$$\lambda = \frac{\omega_a \cdot r_e - v_{w,x}}{|v_{w,x}|} \cdot 100\% \tag{2.2}$$

where λ refers to the slip ratio, ω_a the wheel angular velocity, r_e the wheel effective radius, $v_{w,x}$ the longitudinal velocity component in the contact patch. The relationship between slip ratio, $\mu_{\max}$ and longitudinal force can be described by Fig. 2.2. Under cornering conditions, when the travel direction of the wheel speed shows an angle with respect to

the wheel plane, the tire slip angle α occurs, leading to the generation of tire lateral force F_y and tire self-aligning torque M_z, which respect steady state nonlinear characteristics in relation to the tire slip angle and the tire-road friction coefficient, respectively, see in Fig. 2.3. The acceleration or deceleration maneuvers can also occur during cornering, leading to generation of combined force between longitudinal and lateral directions. This combined force can be expressed by a function of combined slip (combined slip ratio and slip angle) and $\mu_{\max}$, and demonstrates similar characteristics compared to purely longitudinal and lateral ones [90].

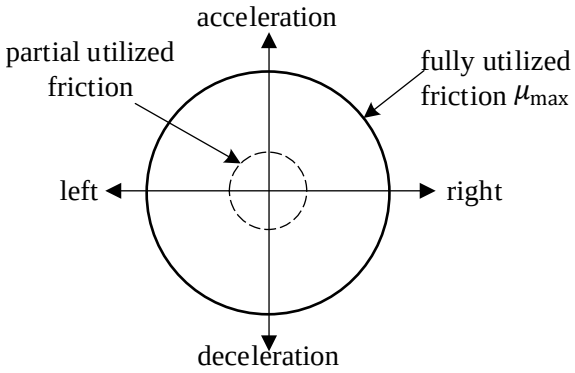

Figure 2.1.: Friction circle of a tire [14].

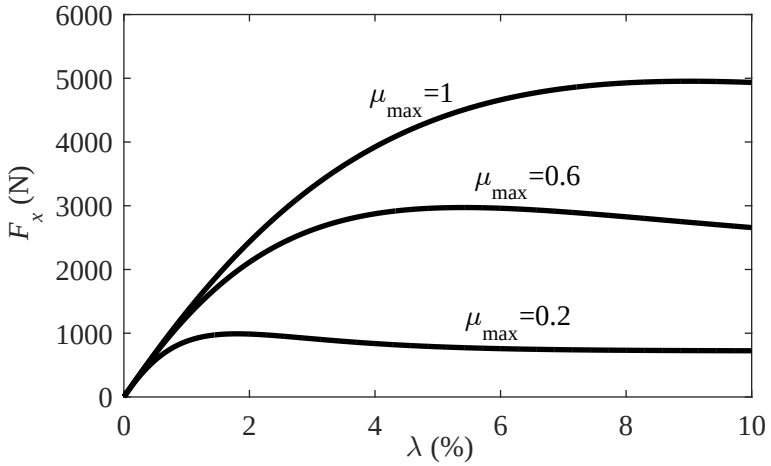

Figure 2.2.: Tire characteristics in longitudinal direction.

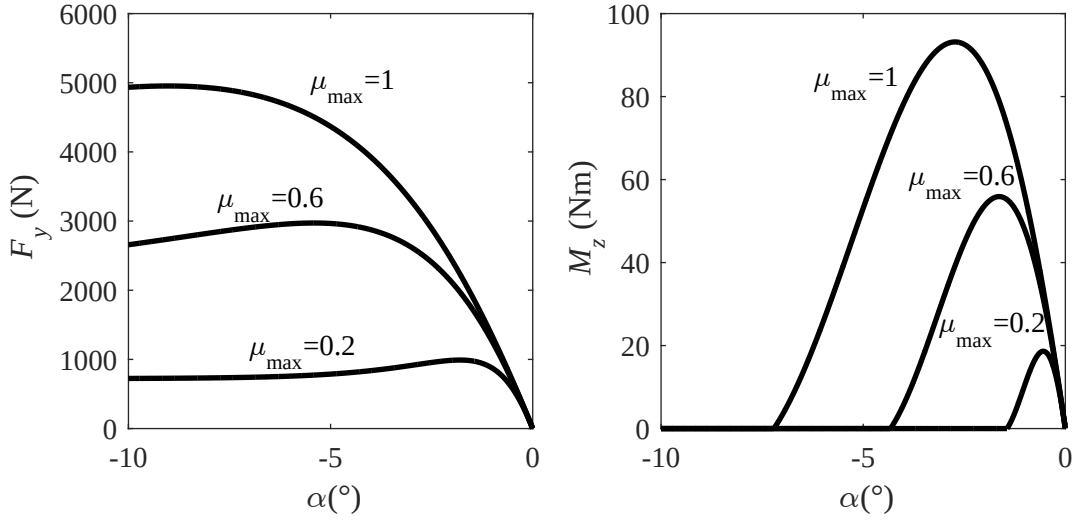

Figure 2.3.: Tire characteristics in lateral direction.

2.2. State of the art

This thesis aims at estimating the tire-road friction coefficient $\mu_{\max}$ based on vehicle lateral dynamics. It belongs to the large research area of tire-road friction coefficient estimation, whose existing methods, as shown in Fig.2.4, can be mainly divided into following two categories: cause-based and effect-based methods [122]. Cause-based methods attempt to investigate measured factors bringing about the changes of friction on the road based on sensors (vision, laser and temperature sensors, etc.) and then estimate road conditions. On the contrary, effect-based methods capture the response of tires and vehicles from different tire-road conditions and then extrapolate the tire-road friction coefficient. Although there are also some other methods like sensor fusion methods and Car-to-X (C2X) methods as mentioned in [78], these methods are actually related to the cause-based and effect-based methods. They either try to combine different estimated $\mu_{\max}$, resulted from cause-based methods or effect based methods, to infer the most probable $\mu_{\max}$ or transmit the estimated $\mu_{\max}$ with Car-to-Car (C2C) or Car-to-Infrastructure (C2I) techniques to other vehicles. Therefore, it can be concluded that, cause-based methods and effect-based methods are still the basics. This research focuses on conducting literature review of cause-based and effect-based methods described in section 2.2.1 and 2.2.2, respectively. For C2X and sensor fusion methods, readers may refer to [17, 69, 77].

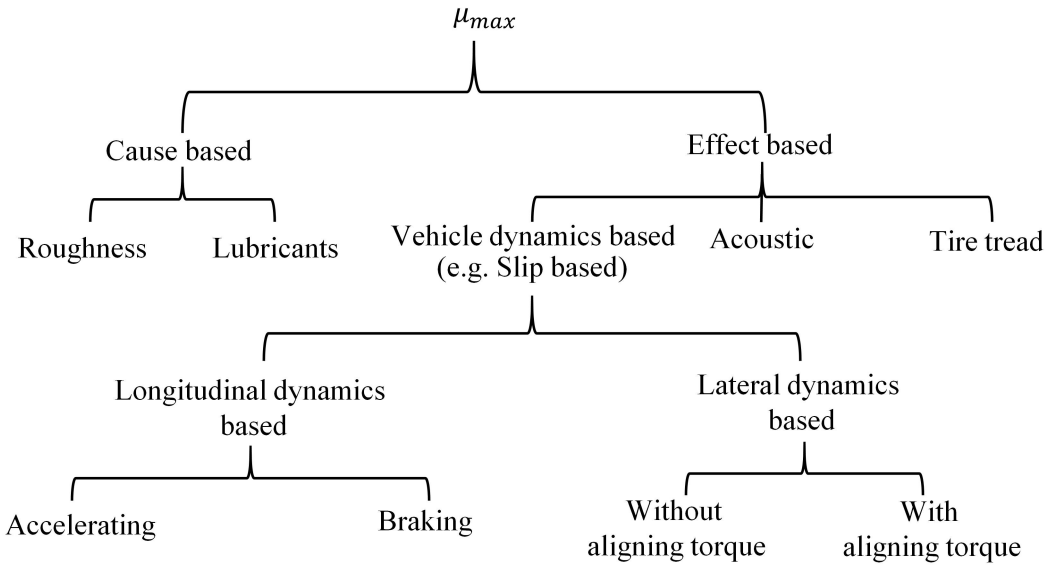

Figure 2.4.: Classification of tire-road friction estimation methods based on [122].

2.2.1. Cause-based methods

In cause-based approaches, two types of parameters—Roughness and Lubricants— are observed as shown in Fig.2.4. **Roughness parameters** mainly refer to the

- road type
- road geometry

while **Lubricants parameters** focus on

- additional media on the road such as waters, snow, ice, oil
- the depth of the film of the media, especially water depth

The principles of utilizing these observed parameters for $\mu_{\max}$ estimation are shown in Fig.2.5.

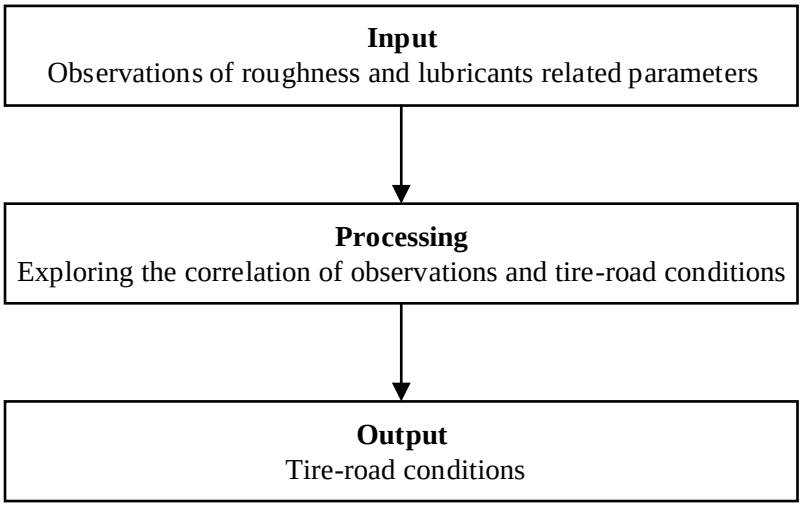

Figure 2.5.: Principles of cause-based method for $\mu_{\max}$ estimation [64].

The observed parameters can be processed by neural networks related algorithms, aiming at exploring the correlation of the observed parameters and $\mu_{\max}$. After this processing, the estimated road condition is outputted.

Andersson used optical sensors to measure infrared light at different wavelengths reflected from the road, such that different road surfaces (dry, wet, icy, snow surfaces) can be identified [14]. Holzmann applied cameras to classify road types by analyzing the pixels' luminance of road images and utilized microphones to improve the estimation accuracy [48]. In [57], the road condition is detected based on light polarization change reflected from road surface, and then texture analysis is conducted to improve recognition capability. More works can be found in [27, 70, 33, 49, 76, 46].

Overall, these methods are promising. As mentioned in [8], there are mainly two advantages: i) the $\mu_{\max}$ of the road surface ahead of the vehicle may be detected, which enables the planning and other control algorithms in vehicles perform better; and ii) $\mu_{\max}$ estimation is possible without physical excitation, leading to widely utilization of this estimation algorithm in various scenarios. However, there are also some shortcomings: at first, these methods require extra sensors installed on mass-produced vehicles which increase the costs. Besides, other factors (tire wear as well as hydroplanning, etc.) influencing $\mu_{\max}$ are difficult to be considered, so only an interval of the tire-road friction coefficient can be obtained which can be quite large sometimes. For example, on wet road condition, the interval may vary from 0.3 to 0.9 [117] which is not sufficient in many

applications such as AEB, ESC [129].

2.2.2. Effect-based methods

Effect-based methods focus on capturing the reaction of the vehicle on different tire-road conditions during driving and then estimate the $\mu_{\max}$. According to Fig. 2.4, effect-based methods can be mainly divided into three branches: vehicle dynamics based (e.g. slip-based), acoustic based as well as tire tread based methods. This research will concentrate on the review of slip based methods. With respect to acoustic and tire tread based methods, readers may refer to [64, 7, 122, 83, 6, 13, 118, 119].

2.2.2.1. Longitudinal dynamics based estimation

Methods for estimating $\mu_{\max}$ based on longitudinal dynamics mainly consist of slip-slope[1] based and model based as well as algebraic based methods.

For the slip-slope based methods, Gustafsson experimentally demonstrated that the relationship of the normalized tire longitudinal force and tire slip ratio is different under various road conditions during normal straight traction [43], so this relationship can be utilized to deduce the current $\mu_{\max}$. Hwang [53], Yi [127] conducted more experiments to prove that this relationship could work for normal traction. Uchanski [122] applied the slip-slope idea during braking maneuvers. By developing an *Optimal FIR Derivative*, the longitudinal tire force is estimated based on longitudinal vehicle dynamics. Then combined with the estimated slip ratio, the $\mu_{\max}$ is identified based on linear regression. However, this slip-slope based methods will be heavily influenced by the tire type, tire pressure, tire wear and so on, leading to a misjudgement of $\mu_{\max}$, hence, adaptation of the slip-slope relationship is necessary [122, 43].

For the model based method, Liu [80] estimated tire-road friction coefficient by writing it as a function of tire slip ratio and longitudinal force based on the special structure of a brush model. Therefore, the $\mu_{\max}$ can be obtained after the tire slip ratio and the longitudinal force are calculated. Lex implemented particle filtering to estimate tire-road friction with on-board vehicle sensors based on tire model TMsimple [47, 78]. In [114], Svendenius also implemented the brush model to estimate the $\mu_{\max}$. He firstly collected the sampled measurements (slip ratio and longitudinal force) into bins, in which

[1] The slip-slope method utilizes the relationship between normalized longitudinal tire force and slip ratio to determine the tire-road friction coefficient [97].

the available data are evenly spread and weighted along the force and slip axis. When the whole sampled measurements in the bins already demonstrate nonlinear tire characteristics, a Gauss-Newton method is applied to estimate tire-road friction coefficient. Canudas firstly formulated a quarter vehicle model as an affine parametrized nonlinear system based on a LuGre tire model. Subsequently, an adaptive observer is proposed to estimate tire-road friction coefficient [28]. Albinsson implemented an active tire force excitation method, in which large but opposite tire forces are exerted on the front and rear tires, while guaranteeing the intended vehicle motion. As a result, $\mu_{\max}$ estimation is possible with no limitation from the driver's input [11], however, this method can lead to increase in energy consumption.

For the algebraic methods, Villagra estimated $\mu_{\max}$ without using tire model by introducing the *extended braking stiffness* concept, refering to the slope of utilized tire-road friction coefficient against slip ratio at the operational point [123]. When this slope is flat enough, the $\mu_{\max}$ can be obtained.

2.2.2.2. Lateral dynamics based estimation

Research on tire-road friction estimation based on vehicle lateral dynamics is conducted for more than 20 years and a large amount of literature is dedicated to this topic. In the beginning, researchers focused on estimating $\mu_{\max}$ by exploiting the tire lateral force characteristics, which, do not reach the nonlinear region until large tire slip angle (see Fig. 2.3). This leads to large excitation as a necessity for $\mu_{\max}$ estimation, which makes the procedure impossible in normal driving such as motorway cruising. Recently, Electric Power System (EPS) or Active Front Steering system (AFS) are increasingly installed on vehicles, providing an extra signal — the front axle total aligning torque, containing tire self-aligning torque information — for $\mu_{\max}$ estimation. Moreover, it is worth to notice that tire self-aligning torque comes into nonlinear region earlier than lateral tire force saturates, see Fig. 2.6. As a result, only moderate excitation is needed to estimate $\mu_{\max}$ [51]. In this thesis, literature review of $\mu_{\max}$ estimation with lateral dynamics will be conducted based on whether the tire self-aligning torque information is utilized or not.

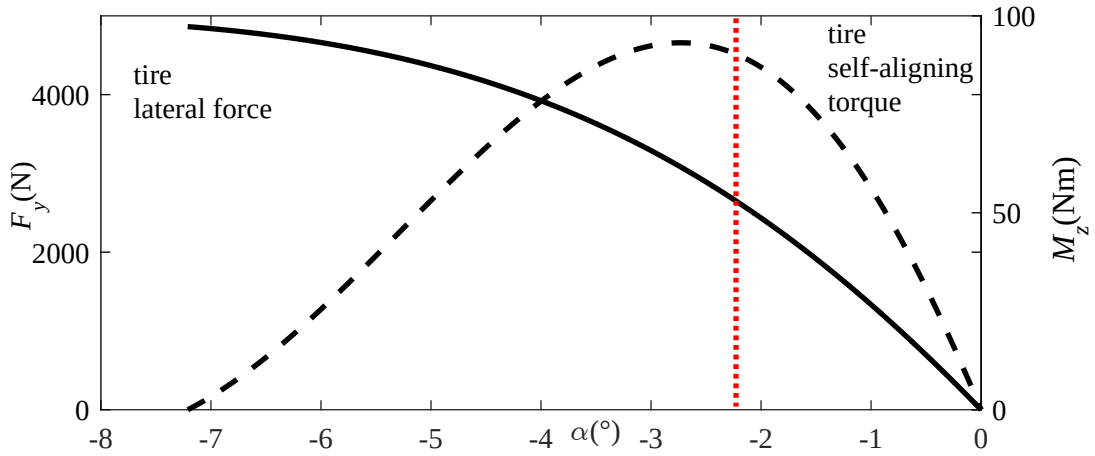

Figure 2.6.: Comparison of characteristics between tire lateral force and tire self-aligning torque.

2.2.2.2.1. Estimation without self-aligning torque (SAT)

Most of the researches for $\mu_{\max}$ estimation without tire self-aligning torque also have no access to Global Positioning System (GPS) information. Therefore, they usually also need to estimate side slip angle or its variants like tire slip angle. Boßdorf utilized Extended Kalman Filter (EKF) to simultaneously estimate vehicle side slip angle and tire-road friction coefficient with a two track vehicle model [25]. Ray also applied EKF to observe vehicle states and tire forces, then the obtained force and slip angle are compared statistically with those that result from a nominal tire model to select the most likely road friction coefficient [99]. Other examples of EKF or similar linearization based methods can refer to Best [24], Baffet [20] and Grip [37]. However, as a vehicle undergoes agile or extreme maneuvers, the tires are pushed to highly nonlinear operation regions resulting in nonlinear vehicle dynamics. Consequently, linearization based approaches, like EKF, do not perform well in this case [54]. In [38], Grip proposed a Lyapunov-based observer to identify the vehicle side slip angle with friction adaptation, but the observer is based on a crucial assumption that the tire force is affine in a tire-related parameter, which is not consistent with the traditional tire model like brush model and magic formula. In [31], Ding utilized recursive least squares (RLS) to estimate the vehicle side slip angle and tire-road friction coefficient by minimizing the squared errors between estimated lateral acceleration, yaw acceleration and their measured values. However, for implementing RLS, measured lateral acceleration and yaw acceleration have to be linearized around the estimated tire-road friction coefficient and the side slip angle, which may lead to

large estimation error when the tires come into the nonlinear region.

For the approaches with the GPS information, efforts are also put on by many researchers. Hahn at first obtained the vehicle lateral velocity with GPS information, then he implemented an adaptive estimator to simultaneously estimate tire-road friction coefficient and cornering stiffness based on a brush tire model [45]. Combined with GPS information, Gupta utilized a machine learning method — a polynomial kernel Support Vector Machine (SVM) — as a classier to estimate tire-road friction coefficient during steering [42]. Though the implementation of GPS can simplify lateral velocity estimation and thus ease the difficulties of TRFC estimation, the continuous availability of the GPS signals in the urban area is always a challenge [30].

2.2.2.2.2. Estimation with tire self-aligning torque

The introduction of EPS or AFS in the mass-production vehicles makes the self-aligning torque information available (through estimation) for $\mu_{\max}$ estimation. The methods can also be divided into two branches based on whether GPS information is available or not. For the methods without GPS information, various researches are conducted. In [51], Hsu designed a nonlinear observer and argued that the estimation error converges when the front axle tire slip angle and the $\mu_{\max}$ are both over- or underestimated at the same time, which suggests that the observer may not be stable. In [10], Ahn designed a nonlinear observer to robustly estimate front axle tire slip angle and $\mu_{\max}$. He utilized Sequential Quadratic Programming (SQP) to calculate the best suitable feedback gains for the observer, such that the operation region of the front axle tire slip angle and $\mu_{\max}$ in the state space is maximized under a given required tolerable initial estimation error, a steady state estimation error as well as an observer's convergent rate. However, when the states (front axle tire slip angle and $\mu_{\max}$) are in the tire saturation region and quasi linear region of tire characteristics, the attraction domain of the operation points is still quite small and does not satisfy the requirements (tolerable initial estimation error, steady state estimation error as well as observer's convergent rate). This results in a possible instability of the observer in the real application due to the model uncertainty or poor initial guesses, which is also demonstrated in his own work. In ([9]), a nonlinear least squares optimization is formulated to estimate front axle tire slip angle and $\mu_{\max}$. The authors applied standard non-linear optimization algorithm to this problem. Unfortunately as the optimization is non-convex, there is no guarantee to find the global minimum without an accurate initial guess. Consequently the observation error can be excessively large in some situations. In [85], EKF for estimating the $\mu_{\max}$ and

front axle tire slip angle is applied, which, however, cannot ensure the stability of the observer. Matilainen innovatively utilized the front tire lateral force, normal force, tire self-aligning torque as well as contact length to express $\mu_{\max}$ based on the brush model and Experiments demonstrate good performance [84].

For methods with GPS based positioning data, there is rare work. In [51], the judgement of whether the self-aligning torque characteristics comes into the nonlinear region is firstly conducted by comparing the difference of linear and nonlinear regression methods. When a large difference is obtained, enough information of $\mu_{\max}$ is indicated and the nonlinear regression method will output the estimated $\mu_{\max}$.

2.2.3. Summary

This section summarizes cause-based and effect-based methods for tire-road friction coefficient estimation. Cause-based methods are promising, since, with the development of highly automated functions, more and more sensors like camera and radar will be installed on the mass-produced vehicles, enriching the availability of the $\mu_{\max}$. What needs to be improved is the reliability and accuracy of the $\mu_{\max}$ estimation results with respect to environment and tire uncertainties. About effect-based methods, emphasis of the literature review was put on the vehicle dynamics based methods, which are also listed in the table 2.1. In the longitudinal dynamics based methods, slip-slope based methods can detect road conditions under low excitation, however, they are sensitive to tire wear, tire type as well as tire pressure. Model based methods and algebraic methods cannot obtain reliable $\mu_{\max}$ until the tire characteristics come into the nonlinear region, resulting in more excitation requirement from the driver compared to slip-slope based methods. Lateral dynamics based methods with GPS are promising, because GPS can measure side slip angle that is difficult to be estimated. Consequently, regression methods can be implemented to estimate the $\mu_{\max}$ both with and without self-aligning torque. However, the GPS signals have errors such as multi-path induced errors [8] and may not be always available in real applications. Therefore, many researchers still focus on lateral dynamics based methods with inertial sensors which are reliable and accurate, but how to design an observer which guarantees stability in wide range of vehicle operations is still an open question.

Table 2.1.: Category of vehicle dynamics based methods

	Methods Category	**References**
Longitudinal dynamics based	Slip-slope-based	[43],[53],[127],[122]
	Model-based	[80], [78], [114], [28], [11]
	Algebraic	[123]
Lateral dynamics based without TSAT	without GPS	[25], [99], [24], [37], [20], [38], [31]
	with GPS	[45], [42]
Lateral dynamics based with TSAT	without GPS	[51], [10], [9], [85], [84]
	with GPS	[51]

2.3. Nonlinear state and parameter estimation

A classical problem occurring in vehicle automation is either lack of measured signals which are necessary for control purposes, or the measured signals are of low quality because of heavy noise, time delays or low sampling rates. In these situations, an observer is advisable to estimate these unknown or inaccurate states by modelling the vehicle's dynamics based on the available measurements. The tire-road friction coefficient estimation based on vehicle lateral dynamics without GPS information is a good example. In literature, researchers often formulate this problem as a nonlinear state (side slip angle or tire slip angle) and parameter (tire-road friction coefficient) estimation problem, then utilize either deterministic-based methods (Luberger type observers) or stochastic-based methods (Kalman method and its extensions) to simultaneously estimate the unknown state and parameter. These approaches were reviewed in section 2.2.2.2. This section will review deterministic-based methods for simultaneous state and parameter estimation based on nonlinear systems. It has to be mentioned that, this section will not review the stochastic-based methods such as EKF [56], Unscented Kalman Filter (UKF) [58, 59], and Particle Filter (PF) [29, 105], etc., because they usually offer no proof for stability which is one of the research objectives of this thesis.

2.3.1. Approaches in nonlinear state and parameter estimation

2.3.1.1. Nonlinear adaptive observers

In presence of unknown parameters in a dynamic system, online estimation of them to yield a desired control results may be necessary. Consider a dynamic system shown in (2.3), where x is a state vector, θ is a vector of unknown parameters, u is an input vector and y is a measurement vector. Observers estimating the states with online adaptation of unknown parameters based on available measurements for dynamic systems are called adaptive observers[22]. There is much literature available on designing adaptive observers for linear systems [55, 22, 130], proposing a typical ideal by separating the state and parameter estimation into two sub-problems: 1) using gradient based or least squares methods to estimate the unknown parameters with input and measured signals 2) applying the Luenberger type observers for state estimation with the estimated parameters as 'known' ones in the linear system [55]. The corresponding estimation structure of adaptive observers for linear systems is shown in Fig. 2.7(a). However, for nonlinear system, relying on input and measured signals to estimate unknown parameters are usually not enough. Therefore, researchers bring about other estimation structure as illustrated in Fig. 2.7(b), which additionally requires the estimated states as feedback for estimating unknown parameters. There are various nonlinear adaptive observers, which can be mainly divided into two branches: nonlinear adaptive observers for parameter-affine[2] and parameter-non-affine nonlinear systems. They will be discussed in the following separately.

$$\begin{aligned} \dot{x} &= f(x, \theta, u, t) \\ y &= h(x, u), \end{aligned} \tag{2.3}$$

For parameter-affine nonlinear systems, there are various observers available according to the structure of the dynamic systems. Systems with the following typical structure can express most of the available results:

$$\begin{aligned} \dot{x} &= Ax + \varphi(x, u) + B\Psi(x, u)\theta \\ y &= Cx, \end{aligned} \tag{2.4}$$

[2]The vector of unknown parameters θ appears linearly in the nonlinear system.

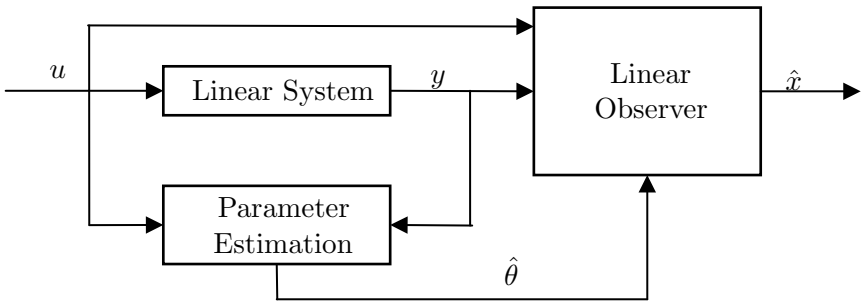

(a) General structure of adaptive observers for linear systems

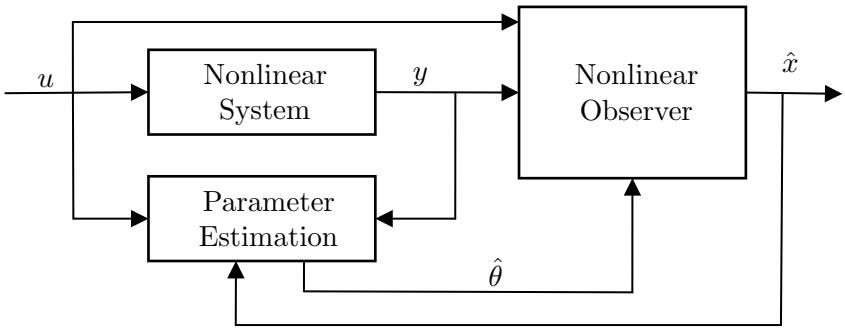

(b) General structure of adaptive observers for nonlinear systems

Figure 2.7.: Different structures of adaptive observers for linear and nonlinear systems

where $A \in \mathbb{R}^{n\times n}$, $B \in \mathbb{R}^{n\times m}$, $\varphi : \mathbb{R}^n \times \mathbb{R}^p \to \mathbb{R}^n$, $\Psi : \mathbb{R}^n \times \mathbb{R}^p \to \mathbb{R}^{m\times r}$, $\theta \in \mathbb{R}^r$, $C \in \mathbb{R}^{m\times n}$. The corresponding nonlinear adaptive observer [22] is

$$\begin{aligned} \dot{\hat{x}} &= A\hat{x} + \varphi(\hat{x}, u) + B\Psi(\hat{x}, u)\hat{\theta} + L(y - C\hat{x}), \\ \dot{\hat{\theta}} &= \Gamma\Psi(\hat{x}, u)^T(y - C\hat{x}), \end{aligned} \tag{2.5}$$

if following conditions are satisfied: strict positive real (SPR) and some Lipschitz conditions. To be specific, there exist symmetric positive definite matrices P, Q and a gain matrix L as well as positive constant k_i fulfilling:

$$\begin{aligned} P(A - LC) + (A - LC)^T P &= -Q, \\ PB &= C^T, \\ k_\varphi + k_\Psi \max(\theta)||B|| &\leq \frac{\lambda_{min}(Q) - k_i}{2\lambda_{max}(P)}, \end{aligned} \tag{2.6}$$

where k_φ and k_Ψ are Lipschitz constants for $\varphi(x,u)$ and $\Psi(x,u)$ uniformly w.r.t u, respectively, $\Gamma \in \mathbb{R}^{r\times r}$ is a positive definite matrix. Denoting $\tilde{x}$ and $\tilde{\theta}$ as the estimation error of x and θ, we have a Lyapunov function

$$V(\tilde{x},\tilde{\theta}) \quad = \quad \tilde{x}^T P\tilde{x} + \tilde{\theta}^T\Gamma^{-1}\tilde{\theta}. \tag{2.7}$$

By calculating the derivative of $V(\tilde{x},\tilde{\theta})$, we can deduce that

$$\dot{V}(\tilde{x},\tilde{\theta}) \quad \leq \quad -k_i||\tilde{x}||. \tag{2.8}$$

Therefore, the equilibrium $(\tilde{x},\tilde{\theta})$ is stable. Further use of Barbălat's Lemma, we have

$$\tilde{x} \to 0 \quad \text{as} \quad t \to \infty. \tag{2.9}$$

Define

$$B\Psi(\hat{x},u) \quad = \quad W^T(t), \tag{2.10}$$

and if $||W(t)||$ as well as $||\dot{W}(t)||$ are uniformly bounded and $W(t)$ is persistently exciting [22] which will be described later, we have

$$\tilde{\theta} \to 0 \quad \text{as} \quad t \to \infty. \tag{2.11}$$

Except for the system featuring the above structure, some literature presented adaptive observers for other structure of nonlinear systems. Besancon and Zhang proposed an adaptive version of the high gain observer for a class of nonlinear systems in [23], without the need of the system being SPR. Stamnes extends the existing class of nonlinear systems for which adaptive observers with stability guarantee can be designed. He presented a type of adaptive observer features that both unknown parameters and non-linearity of the unmeasured states can appear in the dynamics of the unmeasured states [110]. Meanwhile, the process of designing an implementable update law, which is difficult to be directly constructed with Lyapunov analysis, is simplified to solve a certain partial differential equation (PDE).

For parameter-non-affine nonlinear system, there is rare work available. In [40], adaptation laws for monotonically parametrized perturbations are proposed with all states

measurable based on following nonlinear system:

$$\begin{aligned} \dot{x} &= f(t,x) + B(t,x)(g(t,x,\theta) + v(t,x)), \\ y &= x, \end{aligned} \tag{2.12}$$

where $x \in \mathbb{R}^n$ is a measured state vector and $\theta \in \mathbb{R}^p$ is a vector of unknown constant parameters, $f : \mathbb{R}_{\geq 0} \times \mathbb{R}^n \to \mathbb{R}^n$, $B : \mathbb{R}_{\geq 0} \times \mathbb{R}^n \to \mathbb{R}^{n \times m}$, $g : \mathbb{R}_{\geq 0} \times \mathbb{R}^n \times \mathbb{R}^p \to \mathbb{R}^m$, $v : \mathbb{R}_{\geq 0} \times \mathbb{R}^n \to \mathbb{R}^m$. Denote ϕ as $B(t,x)g(t,x,\theta)$ to represent the full unknown perturbations in (2.12). The overall idea of the estimation scheme shown in Fig. 2.8 is: 1) design of an update law that exponentially estimates θ based on the quantity ϕ, as if ϕ were known, 2) then design of an observer for ϕ as if θ were known. With small gain theorem [66], the uniform exponential stability of the estimation error of ϕ and θ can be guaranteed based on some persistent excitation conditions and monotonicity of $g(t,x,\theta)$ w.r.t θ. Similar works with all states measurable are also demonstrated in [15, 120]. Annaswamy introduced a tuning function and an adaptive law based on a min-max strategy to estimate the unknown parameters, with assumption that the nonlinearity in the parameters is either convex or concave [15]. There are also some researchers focusing on simultaneously parameter and state estimation for parameter-non-affine nonlinear system. In [41], under a set of technique assumptions, Grip, et al. proposed an adaptive observer for systems that can be described by a linear part with a nonlinear perturbation, in which there are nonlinearities in the system states and unknown parameters. The nonlinear system is described as follows:

$$\begin{aligned} \dot{x} &= Ax + Bu + E\phi(u,y,x,\theta), \\ y &= Cx, \end{aligned} \tag{2.13}$$

where $x \in \mathbb{R}^n$, $u \in \mathbb{R}^m$, $y \in \mathbb{R}^r$, $\phi(u,y,x,\theta) : \mathbb{R}^m \times \mathbb{R}^r \times \mathbb{R}^n \times \mathbb{R}^p \to \mathbb{R}^k$. The observers consist of a modified high-gain observer and a parameter estimator. The high gain observer is to estimate x and ϕ, while the parameter estimator is designed to identify the unknown parameters. The estimation structure is also illustrated in Fig. 2.9. Except the research described in [41], readers can also refer to similar work for simultaneously state and parameter estimation in [121], where the concepts of weakly attracting sets and non-uniform convergence are utilized.

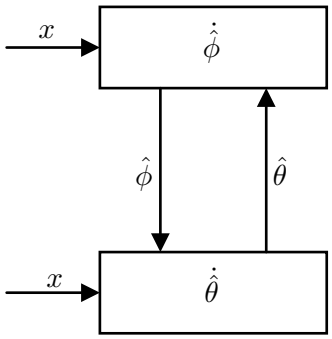

Figure 2.8.: Overall idea of the estimation scheme for ϕ and θ

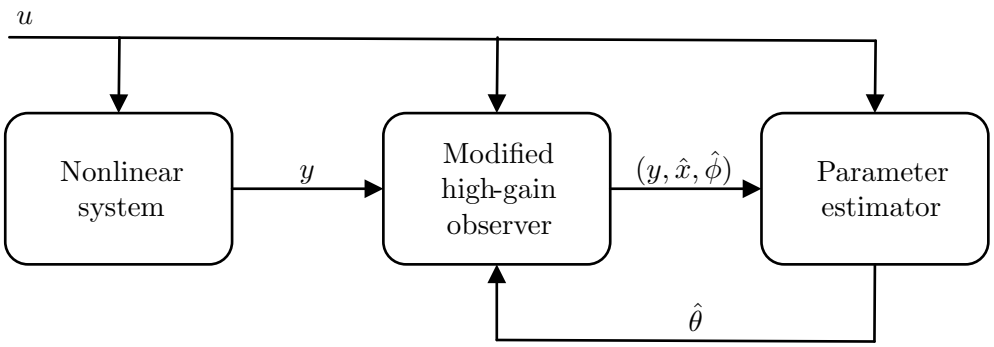

Figure 2.9.: Estimation structure of the adaptive observer based on [36]

The aforementioned term " Persistent Excitation " (PE) will be introduced in the following, which is critical for the convergence of unknown parameters $\hat{\theta}$ to the real value θ in the nonlinear adaptive observer. Take the equation (2.4) as an example to describe this problem. With the assumption of $||W(t)||$ and $||\dot{W}(t)||$ being uniformly bounded as defined in equation (2.10), only

$$\lim_{t\to\infty} W^T(t)\tilde{\theta} = 0, \tag{2.14}$$

can be obtained, which does not give any information about the convergence of the estimation error of θ. Therefore, extra assumption about $W(t)$ should be introduced which is called persistent excitation, defined as follows:

Definition 2.3.1. *Persistent Excitation (PE): For* $\forall\ t \geq 0$, $\exists\ \ T > 0$ *and* $\varepsilon > 0$, *such*

that

$$\int_{t+T}^{t} W(\tau)W^T(\tau)d\tau \geq \varepsilon I. \tag{2.15}$$

When this PE condition is satisfied, the convergence of $\tilde{\theta}$ to the origin can be guaranteed [22]. It has to be mentioned that the PE condition cannot always be satisfied, since $W(t)$ may rely on external signals which cannot be determined by the designer of the nonlinear adaptive observer.

2.3.1.2. Approaches for other observers

Except nonlinear adaptive observers, several other methods consider the unknown parameters in equation (2.3) as states. Consequently, this nonlinear equation is formulated as follows [3]:

$$\begin{aligned} \dot{x} &= f(x,u,t). \\ y &= h(x,u), \end{aligned} \tag{2.16}$$

There is much literature available for nonlinear observers design. They can be mainly divided into high gain observer (HGO) [116, 95, 65, 96], circle criteria based observer (CCO) [16, 34], sliding mode observer (SMO) [107, 109], immersion and invariance observer (IIO) [60, 61], coordinate transformation based observer (CTO) [72, 73, 62, 74, 71], moving horizon observer (MVO) [98, 12, 113]. This section will not extend the detailed review of these observers, but their mechanism, pros and cons are briefly listed as follows:

- **High gain observer**
  Mechanism: the observer is designed based on the utilization of high-gain linear terms to dominate the state dependent nonlinearities in the system.
  Pros: canonical form is available, simple to implement.
  Cons: sensitive to signal noise, global Lipschitz condition is usually necessary.
- **Circle criteria based observer**
  Mechanism: given that an observer error dynamics is expressed as a linear part and a monotonic nonlinear part w.r.t. state estimation error, then based on linear matrix inequality (LMI), the observer feedback gains are computed to satisfy the circle criterion and, hence, to drive the observer error to zero.

[3] In order to use the standard notion from the control community [66], we here still use x to represent the states (including states and parameters), and f and h to express the nonlinear equations.

Pros: simple to implement with LMI, the restriction of global Lipschitz is removed.
Cons: the linear part of the observer error system is strict positive real (SPR); the nonlinearity in the observer error system should satisfy the sector condition of the circle criterion.

- **Sliding mode observer**
  Mechanism: utilization of sliding mode technique to design nonlinear observer
  Pros: robust to model uncertainties
  Cons: chattering phenomenon, sensitive to noise

- **Immersion and invariance observer**
  Mechanism: transformation of a nonlinear observer design problem into finding certain mapping so that a chosen manifold, corresponding to estimation error being equal to zero, is rendered attractive and invariant.
  Pros: the observer design framework is, in theory, applicable for general nonlinear systems.
  Cons: finding the mapping to render the chosen manifold attractive and invariant is in general difficult.

- **Coordinate transformation based observer**
  Mechanism: reduction of the nonlinear system into a linear system by coordinate transformation, such that linear observer design techniques can be applied.
  Pros: usually applicable for many autonomous systems.
  Cons: in general not suitable for nonautonomous system, the existence of the transformation may rely on some stringent assumptions.

- **Moving horizon observer**
  Mechanism: the state estimation problem is formulated as an online optimization problem based on dynamics of the nonlinear system with a list of current and previous measurements.
  Pros: robust to measurement noise, constraints of the states can also be considered.
  Cons: the optimization process may be time-consuming, good initial guesses of the unknown states may be necessary, stability of the observer may be a problem.

2.4. Technical challenges of observer design for $\mu_{\max}$ estimation

As mentioned in the thesis objectives, $\mu_{\max}$ will be estimated based on vehicle lateral dynamics without GPS information, so in general vehicle lateral velocity or side slip angle

has to be estimated. However, there are following technical challenges for simultaneously estimation of vehicle lateral velocity and $\mu_{\max}$:

- Nonlinear tire modelling results in highly nonlinear vehicle lateral dynamics,
- Both unknown $\mu_{\max}$ and tire slip angle appear nonlinearly and are coupled with each other in the tire model.

Consider the simple single track model as an example see in Fig. 3.1 to explain these difficulties. For the case with front axle tire self-aligning torque information, the single track model with measurements can be written as:

$$\begin{aligned} \dot{\omega} &= \frac{l_f F_{yf}(\alpha_f, \mu_{\max}) \cos\delta}{I_z} - \frac{l_r F_{yr}(\alpha_r, \mu_{\max})}{I_z} \\ \dot{v}_y &= a_y(\alpha_f, \alpha_r, \mu_{\max}) - \omega v_x \\ y &= [\omega, a_y(\alpha_f, \alpha_r, \mu_{\max}), M_{zf}(\alpha_f, \mu_{\max})]^T, \end{aligned} \tag{2.17}$$

with

$$\alpha_f = \frac{v_y + l_f\omega}{v_x} - \delta, \quad \alpha_r = \frac{v_y - l_r\omega}{v_x}, \tag{2.18}$$

while the case without front axle tire self-aligning torque information, the single track model with measurements will be written as:

$$\begin{aligned} \dot{\omega} &= \frac{l_f F_{yf}(\alpha_f, \mu_{\max}) \cos\delta}{I_z} - \frac{l_r F_{yr}(\alpha_r, \mu_{\max})}{I_z} \\ \dot{v}_y &= a_y(\alpha_f, \alpha_r, \mu_{\max}) - \omega v_x \\ y &= [\omega, a_y(\alpha_f, \alpha_r, \mu_{\max})]^T, \end{aligned} \tag{2.19}$$

with

$$\alpha_f = \frac{v_y + l_f\omega}{v_x} - \delta, \quad \alpha_r = \frac{v_y - l_r\omega}{v_x}, \tag{2.20}$$

where ω is the yaw rate, a_y the lateral acceleration, v_y the lateral velocity, l_f is the distance between the vehicle front axle to the center of gravity, l_r the distance between the vehicle rear axle to the center of gravity, δ the front wheel steering angle, v_x the longitudinal velocity, m the vehicle mass, I_z the yaw moment of inertia of the vehicle, F_{yf} and F_{yr} are the front and rear axle tire lateral force, respectively, M_{zf} the front axle tire self-aligning torque, α_f the vehicle front axle tire slip angle, α_r the vehicle rear axle tire slip angle.

Since $a_y = \frac{F_{yf}\cos\delta + F_{yr}}{m}$, it can be concluded that the nonlinearity of the single track model depends on the nonlinearity of the tire model. However, the classical tire mod-

els, such as the brush model [90], the magic formula [90], the dugoff tire model [32], TMsimple [47]/TMeasy[4] [100], are highly nonlinear, in which both tire slip angle and $\mu_{\max}$ appear nonlinearly and are coupled with each other in the tire models, leading to high nonlinearities in the single track model. To the author's best knowledge, the existing approaches of adaptive observers for non-affine parametrized nonlinear system may not be suitable to be directly applied in both cases (cases with and without self-aligning torque). Besides, even consider $\mu_{\max}$ as a state, and attempt to utilize the existing nonlinear observer methods reviewed in 2.3.1.2, it seems difficult to satisfy the corresponding canonical form or solve the PDEs required by the nonlinear observer methods. The moving horizon observer may be a choice (Ahn also utilized a similar method [9]), but solving the non-convex optimization problem real time with stability guarantee is also a great challenge. Most of the existing work based on vehicle lateral dynamics reviewed in 2.2.2.2 does not demonstrate satisfactory solutions: some of them utilize linearization based methods which may be unstable in highly nonlinear region [25, 24, 20], and some designed observers with unrealistic tire model assumptions [38] or with small operation regions [10]. It seems there is a great barrier to come up with a good theoretical solution for simultaneous lateral velocity and tire-road friction estimation.

2.5. Approaches in this research

Several approaches for nonlinear observer design based on vehicle lateral dynamics are presented in the following.

For the case with tire self-aligning torque information, it can be noted that the tire models like the brush model, the magic formula[5],the dugoff tire model, TMsimple/TMeasy can all be written as following form:

$$\begin{aligned} F_y &= \mu_{\max} \cdot f(\frac{\alpha}{\mu_{\max}}), \\ M_z &= \mu_{\max} \cdot g(\frac{\alpha}{\mu_{\max}}). \end{aligned} \tag{2.21}$$

Regard $\frac{\alpha}{\mu_{\max}}$ as a new state variable, it can be noticed that $\mu_{\max}$ and $\frac{\alpha}{\mu_{\max}}$ are decoupled with each other and $\mu_{\max}$ appears linearly in the tire model. Hence, the single track

[4]Usually TMsimple and TMeasy are used to express the tire lateral force and self-aligning torque, respectively.

[5]For magic formula, the influence of horizontal and vertical shift as well as the camber reduction on the pure lateral force is omitted, so is the influence of horizontal and vertical shift as well as residual torque on the tire self-aligning torque [90]

model can be formulated into a low-triangular affine-parametrized nonlinear system as shown below:

$$\begin{aligned} \dot{\omega} &= \varrho_1(t) + \varrho_2(t)\varrho_3(t, x_f) \\ \dot{x}_f &= \varrho_4(t, x_f) + \varrho_5(t)\theta \\ y &= \omega. \end{aligned} \tag{2.22}$$

where $\varrho_1(t)$ and $\varrho_2(t)$ as well as $\varrho_5(t)$ are time varying functions, $x_f = \frac{\alpha_f}{\mu_{\max}}$, α_f is the front axle tire slip angle, $\varrho_3(t, x_f)$ is the monotonic and odd function with respect to x_f and uniformly to t, $\varrho_4(t, x_f)$ is the function and global Lipschitz with respect to x_f and uniformly to t, $\theta = \frac{1}{\mu_{\max}}$. Based on this transformation, two different methods to estimate x_f and $\mu_{\max}$ are proposed. The estimation framework can be seen in Fig. 2.10 and Fig. 2.11, respectively.

In method I, the measurements (yaw rate, lateral acceleration as well as longitudinal velocity etc.) are firstly utilized to estimate the front axle tire lateral force with a novel strategy based on unknown input observer (UIO) [94]. Meanwhile, the front axle total aligning torque (contains tire self-aligning torque information) is estimated on the basis of the measured tie rod force. Then, with the front axle tire lateral force and total aligning torque as input, an indirect measurement $y(x_f, t)$ is generated. Combining with this indirect measurement a nonlinear adaptive observer is designed to estimate the tire-road friction coefficient. To increase the robustness of the estimation result, an excitation detection block is proposed with defined criteria to better update estimated tire-road friction coefficient.

Though method I is simple to implement, the indirect measurement is singular when total aligning torque approaches zero. Meanwhile, front axle lateral force needs to be extra estimated. Therefore, a method II, aiming at eliminating aforementioned shortcomings, is proposed. Based on system (2.22), an adaptive observer, generally applicable for non-affine parametrized lower-triangular nonlinear system, is designed. Furthermore, the design procedure is applied to the tire-road friction coefficient estimation problem, with no need to estimate front axle tire lateral force. After various simulation and experimental validation, the estimation result of $\mu_{\max}$ from method II is overall similar to that from method I in terms of root mean square of estimation error (RMS).

For the case without tire self-aligning torque information, it's in general difficult to simultaneously estimate lateral velocity and $\mu_{\max}$. An approach similar to the moving horizon estimation in this research is presented, which, however, propose an innovative

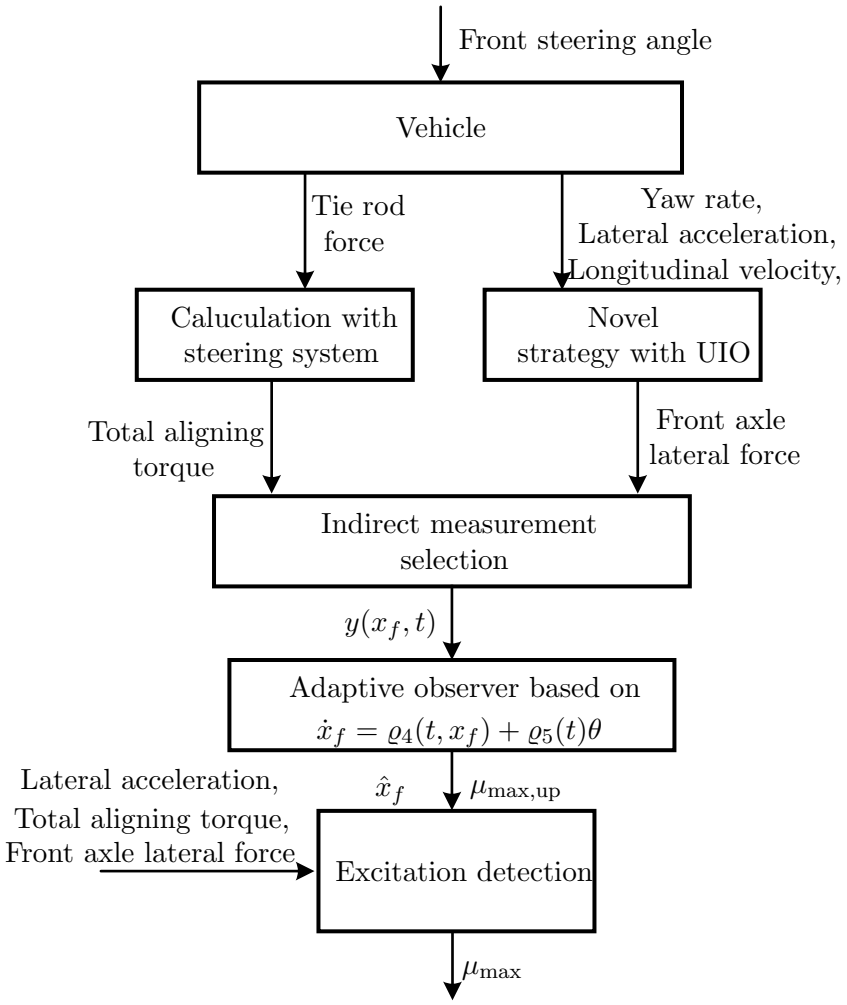

Figure 2.10.: Estimation structure of method I

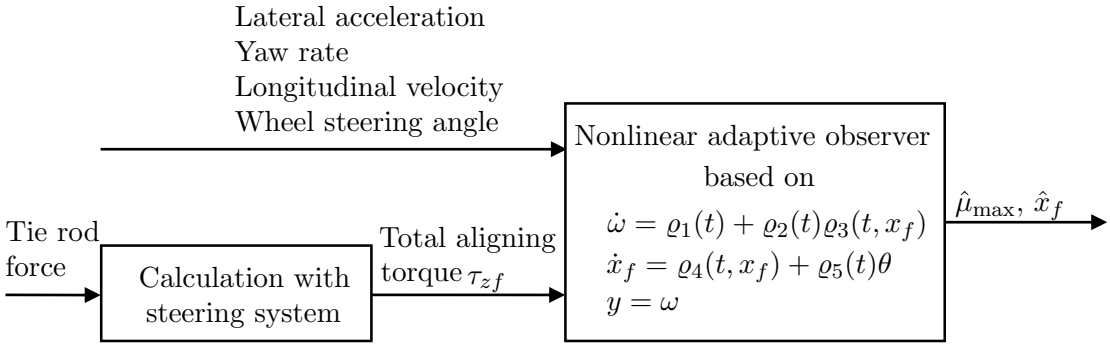

Figure 2.11.: Estimation structure of method II

scheme shown in fig. 2.12 to leave sufficient time for solving a non-convex optimization problem and meanwhile guarantee the stability of the estimation error. This scheme can be realized since the derivative of lateral velocity and $\mu_{\max}$ (assumed to be zero) are measurable, which inspires us to interweave the discrete time solution of the non-convex optimization for v_y and $\mu_{\max}$ as initial value of integration and continuous integration of measurable derivatives. Therefore, this scheme can real time estimate vehicle lateral velocity and $\mu_{\max}$ despite of the non-convex optimization.

Eventually, it can be ensured that, the whole proposed observers can work in real time and their stability for $\mu_{\max}$ can be mathematically guaranteed in wide range of vehicle operations[6].

[6]In each method, an operational region of the observer in the later chapters will be given.

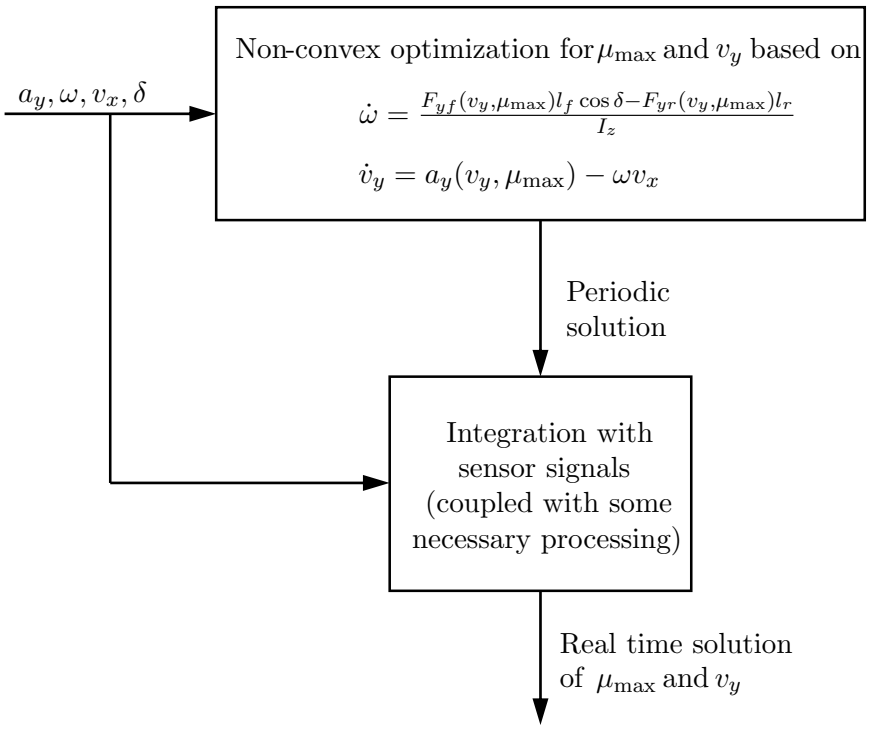

Figure 2.12.: Estimation structure of method III

3. Vehicle Model

In this chapter, the models used for $\mu_{\max}$ estimation will be described. At first, the vehicle model based on lateral dynamics will be presented. Subsequently, the tire model TMsimple for modelling tire lateral force and TMeasy for tire self-aligning torque will be introduced. Finally, the steering system, together with the method utilized for total aligning torque estimation, will be demonstrated. It has to be mentioned that the identification and validation of the tire model, steering system model as well as the whole vehicle model based on lateral dynamics is described in Appx. A.

3.1. Vehicle model based on lateral dynamics

3.1.1. Single track model

In this thesis, for simplifying the description of vehicle lateral dynamics without losing its main dynamic property, the vehicle is assumed to move on a flat, horizontal surface and the external forces, such as air drag, forces caused by slope and bank[1], are omitted. In other words, only the tire road interaction forces are exerted on the vehicle. Therefore, a nonlinear single track model, with yaw rate and lateral velocity as state variables as shown in Fig. 3.1, can be used to express the lateral dynamics of the vehicle. It considers lateral load transfer (caused by lateral acceleration), and assumes that $\mu_{\max}$ is piecewise constant and longitudinal velocity v_x is slowly changing or positive constant[2]. The corresponding differential equations are described as

$$\dot{\omega} \;=\; \frac{l_f F_{yf} \cos\delta}{I_z} - \frac{l_r F_{yr}}{I_z}, \tag{3.1a}$$

[1] In case of slopes and banks in the real application, the work from [39] can be implemented to estimate them.

[2] These assumptions are proposed for neglecting time derivatives of $\mu_{\max}$ and v_x. Hence, if the vehicle accelerates or brakes aggressively during cornering, the assumption of v_x for single track model in this work does not hold any more. Besides, if the $\mu_{\max}$ varies dramatically under a fixed road surface due to e.g. varying tire temperature caused by aggressive variation of v_x, the assumption for $\mu_{\max}$ is invalid.

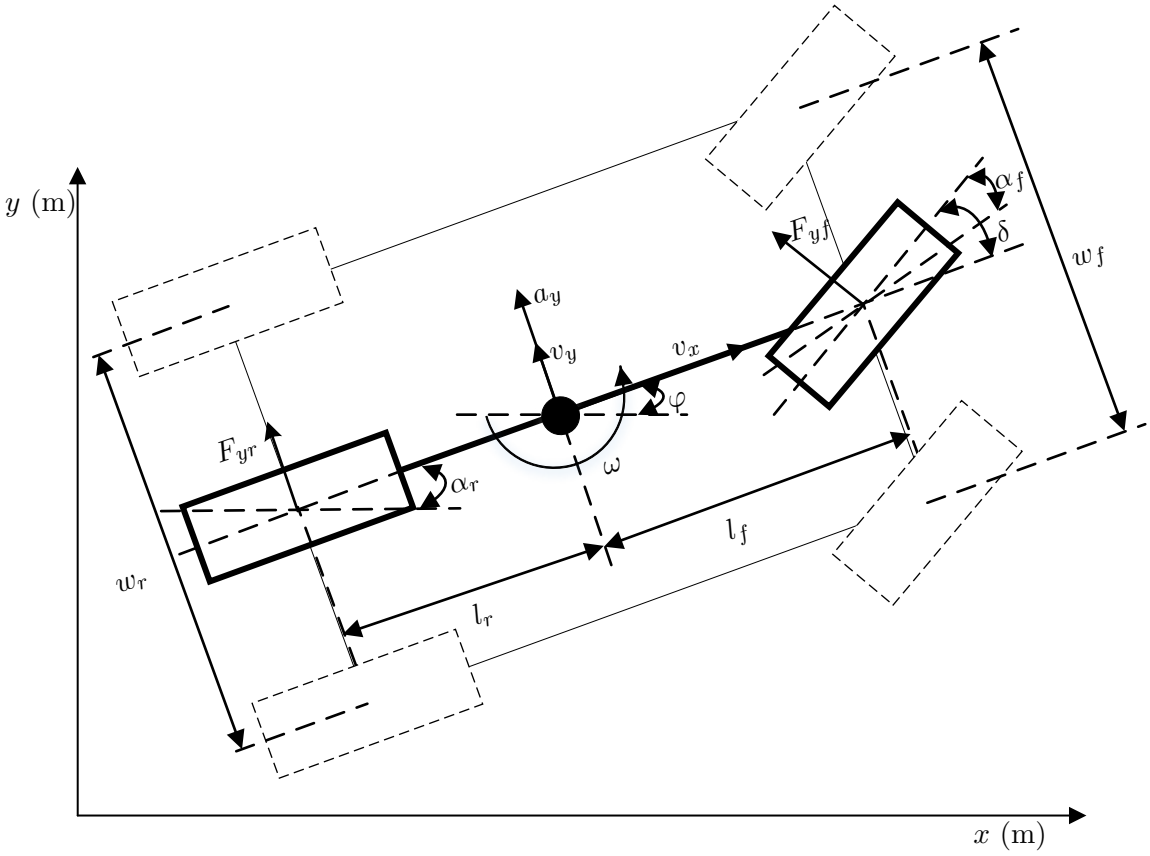

Figure 3.1.: Single track model

$$\dot{v}_y \;=\; a_y - \omega v_x, \tag{3.1b}$$

with

$$\alpha_f \;=\; \frac{v_y + l_f\omega}{v_x} - \delta, \quad \alpha_r \;=\; \frac{v_y - l_r\omega}{v_x} \tag{3.2}$$

where l_f is the distance between the front axle to the center of gravity, l_r the distance between the rear axle to the center of gravity, δ the front wheel steering angle, F_{yf} the front axle lateral force, F_{yr} the rear axle tire lateral force, ω the yaw rate, v_y the side slip angle, a_y the lateral acceleration and I_z the moment of inertia of the vehicle, α_f the front axle tire slip angle, α_r the rear axle tire slip angle, φ the heading angle.

3.1.2. Load transfer

Dynamic tire loads of the vehicle occur during accelerations. If the vertical dynamics are ignored, the variations of load force on the tires can be calculated by using the

longitudinal and lateral acceleration. Since the v_x is assumed to be slowly changing or positive constant, lateral acceleration can be mainly utilized to express the variations.

If the front axle and rear axle are considered to be decoupled with each other, the tire load transfer on front axle and rear axle can be calculated, separately [68]. Introducing a virtual mass m_f to express the static front axle tire loads as shown in Fig. 3.2,

$$m_f = \frac{ml_r}{l_f + l_r} \tag{3.3}$$

is deduced. Based on the contact point of the front left wheel, the torque balance equation

$$m_f g \frac{w_f}{2} + m_f a_y h_g = F_{zfr} w_f \tag{3.4}$$

is obtained, where h_g is the height of gravity, F_{zfr} the front right wheel normal force, w_f the front track, g the acceleration of gravity. Replacing m_f from equation (3.3), the front right wheel normal force can be calculated as follows:

$$F_{zfr} = \frac{ml_r}{l_f + l_r}(\frac{g}{2} + \frac{a_y h_g}{w_f}). \tag{3.5}$$

The remaining normal forces are obtained by

$$F_{zfl} = \frac{ml_r}{l_f + l_r}(\frac{g}{2} - \frac{a_y h_g}{w_f}), \tag{3.6a}$$

$$F_{zrl} = \frac{ml_f}{l_f + l_r}(\frac{g}{2} - \frac{a_y h_g}{w_r}), \tag{3.6b}$$

$$F_{zrr} = \frac{ml_f}{l_f + l_r}(\frac{g}{2} + \frac{a_y h_g}{w_r}), \tag{3.6c}$$

where F_{zfl}, F_{zrl}, F_{zrr} are the front left, rear left, rear right normal force, respectively, w_r is the rear track.

3.2. Tire model

A suitable tire model for describing tire lateral force and tire self-aligning torque is very important. Tire models, such as magic formula [90], brush model [90] as well as TM-simple (for tire lateral force) [47]/TMeasy (tire self-aligning torque) [100] can all express

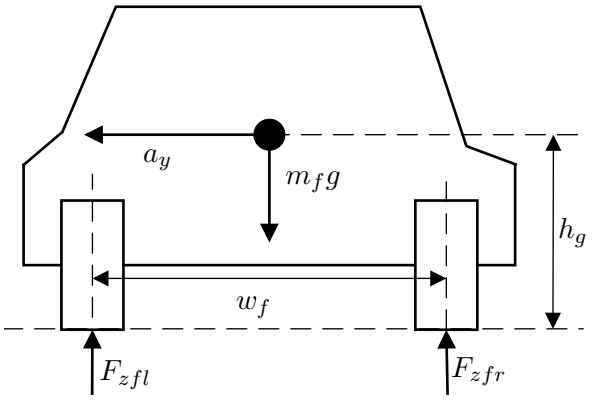

Figure 3.2.: Load transfer in the front axle during cornering

the tire characteristics and they are compared in table. 3.1. As can be seen, both brush model and TMsimple/TMeasy are simpler than magic formula in real implementation. However, they have less available parameters than magic formula in describing the tire characteristics. In other words, magic formula has higher possibility to describe the real tire characteristics since there are more parameters available for tuning. Due to the same reason, TMsimple/TMeasy are more flexible than brush model in accurately expressing the tire self-aligning torque characteristics. Therefore, by comprehensively considering the simplicity in implementation and available parameters in accurately capturing tire characteristics, tire models TMsimple/TMeasy are chosen.

Table 3.1.: Comparison of different tire models. Ratings: ++... *higher*; +... *high*; −... *low*.

	Magic Formula	**Brush Model**	**TMsimple/TMeasy**
Simplicity for implementation	−	+	+
Available parameters to describe tire lateral force characteristics	++	+	+
Available parameters to describe tire self-aligning torque characteristics	++	−	+

Tire lateral force F_y of TMsimple can be expressed as a function of tire slip angle α and tire-road friction coefficient μ_{max} [47]:

$$F_y = -K \sin[B(1 - e^{\frac{-|\alpha|}{A}})\text{sign}(\alpha)] \tag{3.7}$$

with

$$\begin{aligned} K &= Y_{\max} \\ B &= \pi - \arcsin(Y_\infty / Y_{\max}) \quad (Y_\infty \leq Y_{\max}) \\ A &= (1/dY_0)KB, \end{aligned} \tag{3.8}$$

where $Y_{\max}$, Y_∞ as well as dY_0, as shown in Fig. 3.3, refer to the maximum lateral force, the saturation lateral force and initial stiffness, respectively. $Y_{\max}$ and Y_∞ are proportional to the $\mu_{\max}$ which, however, does not influence dY_0. They are all related to normal force F_z and are expressed as follows:

$$\begin{aligned} Y_{\max}(F_z, \mu_{\max}) &= \left(a_1 \frac{F_z}{F_{z,nom}} + a_2 \left(\frac{F_z}{F_{z,nom}} \right)^2 \right) \cdot \frac{\mu_{\max}}{\mu_0} \\ dY_0(F_z) &= b_1 \frac{F_z}{F_{z,nom}} + b_2 \left(\frac{F_z}{F_{z,nom}} \right)^2 \\ Y_\infty(F_z, \mu_{\max}) &= \left(c_1 \frac{F_z}{F_{z,nom}} + c_2 \left(\frac{F_z}{F_{z,nom}} \right)^2 \right) \cdot \frac{\mu_{\max}}{\mu_0}, \end{aligned} \tag{3.9}$$

where $F_{z,nom}$ refers to nominal tire load; μ_0 is the nominal value of the tire-road friction coefficient; a_1, a_2, b_1, b_2, c_1, c_2 are derived based on the measurements of $Y_{\max}(F_{z,nom}, \mu_0)$, $Y_{\max}(F_{z,2nom}, \mu_0)$, $dY_0(F_{z,nom})$, $dY_0(F_{z,2nom})$, $Y_\infty(F_{z,nom}, \mu_0)$, $Y_\infty(F_{z,2nom}, \mu_0)$ under nominal tire load ($F_{z,nom}$) and an extra tire load[3] ($F_{z,2nom}$) as

[3]Usually this extra tire load is double the nominal tire load, but other values are also possible. The principle for selecting this extra tire load is to allow the variation range of tire normal force in the real application within the nominal tire load and this extra tire load.

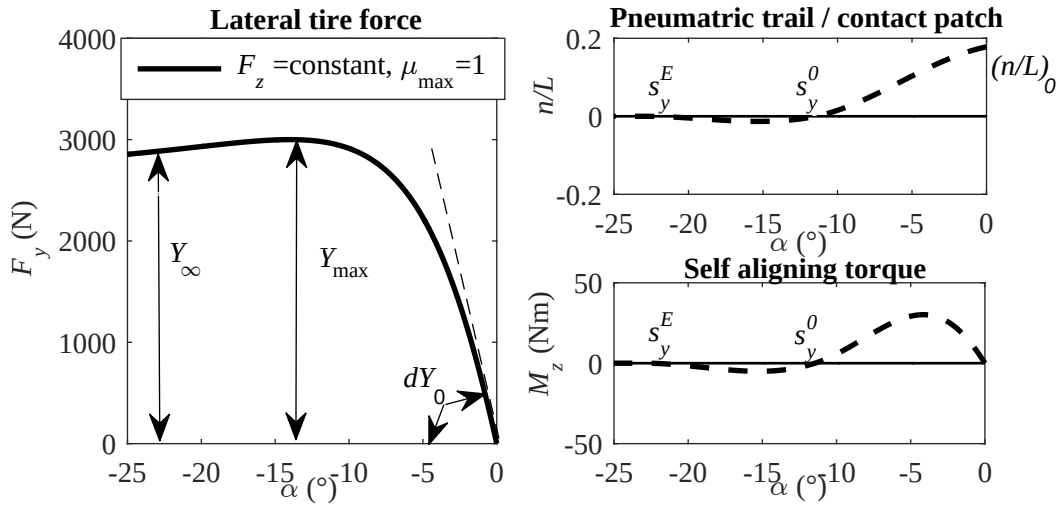

Figure 3.3.: Example of a passenger car tire characteristics under constant normal force and tire-road friction coefficient

well as nominal tire-road friction (μ_0), and expressed as

$$\begin{aligned}
a_1 &= \frac{Y_{\max}(F_{z,nom},\mu_0)r_{rat}^2 - Y_{\max}(F_{z,2nom},\mu_0)}{r_{rat}^2 - r_{rat}} \\
a_2 &= \frac{Y_{\max}(F_{z,2nom},\mu_0) - Y_{\max}(F_{z,nom},\mu_0)r_{rat}}{r_{rat}^2 - r_{rat}} \\
b_1 &= \frac{dY_0(F_{z,nom})r_{rat}^2 - dY_0(F_{z,2nom})}{r_{rat}^2 - r_{rat}} \\
b_2 &= \frac{dY_0(F_{z,2nom}) - dY_0(F_{z,nom})r_{rat}}{r_{rat}^2 - r_{rat}} \\
c_1 &= \frac{Y_\infty(F_{z,nom},\mu_0)r_{rat}^2 - Y_\infty(F_{z,2nom},\mu_0)}{r_{rat}^2 - r_{rat}} \\
c_2 &= \frac{Y_\infty(F_{z,2nom},\mu_0) - Y_\infty(F_{z,nom},\mu_0)r_{rat}}{r_{rat}^2 - r_{rat}}
\end{aligned} \tag{3.10}$$

where $r_{rat} = F_{z,2nom}/F_{z,nom}$.

After formulation of the tire lateral force, it comes to the self-aligning torque shown in Fig. 3.3 and is represented as

$$M_z = F_y \cdot n. \tag{3.11}$$

Instead of directly expressing the pneumatic trail n, TMeasy introduces a normalized pneumatic trail — $\frac{n}{L}$ (pneumatic trail above contact length L), which is represented as

$$\begin{aligned} \frac{n}{L} &= (\frac{n}{L})_0[(1-w)(1-|s|)+w(1-(3-2|s|)s^2)] && |s| \le 1 \\ \frac{n}{L} &= (\frac{n}{L})_0[-(1-w)(|s|-1)(\frac{1-w|s|}{1-w})^2] && 1 < |s| \le \frac{1}{w} \\ \frac{n}{L} &= 0 && |s| > \frac{1}{w}, \end{aligned} \tag{3.12}$$

where $(\frac{n}{L})_0$ the initial value of the pneumatic trail divided by the contact length, $s = \frac{\alpha\mu_0}{s_y^0\mu_{\max}}$, $w = \frac{s_y^0}{s_y^E}$. The $(\frac{n}{L})_0$ is influenced by normal force F_z and can be expressed by linear interpolation on two points $(\frac{n}{L})_0(F_{z,nom})$ as well as $(\frac{n}{L})_0(F_{z,2nom})$:

$$(\frac{n}{L})_0(F_z) = (\frac{n}{L})_0(F_{z,nom}) + \frac{(\frac{n}{L})_0(F_{z,2nom}) - (\frac{n}{L})_0(F_{z,nom})}{F_{z,2nom} - F_{z,nom}}(F_z - F_{z,nom}). \tag{3.13}$$

The $(\frac{n}{L})_0(F_{z,nom})$ and $(\frac{n}{L})_0(F_{z,2nom})$ are estimated by fitting the measurement data under $F_{z,nom}$ and $F_{z,2nom}$. s_y^0 and s_y^E are determined by normal force (F_z) and $(\mu_{\max})$ and can be expressed as

$$\begin{aligned} s_y^0(F_z,\mu_{\max}) &= \Big(s_y^0(F_{z,nom},\mu_0) + \frac{s_y^0(F_{z,2nom},\mu_0) - s_y^0(F_{z,nom},\mu_0)}{F_{z,2nom} - F_{z,nom}}(F_z - F_{z,nom})\Big)\frac{\mu_{\max}}{\mu_0} \\ s_y^E(F_z,\mu_{\max}) &= \Big(s_y^E(F_{z,nom},\mu_0) + \frac{s_y^E(F_{z,2nom},\mu_0) - s_y^E(F_{z,nom},\mu_0)}{F_{z,2nom} - F_{z,nom}}(F_z - F_{z,nom})\Big)\frac{\mu_{\max}}{\mu_0}, \end{aligned}$$

where $s_y^0(F_{z,nom},\mu_0)$, $s_y^0(F_{z,2nom},\mu_0)$, $s_y^E(F_{z,nom},\mu_0)$, $s_y^E(F_{z,2nom},\mu_0)$ are estimated by fitting the measurement data under nominal tire load $(F_{z,nom})$ and the extra tire load $(F_{z,2nom})$ as well as nominal tire-road friction (μ_0).

After obtaining $\frac{n}{L}$, we also need to calculate contact length L. According to [100], L is approximated as:

$$L \approx 2\sqrt{\frac{r_0 F_z}{c_z}}, \tag{3.14}$$

where r_0 is the unloaded tire radius, c_z the vertical stiffness.

3.3. Steering system model and total aligning torque estimation

3.3.1. Steering system model

More and more vehicles are equipped with electric power steering systems (EPS) or active front steering systems (AFS), allowing for estimation of front axle total aligning torque (contains self-aligning torque information) [10, 51, 85]. In this research, instead of utilizing EPS or AFS information, strain gauge sensors are installed on the tie rod of the steering system to estimate total aligning torque information, and thus the steering system shown in Fig. 3.4 can be written in a similar way like [10] as

$$\tau_g(t) = F_l(t)L_l(\delta) - F_r(t)L_r(\delta) \tag{3.15}$$

$$J_s\ddot{\delta} + k_s\dot{\delta} = \tau_g(t) - \tau_{zf}(t) \tag{3.16}$$

with

$$\tau_{zf}(t) = M_{zfl} + M_{zfr} + (F_{yfl} + F_{yfr})d_c, \tag{3.17}$$

where J_s is the effective moment of inertia of steering system, k_s the effective damping of steering system, δ the wheel steering angle, $\tau_{zf}(t)$ the total aligning torque, $\tau_g(t)$ the aligning torque caused by $F_l(t)$ and $F_r(t)$ which are the tie rod forces on the left and right sides measured by strain gauge sensors, $L_l(\delta)$ and $L_r(\delta)$ are the vertical distances between the tie rod to the kingpin separately which vary with steering angle, M_{zfl} and M_{zfr} the front left and right self-aligning torque separately, F_{yfl} the front left lateral force, F_{yfr} the front right lateral force, d_c the mechanical trail of front tires which is assumed to be the same for both front left and right tires. It has to be mentioned that the contribution of jacking torque here can be omitted since the jacking torque caused by the vertical load on the right and left wheels are mutually cancelled [85].

3.3.2. Total aligning torque estimation

For estimation of $\tau_{zf}(t)$ based on equation (3.16), an unknown input observer (UIO) is implemented in [10] by assuming the dynamic variation of τ_{zf} is slow or invariant. In this work, since the signal of wheel steering angle δ is smooth, its first and second numerical differentiation will be used to represent the total aligning torque, which is demonstrated

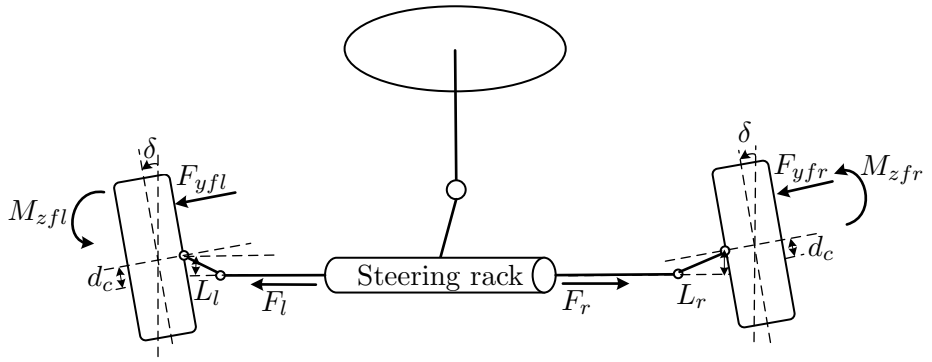

Figure 3.4.: Steering system

as follows:

$$\hat{\tau}_{zf}(t) = F_l(t)L_l(\delta) - F_r(t)L_r(\delta) - J_s\ddot{\delta} - k_s\dot{\delta}, \tag{3.18}$$

where $\hat{\tau}_{zf}(t)$ is the estimation of total aligning torque.

4. Tire-road friction coefficient estimation with tire self-aligning torque

4.1. Introduction

This chapter introduces two methods for estimating $\mu_{\max}$ based on self-aligning torque.

Method I proposes a framework to estimate the tire-road friction coefficient with asymptotic stability and reliability guarantee using the total aligning torque of the front axle during steering. A novel strategy is firstly adopted to estimate the front axle lateral force which performs better than the classical unknown input observer (UIO) [94]. Then, combined with an indirect measurement based on the estimated total aligning torque and front axle lateral force, a nonlinear adaptive observer is designed to estimate $\mu_{\max}$ with asymptotic stability guarantee. To increase the reliability of the estimation result, criteria are proposed to decide when to update the estimated $\mu_{\max}$.

Though method I is simple to implement, the indirect measurement is singular when the total aligning torque approaches zero. Meanwhile, front axle lateral force needs to be extra estimated. Therefore, a method II, aiming at eliminating aforementioned shortcomings, is proposed. **Method II** proposes a nonlinear adaptive observer to estimate tire-road friction coefficient with no need to estimate the front axle lateral force. Firstly, the vehicle lateral dynamics model is transformed into a lower-triangular form with yaw rate, x_f (front axle tire slip angle over $\mu_{\max}$) and $\mu_{\max}$ as state variables. Then, for non-affine parametrized systems in such a form, a nonlinear adaptive observer was proposed and its estimation error was proved to be exponentially stable by constructing a strict Lyapunov function. Furthermore, the design procedure is applied to the $\mu_{\max}$ estimation problem with proper modifications. It has to be mentioned that the proposed nonlinear adaptive observer is universally applicable if other dynamic systems featuring the same system form (a lower-triangular form) satisfy the corresponding assumptions for this observer.

Finally, $\mu_{\max}$ estimation results between **method I** and **method II** as well as Extended Kalman Filter (EKF) are demonstrated and compared in both simulations and experiments. The results show that both **method I** and **method II** can guarantee stability of $\mu_{\max}$ estimation in a wider range of vehicle operations than EKF. Furthermore, in terms of root mean square of $\mu_{\max}$ estimation error[1] (RMS), the performance from **method I**, **method II** and EKF (in stable situation) is overall similar. Moreover, **method I** and **method II** are both real time capable. It has to be mentioned that in this chapter, **method I** and **method II** are short for AVE and NAO, respectively.

4.2. Model transformation

4.2.1. Tire model transformation

Introducing the state variable $x = \alpha/\mu_{\max}$, the tire models in (3.7) and (3.11) can then be rewritten as

$$\begin{aligned} F_y &= \mu_{\max} \cdot f(x), \\ M_z &= \mu_{\max} \cdot g(x), \end{aligned} \tag{4.1}$$

which decouples x and $\mu_{\max}$ in the expression of F_y and M_z. It can be noted that other tire models like brush model, magic formula[2], dugoff tire model can also be written in this form.

Then the tire characteristics in Fig. 4.1 are obtained under a constant normal force with the new abscissa x. With respect to the tire self-aligning torque in Fig. 4.1, it can be deduced that the peak of M_z is at the same value of $x = x_o$ independent of $\mu_{\max}$. In addition, the smaller $|x|$ is, the closer the relationship of $|x|$ to M_z is to a linear one, making a possible estimation of $\mu_{\max}$ in this area less accurate. In this work, $|x| \leq x_c$ is used to indicate the quasi-linear region. In this way, the excitation of lateral dynamics can be detected by checking whether the value of x is pushed into the nonlinear region of tire self-aligning torque regardless of the road conditions. Although the values of x for the peak and the end of the linear region differ, this assumption for the linear region also holds for F_y over x. For different tire normal force, the values of x_c and x_o vary, however,

[1] RMS is a common index to measure the quality of estimation result and is widely used in the vehicle states estimation [14, 93].

[2] For the magic formula, the influence of horizontal and vertical shift on the tire lateral force and self-aligning torque are omitted [90].

if we assume the longitudinal velocity changes slowly, leading to a negligible longitudinal load transfer, both x_c and x_o change little for the overall front tire lateral force and self-aligning torque in the front axle (especially for low tire-road friction coefficient[3]) and can be assumed constant for this application [103].

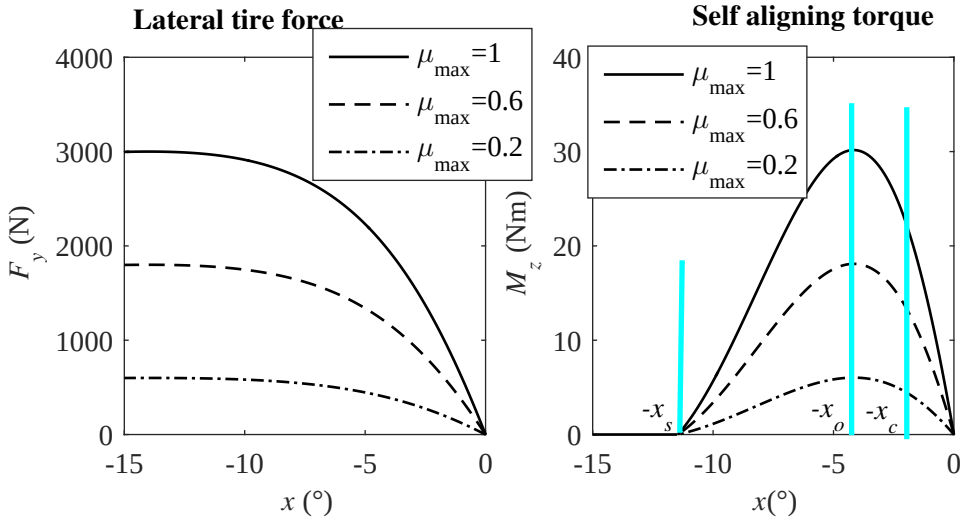

Figure 4.1.: F_y and M_z varies with x in different μ_{max} for a constant normal force [115]

4.2.2. Vehicle model transformation

Using the relationship $\alpha_f = \beta + \frac{l_f \omega}{v_x} - \delta$, the single track model (3.1) can be transformed into

$$\dot{\omega} = \frac{l_f F_{yf} \cos\delta}{I_z} - \frac{l_r F_{yr}}{I_z}, \tag{4.2a}$$

$$\dot{\alpha}_f = aF_{yf} + bF_{yr} - \omega - \dot{\delta}, \tag{4.2b}$$

where $a = \frac{1}{mv_x} + \frac{l_f^2}{I_z v_x}$, $b = \frac{1}{mv_x} - \frac{l_f l_r}{I_z v_x}$. With $F_{yr} = ma_y - F_{yf}\cos\delta$, following equations

$$\dot{\omega} = \frac{lF_{yf} \cos\delta}{I_z} - \frac{l_r m a_y}{I_z}, \tag{4.3a}$$

$$\dot{\alpha}_f = (a-b)(cos\delta)F_{yf} + bma_y - \omega - \dot{\delta} \tag{4.3b}$$

[3] On low $\mu_{\max}$ condition, the vehicles have small lateral acceleration, resulting in less lateral road transfer and thus less normal force variation.

are deduced. Applying the result from (4.1) to the vehicle front axle and considering the lateral load transfer,

$$\begin{aligned} F_{yf} &= \mu_{\max} \cdot f_f(x_f, t), \\ M_{zf} &= \mu_{\max} \cdot g_f(x_f, t), \end{aligned} \tag{4.4}$$

are obtained, where $x_f = \frac{\alpha_f}{\mu_{\max}}$, $f_f(x_f, t) := f_{fl}(x_f, t) + f_{fr}(x_f, t)$, $g_f(x_f, t) := g_{fl}(x_f, t) + g_{fr}(x_f, t)$, fl and fr denote front left and front right, respectively.

Combining (3.17) and (4.4),

$$\mu_{\max} = \frac{\tau_{zf}}{g_f(x_f) + f_f(x_f) d_c} \tag{4.5}$$

is obtained, finally transforming (3.1) into

$$\begin{aligned} \dot{\omega} &= \frac{l \tau_{zf} m_v \cos(\delta) - l_r m a_y}{I_z} \\ &\quad + \frac{-|\tau_{zf}| l \cos(\delta)}{I_z} \left(\frac{f_f(x_f)}{g_f(x_f) + f_f(x_f) d_c} - m_v \right) \text{sign}(x_f), \end{aligned} \tag{4.6a}$$

$$\dot{x}_f = (a - b)(cos\delta) f_f(x_f) + (b m a_y - \omega - \dot{\delta}) \frac{1}{\mu_{\max}}, \tag{4.6b}$$

where $m_v = \lim_{x_f \to 0} \frac{f_f(x_f)}{g_f(x_f) + f_f(x_f) d_c}$. Details of the transformation can be found in Appx. B.

4.3. Method I: $\mu_{\max}$ estimation with front axle tire lateral force estimation

4.3.1. Front axle tire lateral force estimation

According to (4.3a),

$$\begin{aligned} \dot{\omega} &= \frac{l F_{yf} \cos \delta}{I_z} - \frac{l_r m a_y}{I_z}, \\ \dot{F}_{yf} &= p_1(t) \end{aligned} \tag{4.7}$$

is obtained, where a_y is the lateral acceleration and $p_1(t)$ the derivative of F_{yf}.

Usually, for estimating F_{yf}, classical UIO can be applied as follows:

$$\begin{aligned} \dot{\hat{\omega}} &= \frac{l\hat{F}_{yf}\cos\delta}{I_z} - \frac{l_r m a_y}{I_z} + k_1(\omega - \hat{\omega}), \\ \dot{\hat{F}}_{yf} &= k_2(\omega - \hat{\omega}), \end{aligned} \tag{4.8}$$

where k_1 and k_2 are the positive constants. The corresponding error dynamics is

$$\begin{aligned} \dot{\tilde{\omega}} &= \frac{l\tilde{F}_{yf}\cos\delta}{I_z} - k_1\tilde{\omega}, \\ \dot{\tilde{F}}_{yf} &= -k_2\tilde{\omega} + p_1(t). \end{aligned} \tag{4.9}$$

Therefore, the steady state estimation error of F_{yf} is

$$\tilde{F}_{yf} = \frac{k_1 I_z p_1(t)}{l k_2 \cos\delta}. \tag{4.10}$$

Since k_2 cannot be set infinite large due to the yaw rate measurement noise, a novel strategy is introduced to reduce the estimation error of the front axle tire lateral force without changing UIO gains, which is

$$\hat{F}_{yf,ave} = \frac{\hat{F}_{yf} + (m a_y - \hat{F}_{yr})/\cos\delta}{2}, \tag{4.11}$$

where $\hat{F}_{yr}$ is the estimated rear axle tire lateral force, observed in a similar way. The corresponding steady state estimation error of F_{yr} is

$$\tilde{F}_{yr} = -\frac{k_3 I_z p_2(t)}{l k_4}, \tag{4.12}$$

where k_3 is a positive and k_4 is a negative constant, $p_2(t)$ the derivative of rear axle tire lateral force. The overall observer for the front axle tire lateral force is summarized in Table 4.1. The corresponding steady state estimation error is

$$\begin{aligned} \tilde{F}_{yf,ave} &= F_{yf} - \hat{F}_{yf,ave} \\ &= F_{yf} - \frac{\hat{F}_{yf} + (F_{yf}\cos\delta + F_{yr} - \hat{F}_{yr})/\cos\delta}{2} \\ &= \frac{F_{yf} - \hat{F}_{yf}}{2} - \frac{F_{yr} - \hat{F}_{yr}}{2\cos\delta} \\ &= \frac{I_z}{2l\cos\delta}\left(\frac{k_1 p_1(t)}{k_2} + \frac{k_3 p_2(t)}{k_4}\right). \end{aligned} \tag{4.13}$$

Table 4.1.: Summary of F_{yf} estimation

F_{yf} **estimation summary**
$\begin{cases} \dot{\hat{\omega}} = \frac{l\hat{F}_{yf}\cos\delta}{I_z} - \frac{l_r m a_y}{I_z} + k_1(\omega - \hat{\omega}) \\ \dot{\hat{F}}_{yf} = k_2(\omega - \hat{\omega}) \\ \dot{\hat{\omega}}_r = \frac{l_f m a_y}{I_z} - \frac{l\hat{F}_{yr}}{I_z} + k_3(\omega - \hat{\omega}_r) \\ \dot{\hat{F}}_{yr} = k_4(\omega - \hat{\omega}_r) \\ \hat{F}_{yf,ave} = \frac{\hat{F}_{yf} + (m a_y - \hat{F}_{yr})/\cos\delta}{2}. \end{cases}$

Dividing (4.13) by (4.11),

$$\frac{|\tilde{F}_{yf,ave}|}{|\tilde{F}_{yf}|} = \frac{|1 + \frac{k_2 k_3}{k_1 k_4}\frac{p_2(t)}{p_1(t)}|}{2} \tag{4.14}$$

is obtained. For this application, $\frac{k_2 k_3}{k_1 k_4}$ is set to be -1 to guarantee similar performance of UIOs for front axle and rear axle tire lateral force estimation. Therefore, as long as $-1 \leq \frac{p_2(t)}{p_1(t)} \leq 3$, $|\tilde{F}_{yf,ave}| \leq |\tilde{F}_{yf}|$ can be guaranteed.

In the following, simulations will be used to demonstrate that $-1 \leq \frac{p_2(t)}{p_1(t)} \leq 3$ holds most of the time with typical driving maneuvers. Before conducting these simulations, an evaluation criteria p_v is introduced which demonstrates ratio of time when $\frac{p_2(t)}{p_1(t)}$ is within -1 and 3 to overall simulation time during one simulation, see in Fig.4.2. The maneuvers chosen for simulations are step steer, sinusoidal input as well as double lane change [1]. The dimensions of the input space for these maneuvers are different, for instance, there are three input variables for the step steer and four for the sinusoidal maneuver, which are longitudinal velocity v_x, amplitude of the front wheel steering angle δ_a as well as tire-road friction coefficient μ_{max} (common for both maneuvers) and steering frequency (additional for sinusoidal maneuver). On the contrary, the dimensions of the input space for double lane change are 2 (v_x and μ_{max}).

Now it comes to the conduction of simulation maneuvers. For lowing the simulation effort in step steer, one of these three variables (v_x, δ_a and μ_{max}) is fixed in each time and then the relationship between p_v and the rest two are studied. The chosen fixed values are selected as $\mu_{max} = 1$, $v_x = 20$ m/s, $\delta_a = 0.03$ rad, so that the maximum lateral acceleration is approximate 4 m/s^2 which is recommended in the standard [1]. The duration time starts from the execution of the step steer and ends with recovery of stability (about 5% variation around steady yaw rate) of the vehicle. The results can be

seen in Fig. 4.3. It has to be mentioned that only surface surrounded by line segments without intersecting with plane $p_v = 0$ is valid, since other parts are too aggressive to be simulated, which also holds for sinusoidal and double lane change maneuvers. In Fig. 4.3, it can be concluded that p_v apparently exceeds 50% and is actually larger than 80% which means $-1 \leq \frac{p_2(t)}{p_1(t)} \leq 3$ holds in most of the simulation time. In a next step, sinusoidal inputs are considered. Since during the transient process of the step steer the behavior of the vehicle is close to that of a vehicle in sinusoidal maneuver, frequency influence is focused on shown in right down side of fig. 4.3. As can be seen, the higher the frequency is, the lower p_v is, but still much larger than 50%. Finally double lane change maneuver is simulated. As illustrated in fig. 4.4, with increasing of v_x, p_v drops for fixed μ_{max}, while p_v is robust to μ_{max} when v_x is fixed. Overall speaking, based on p_v analysis with simulation, it can be demonstrated that the proposed strategy works better than classical UIO for front axle tire lateral force estimation.

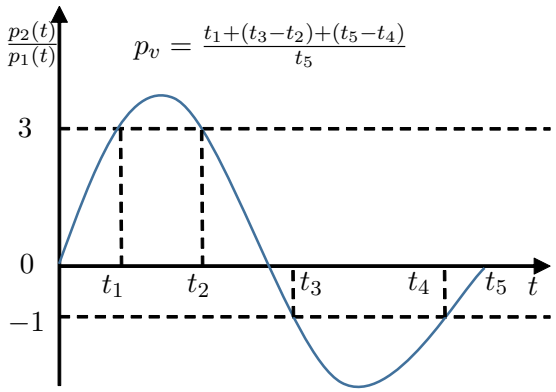

Figure 4.2.: Demonstration of how to calculate p_v.

In order to more intuitively demonstrate F_{yf} estimation quality of the proposed novel estimation strategy, some exemplary comparison is shown, between the proposed strategy and classical UIO considering the variation of $\mu_{\max}$ and velocity as well as the amplitude of the front wheel steering angle. Three different maneuvers—the sinusoidal, the step steer and the double lane change—are performed and the results are illustrated in Fig. 4.5. As can be seen, the estimation errors from $\hat{F}_{yf,ave}$ with the proposed estimation strategy are smaller than those from $\hat{F}_{yf,nor}$ with classical UIO most of the time in all three maneuvers, which also verifies the p_v simulation analysis.

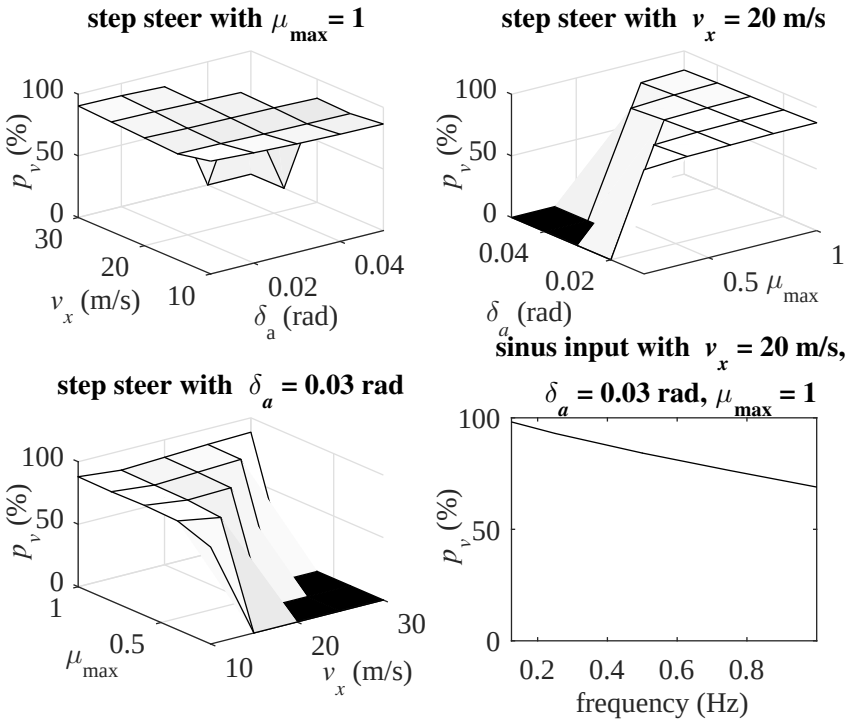

Figure 4.3.: Characteristics of p_v with respect to input space variables at step steer and sinusoidal maneuvers are simulated.

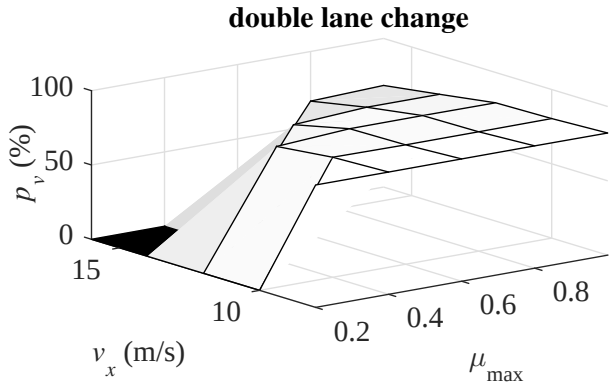

Figure 4.4.: Characteristics of p_v with respect to input space variables at double lane change maneuver are simulated.

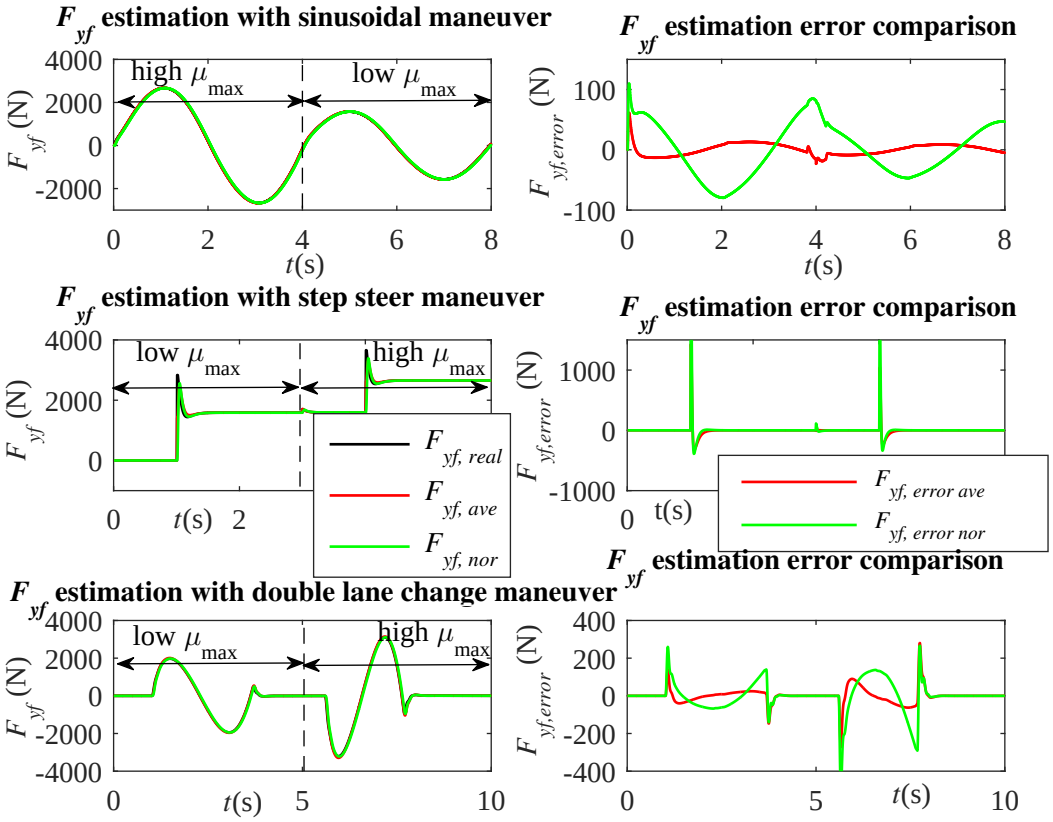

Figure 4.5.: The results for the F_{yf} estimation in three different driving maneuvers. Three different maneuvers—sinusoidal, step steer and double lane change—are illustrated. Sinusoidal maneuver is conducted from high friction with $v_x = 20$ m/s to low friction road condition with $v_x = 15$ m/s. The step steer maneuver is carried out from low friction to high friction road condition: $v_x = 15$ m/s. Under low friction road condition, the front wheel steering angle jumps from 0 to 0.03 rad and then from 0.03 rad to 0.05 rad under high friction road condition. Double lane change maneuver is performed from low friction to high friction road condition: $v_x = 12$ m/s. The estimation result with "ave" and "nor" are based on the proposed F_{yf} estimation strategy and the classical UIO estimation, respectively.

4.3.2. Nonlinear adaptive observer for $\mu_{\max}$ estimation

4.3.2.1. Nonlinear adaptive observer design

After estimating the front axle lateral force and total aligning torque,

$$\begin{aligned} \hat{F}_{yf,ave} &= \mu_{\max} \cdot f_f(x_f, t), \\ \tau_{zf} &= \mu_{\max} \cdot (g_f(x_f, t) + f_f(x_f, t) d_c) \end{aligned} \tag{4.15}$$

are obtained. Then how to utilize these information for an observer, such that the designed one can be guaranteed to be stable, is critical. According to summary of observer design in 2.3.1, directly incorporating these information in an observer seems difficult. In the authors' previous work [102], convex optimization was firstly used to solve x_f online, subsequently it was applied as a measurement in an adaptive observer. However, the convex optimization needs high calculation effort. To avoid this, an indirect measurement possessing monotonicity property w.r.t. x_f and demonstrated in (4.16) is introduced, which is simple to be implemented in an adaptive observer[55, 40].

$$\begin{aligned} y(x_f, t) &= (\frac{f_f(x_f, t)}{g_f(x_f, t) + f_f(x_f, t) d_c} - m_v)\text{sign}(x_f) \\ &= (\frac{\hat{F}_{yf,ave}}{\tau_{zf}} - m_v)\text{sign}(-\hat{F}_{yf,ave}), \end{aligned} \tag{4.16}$$

where $m_v = \lim_{x_f \to 0} \frac{f_f(x_f,t)}{g_f(x_f,t)+f_f(x_f,t)d_c}$ and $y(x_f, t)$ is a monotonic increasing odd function (between $-x_s$ and x_s) with respect to x_f and uniformly to t, see in Fig. 4.6. However, the indirect measurement $y(x_f, t)$ is confronted with singularity problem when τ_{zf} is close to zero, so some processing is needed to improve the quality of $y(x_f, t)$ and can be described as follows:

if $|\hat{F}_{yf,ave}| \leq F_{yf,\text{thres}}$ | $|\tau_{zf}| \leq \tau_{\text{thres}}$ | $\text{sign}(\tau_{zf} - \hat{F}_{yf,ave} \cdot d_c) \neq \text{sign}(\hat{F}_{yf,ave})$
| $|\hat{F}_{yf,ave}| < |\tau_{zf} \cdot m_v|$
$y = 0, k_a = 0, k_b = 0;$
else
$y = y(x_f, t); k_a = k_a; k_b = k_b(t);$
end

where τ_{thres}, $F_{yf,\text{thres}}$ are thresholds to judge whether the estimated total aligning torque and front axle lateral force are close to zero or not. The term $\text{sign}(\tau_{zf} - \hat{F}_{yf,ave} \cdot d_c) \neq$

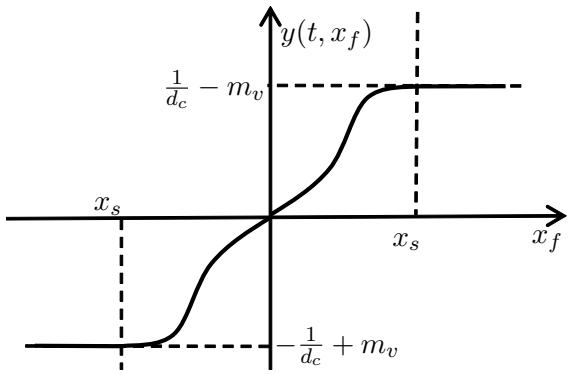

Figure 4.6.: Indirect measurement $y(x_f, t)$ with respect to x_f. Between $-x_s$ and x_s (as shown in fig. 4.1), $y(x_f, t)$ is monotonic increasing odd function, otherwise it is constant.

$\text{sign}(\hat{F}_{yf,ave})$ is to detect whether the front axle self-aligning torque and the front axle lateral force have the same sign. Theoretically speaking, they should be the same, but when both of the estimated values are close to zero, the sign may differ due to estimation error of $\hat{F}_{yf,ave}$ or numerical error. W.r.t. the condition $|\hat{F}_{yf,ave}| < |\tau_{zf} \cdot m_v|$, if it is respected, there is no solution in the tire model because $|\hat{F}_{yf,ave}|$ should be equal or larger than $|\tau_{zf} \times m_v|$. If one of the proposed conditions is satisfied, $y(x_f, t) = 0, k_a = 0, k_b = 0$ are set, where k_a and k_b are gains for the nonlinear adaptive observer and will be described in the following.

Based on this indirect measurement and the model given in (4.6b), following system

$$\begin{aligned} \dot{x}_f &= c_1(t) f_f(x_f, t) + c_2(t)\theta, \\ \dot{\theta} &= 0, \\ y &= y(x_f, t) \end{aligned} \tag{4.17}$$

is considered, where $c_1(t) = (a - b)(\cos\delta) > 0$, $c_2(t) = bma_y - \omega - \dot{\delta}$, $x_f \in \Theta_1 \subset \mathbb{R}$, $\Theta_1 = \{x_f \in \mathbb{R} | -x_s \leq x_f \leq x_s\}$, x_s is constant as shown in Fig. 4.1, $\theta = \frac{1}{\mu_{\max}}$ and $\theta \in \Theta_2 \subset \mathbb{R}$ with $\Theta_2 = \{\theta \in \mathbb{R} | 0.8 \leq \theta \leq 10\}$, Θ_1 and Θ_2 are compact sets.

The corresponding observer is

$$\begin{aligned} \dot{\hat{x}}_f &= c_1(t) f_f(\hat{x}_f, t) + c_2(t)\hat{\theta} + k_a(y - y(\hat{x}_f, t)), \\ \dot{\hat{\theta}} &= k_b(t) \frac{\partial y(\hat{x}_f, t)}{\hat{x}_f} c_2(t)(y - y(\hat{x}_f, t)), \end{aligned} \tag{4.18}$$

where k_a is a positive constant, while $k_b(t)$ is $\frac{k_c}{\max(|c_2(t)|,\epsilon)}$ with k_c and ϵ both being positive constant, such that the convergent rate of $\hat{\theta}$ to the real θ will be less influenced by the time varying $c_2(t)$. Then, the corresponding error dynamics is

$$\begin{aligned} \dot{\tilde{x}}_f &= c_1(t)(f_f(x_f,t) - f_f(\hat{x}_f,t)) + c_2(t)(\theta - \hat{\theta}) - k_a(y - y(\hat{x}_f,t)) \\ \dot{\tilde{\theta}} &= -k_b(t)\frac{\partial y(\hat{x}_f,t)}{\hat{x}_f}c_2(t)(y - y(\hat{x}_f,t)), \end{aligned} \tag{4.19}$$

where $\tilde{x}_f = x_f - \hat{x}_f$ and $\tilde{\theta} = \theta - \hat{\theta}$

4.3.2.2. Stability analysis

For the stability analysis, the following assumptions and properties need to be introduced.

Assumption 4.3.1. *For all* $(t, x_f, \hat{x}_f, \tilde{x}_f) \in \mathbb{R}_{\geq 0} \times \Theta_1 \times \mathbb{R} \times (\Theta_1 - \mathbb{R})$,

$$k_{y,low}\tilde{x}_f \leq \tilde{y}(\tilde{x}_f,t) \tag{4.20}$$

where $k_{y,low}$ *is a positive constant and* $\tilde{y}(\tilde{x}_f,t) = y(x_f,t) - y(\hat{x}_f,t)$

Remarks. *This is a Lipschitz condition to make the variation of* $y(x_f,t)$ *w.r.t.* x_f *always bounded by* $k_{y,low}$*. With this assumption, it is required that, when* x_f *reaches the boundary of set* Θ_1 *in very aggressive situation (rarely occurs),* $\hat{x}_f$ *should stay in the interior of set* Θ_1 *for guaranteeing the Lipschitz condition. This assumption can be actually replaced by implementing some projection techniques to restrict* $\hat{x}_f$ *within a boundary [75]. In this thesis, for simplicity, instead of taking the proposed measure, the Assumption 4.3.1 is directly presented. However, this is already far more enough for tire-road friction estimation.*

Assumption 4.3.2. *Suppose that there exists positive scales* T_1*,* ϵ_1 *and* ϵ_2*, such that, for all* $t \in R_{\geq 0}$*, we have*

$$\epsilon_1 \leq \int_t^{t+T_1} c_2^2(\tau)d\tau \leq \epsilon_2, \tag{4.21}$$

with $c_2(t)$*,* $\dot{c}_2(t) \in L_\infty$*.*

Remarks. *Assumption 4.3.2 indicates a persistent excitation condition, which is a common assumption for parameter estimation. Besides, the assumption of* L_∞ *for* $c_2(t)$*,*

$\dot{c}_2(t)$ is to guarantee the boundedness of $k_b(t)$ as well as $\dot{k}_b(t)$, which will be described in Property 4.3.2 in the following.

Property 4.3.1. *Suppose that assumption 4.3.1 holds, then for all $(t, x_f, \hat{x}_f, \tilde{x}_f) \in \mathbb{R}_{\geq 0} \times \Theta_1 \times \mathbb{R} \times (\Theta_1 - \mathbb{R})$, we have*

$$k_{y,low}\tilde{x}_f \quad \leq \quad \tilde{y}(\tilde{x}_f, t) \quad \leq \quad k_{y,upp}\tilde{x}_f, \tag{4.22}$$

and

$$||f_f(x_f) - f_f(\hat{x}_f)|| \quad \leq \quad k_f||\tilde{x}_f||, \tag{4.23}$$

where $k_{y,upp}$ and k_f are positive constants.

Property 4.3.2. *Suppose that assumption 4.3.2 holds, then we have*

$$\rho_1 \quad \leq \quad k_b(t) \quad \leq \quad \rho_2, \tag{4.24}$$

and

$$0 \quad \leq \quad ||\dot{k}_b(t)|| \quad \leq \quad \rho_3, \tag{4.25}$$

where ρ_1 and ρ_2 as well as ρ_3 are positive constants.

Property 4.3.3. *For all $(t, x_f, \hat{x}_f, \tilde{x}_f) \in \mathbb{R}_{\geq 0} \times \Theta_1 \times \mathbb{R} \times (\Theta_1 - \mathbb{R})$,*

$$||d_1(t, \tilde{x}_f)|| \quad \leq \quad l_1||\tilde{x}_f||^2, \tag{4.26}$$

where l_1 is a positive constant, $d_1(t, \tilde{x}_f) = 2k_b(t)(y(x_f, t) - y(\hat{x}_f, t))\Big((\frac{\partial y(x_f,t)}{\partial x_f} - \frac{\partial y(\hat{x}_f,t)}{\partial \hat{x}_f})\dot{x}_f + (\frac{\partial y(x_f,t)}{\partial t} - \frac{\partial y(\hat{x}_f,t)}{\partial t})\Big) + \dot{k}_b(t)(y(x_f, t) - y(\hat{x}_f, t))^2$.

Theorem 4.3.1. *Suppose that assumptions $1-2$ hold, then there exist a positive constant k_a and a bounded positive $k_b(t)$, such that if k_a is large enough, then $\tilde{x}_f \to 0, \quad \tilde{\theta} \to 0 \quad \text{as} \quad t \to \infty$ for $(\tilde{x}_f, \tilde{\theta}) \in (\Theta_1 - \mathbb{R}) \times (\Theta_2 - \mathbb{R})$.*

Proof. The Lyapunov function is defined as

$$V(\tilde{x}_f, t) \quad = \quad k_b(t)(y(x_f, t) - y(\hat{x}_f, t))^2 + \tilde{\theta}^2$$

Denote the vector $[\tilde{x}_f; \tilde{\theta}]$ by X and according to property 1,

$$\min(\rho_1 k_{y,low}^2, 1)X^2 \leq V(\tilde{x}_f, t) \leq \max(\rho_2 k_{y,upp}^2, 1)X^2 \tag{4.27}$$

is deduced, which indicates that $V(\tilde{x}_f, t)$ is radially unbounded. Subsequently,

$$\begin{aligned}
\dot{V} &= 2k_b(t)(y(x_f,t)-y(\hat{x}_f,t))\Big(\tfrac{\partial y(x_f,t)}{\partial x_f}\dot{x}_f - \tfrac{\partial y(\hat{x}_f,t)}{\partial \hat{x}_f}\dot{\hat{x}}_f \\
&\quad + \tfrac{\partial y(x_f,t)}{\partial t} - \tfrac{\partial y(\hat{x}_f,t)}{\partial t}\Big) + 2\tilde{\theta}\dot{\tilde{\theta}} + \dot{k}_b(t)(y(x_f,t)-y(\hat{x}_f,t))^2 \\
&= 2k_b(t)(y(x_f,t)-y(\hat{x}_f,t))\Big((\tfrac{\partial y(x_f,t)}{\partial x_f} - \tfrac{\partial y(\hat{x}_f,t)}{\partial \hat{x}_f})\dot{x}_f + \tfrac{\partial y(\hat{x}_f,t)}{\partial \hat{x}_f}\dot{\tilde{x}}_f \\
&\quad + (\tfrac{\partial y(x_f,t)}{\partial t} - \tfrac{\partial y(\hat{x}_f,t)}{\partial t})\Big) + 2\tilde{\theta}\dot{\tilde{\theta}} + \dot{k}_b(t)(y(x_f,t)-y(\hat{x}_f,t))^2 \\
&= 2k_b(t)(y(x_f,t)-y(\hat{x}_f,t))\tfrac{\partial y(\hat{x}_f,t)}{\partial \hat{x}_f}\dot{\tilde{x}}_f + 2\tilde{\theta}\dot{\tilde{\theta}} + d_1(t,\tilde{x}_f) \\
&= 2k_b(t)(y(x_f,t)-y(\hat{x}_f,t))\tfrac{\partial y(\hat{x}_f,t)}{\partial \hat{x}_f}\Big(c_1(t)(f_f(x_f)-f_f(\hat{x}_f)) - k_a(y-y(\hat{x}_f,t))\Big) \\
&\quad + 2k_b(t)(y(x_f,t)-y(\hat{x}_f,t))\tfrac{\partial y(\hat{x}_f,t)}{\partial \hat{x}_f}c_2(t)\tilde{\theta} \\
&\quad + 2\tilde{\theta}\Big(-k_b(t)\tfrac{\partial y(\hat{x}_f,t)}{\partial \hat{x}_f}c_2(t)(y-y(\hat{x}_f,t))\Big) + d_1(t,\tilde{x}_f) \\
&\leq -2k_ak_b(t)\tfrac{\partial y(\hat{x}_f,t)}{\partial \hat{x}_f}(y(x_f,t)-y(\hat{x}_f,t))^2 + 2k_b(t)c_1(t)k_{y,upp}^2k_f||\tilde{x}_f||^2 + l_1||\tilde{x}_f||^2 \\
&\leq (-2k_a\rho_1k_{y,low}^3 + 2\rho_2c_1(t)k_{y,upp}^2k_f + l_1)||\tilde{x}_f||^2.
\end{aligned} \tag{4.28}$$

Since $c_1(t)$ is positive and bounded, then if k_a is chosen large enough, there exists a positive constant k^*, such that

$$\dot{V}(X,t) \leq -k^*||\tilde{x}_f||^2. \tag{4.29}$$

According to theorem 8.4 barbalat lemma in [66], it can be deduced that

$$\tilde{x}_f \to 0 \quad \text{as} \quad t \to \infty.$$

Combined with Assumption 4.3.2 and applying Lemma A.1. from [22], it can be reasoned out that

$$\tilde{\theta} \to 0 \quad \text{as} \quad t \to \infty.$$

□

4.3.3. Criteria and overall estimation framework description

4.3.3.1. Criteria description

Estimating $\mu_{\max}$ is important, but when to estimate $\mu_{\max}$, such that a reliable tire-road friction coefficient can be obtained? To the author's best knowledge, based on the sensor configurations of mass produced vehicles, no reliable criteria of excitation detection to trigger the update of $\mu_{\max}$ estimation result are given. As is known, under

different $\mu_{\max}$ the corresponding lateral acceleration as threshold to indicate the tires coming into the nonlinear region is different, for instance, on high friction road condition, lateral acceleration smaller than 4 $\mathrm{m/s^2}$ is an indication that the tires still work in the linear region [86] while this value can be much smaller under low friction road conditions. Grip uses yaw rate and derivative of lateral velocity to check the excitation of vehicle lateral dynamics [39]. Similar methods are implemented to detect vehicle excitation [35, 44]. However, these criteria cannot be well adapted due to the lack of $\mu_{\max}$ information. Besides, in order to avoid mis-operation of ESC, the strategy about when to estimate $\mu_{\max}$ is conservative, which means some situations suitable for $\mu_{\max}$ estimation are ignored since there are no excitation criteria uniformly to $\mu_{\max}$. Hence, the criteria should be robust to $\mu_{\max}$ variations and meanwhile not conservative to the utilization of excitation, such that the $\mu_{\max}$ can be estimated more reliably.

The criteria in this study consist of two parts. The first and also the most important one is to compare the estimated $|x_f|$ with a defined constant threshold $x_{f,c}$ shown in Fig. 4.1 (shown as x_c) which is applicable for all tire-road friction conditions and thus can be used to detect excitation effectively. Moreover, this threshold is the boundary between the quasi-linear region and the nonlinear region of the front axle self-aligning torque, therefore, the decision of when to estimate road friction is not conservative due to sufficient usage of the tire non-linearity. The second part is an auxiliary criterion to alleviate the misuse of the first criterion. When vehicle lateral dynamic excitation is too small, the tire characteristics remain exactly in the linear region, which leads to a singular estimation of x_f. As a result, the estimated x_f may be much larger than the real value and thus leads to misuse of the criterion one. Therefore, extra criteria is introduced to alleviate its misoperation. To be more specific, the activation of criterion one is based on the precondition that the estimated total aligning torque, the measured lateral acceleration and the estimated front axle tire lateral force are simultaneously larger than their corresponding defined thresholds, which increases the reliability of $\mu_{\max}$ estimation. These criteria are shown more detailed with mathematical description as follows:

if $|\hat{x}_f| > x_{f,c}$ & $|\tau_{zf}| > \tau_{\text{thres}}$ & $|a_y| > a_{y,\text{thres}}$ & $|\hat{F}_{yf,ave}| > F_{yf,\text{thres}}$
$\hat{\mu}_{\max} = \mu_{max,\text{update}}$;
else
$\hat{\mu}_{\max} = \mu_{max,pre}$;
end

where τ_{thres}, $F_{yf,\text{thres}}$ as well as $a_{y,\text{thres}}$ are thresholds to avoid updating $\mu_{\max}$ when the

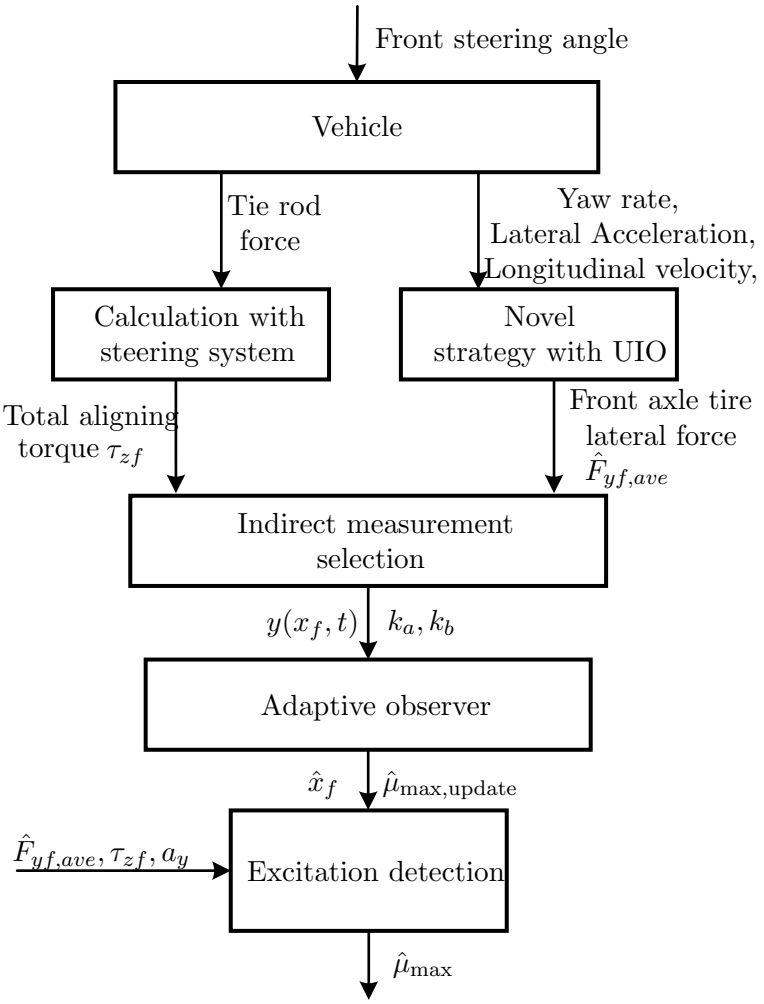

Figure 4.7.: Overall estimation framework, which is further referred to as AVE.

excitation is too small, $\hat{\mu}_{\max}$ is the final estimated tire-road friction coefficient, $\mu_{max,\text{update}}$ is the estimation result of tire-road friction coefficient from the observer, $\mu_{max,pre}$ is the value of $\hat{\mu}_{\max}$ in previous step. It has to be mentioned that τ_{thres} and $F_{yf,\text{thres}}$ here are the same values for avoiding singularity in the indirect measurement $y(x_f, t)$.

4.3.3.2. Overall estimation framework (AVE)

For a better understanding of the whole description in this thesis, the overall estimation framework is presented in Fig. 4.7. All parts of this estimation framework are further referred to as AVE. The measurements (yaw rate, lateral acceleration as well as longitu-

dinal velocity, etc.) are firstly utilized to estimate the front axle tire lateral force with a novel strategy based on UIO. Meanwhile, the front axle total aligning torque is estimated on the basis of measured tie rod force. Then, considering the front axle tire lateral force and the total aligning torque as input, an indirect measurement $y(x_f, t)$ based on the selection criteria is generated. Combined with this indirect measurement, a nonlinear adaptive observer is designed to estimate the tire-road friction coefficient. To increase the reliability of the estimation result, an excitation detection block is proposed with the proposed criteria to better update the estimated tire-road friction coefficient. The simulation and experimental results from method I are described in section 4.5 together with those from method II.

4.4. Method II: nonlinear adaptive observer for tire-road friction coefficient estimation

4.4.1. Transformed vehicle model

The transformed single track model (4.6) can be expressed as

$$\begin{aligned} \dot{\omega} &= q_1(t) + q_2(t)v_1(x_f) \\ \dot{x}_f &= q_3(t, x_f) + q_4(t)v_2(\mu_{\max}) \end{aligned} \tag{4.30}$$

where $q_1(t) = \frac{l\tau_{zf} m_v \cos(\delta) - l_r m a_y}{I_z}$, $q_2(t) = \frac{-|\tau_{zf}| l \cos(\delta)}{I_z}$, $v_1(x_f) = (\frac{f_f(x_f)}{g_f(x_f)+f_f(x_f)d_c} - m_v)\text{sign}(x_f)$ which is a monotonic increasing odd function (between $-x_s$ and x_s) w.r.t. x_f and already shown in Fig.4.6 in section 4.3.2.1[4], $q_3(t, x_f) = (a-b)(cos\delta)f_f(x_f)$, $q_4(t) = (bma_y - \omega - \dot{\delta})$, $v_2(\mu_{\max}) = \frac{1}{\mu_{\max}}$. In the following, a nonlinear adaptive observer will be proposed for a more generalized low-triangular system and then be applied to the $\mu_{\max}$ estimation problem.

4.4.2. Nonlinear adaptive observer

Various approaches have been developed for adaptive observer design [22, 21, 55, 75, 110, 130, 40, 120, 41]. For affine-parametrized system, there is a considerable amount of literature. In [55], the Luenberger type observers, combined with different parameter adaptation laws such as gradient based and least squares methods, etc., are proposed

[4]The indirect measurement $y(x_f)$ in method I is actually the $v_1(x_f)$ in method II.

for linear time invariant systems. Zhang proposed an adaptive observer for linear time varying systems which require only uniform complete observability for the systems and persistent excitation for parameter estimation [130]. In [22], an adaptive observer is presented for nonlinear systems which need to be strict positive real (SPR) and satisfy some Lipschitz conditions. Stamnes designed a type of adaptive observer features that both unknown parameters and non-linearity of the unmeasured states can appear in the dynamics of the unmeasured states [110]. For non-affine parametrized systems, there is less work due to its complexity and difficulty. In [120] and [40], adaptation laws for monotonically parametrized perturbations are proposed with all states measurable. In [41], partial states are needed to be measured for estimation of non-affine parameters, however, this proposed method is based on some assumptions which are not all applicable for the system in this study.

Based on [40], in which an estimator for non-affine parametrized system was proposed with requirement of all states measurable, a nonlinear adaptive observer is proposed in this thesis. It recursively applies the idea from [40] on a non-affine parametrized lower triangular system, such that only partial states need to be measured for non-affine parameter estimation.

4.4.2.1. Nonlinear adaptive observer design

Considering the following class of system:

$$\begin{cases} \dot{w} &= f_1(t,w) + B_1(t,w)g_1(w,x) \\ \dot{x} &= f_2(t,x) + B_2(t,x)g_2(x,\theta) \\ \dot{\theta} &= 0 \\ y &= w, \end{cases} \tag{4.31}$$

where $x \in \Theta_1 \subset \mathbb{R}^n$ is a state vector, $\theta \in \Theta_2 \subset \mathbb{R}^r$ is a vector of unknown constant parameters, $w \in \Theta_3 \subset \mathbb{R}^n$ is a measured state vector, Θ_1, Θ_2, Θ_3 are all compact sets. The functions $f_1 : \mathbb{R}_{\geq 0} \times \mathbb{R}^n \to \mathbb{R}^n$, $B_1 : \mathbb{R}_{\geq 0} \times \mathbb{R}^n \to \mathbb{R}^{n \times m}$, $g_1 : \mathbb{R}^n \times \mathbb{R}^n \to \mathbb{R}^m$, $f_2 : \mathbb{R}_{\geq 0} \times \mathbb{R}^n \to \mathbb{R}^n$, $B_2 : \mathbb{R}_{\geq 0} \times \mathbb{R}^n \to \mathbb{R}^{n \times q}$, $g_2 : \mathbb{R}^n \times \mathbb{R}^r \to \mathbb{R}^q$. Besides, $g_1(w,x)$, $g_2(x,\theta)$ and $f_2(t,x)$ are locally Lipschitz in their arguments, respectively. $||B_1(t,w)||, ||B_2(t,x)||, ||\frac{\partial B_1(t,w)}{\partial t}||$, $||\frac{\partial B_2(t,x)}{\partial t}||$, $||\frac{\partial B_1(t,w)}{\partial w}||, ||\frac{\partial B_2(t,x)}{\partial x}||$ are bounded, respectively.

Remarks. *It is realistic to assume that x, θ, w all belong to some compact sets, since usually the parameters and state variables in real systems are bounded, especially for vehicle dynamics systems.*

The observer for the system is given by

$$\begin{aligned}
\dot{z}_1 &= -K_{\varphi_1}(f_1(t,w)+\hat{\varphi}_1) - B_1(t,w)\frac{\partial g_1(w,\hat{x})}{\partial \hat{x}}\big(u_\tau - f_2(t,\hat{x}) - B_2(t,\hat{x})g_2(\hat{x},\hat{\theta})\big)\\
\hat{\varphi}_1 &= z_1 + K_{\varphi_1}w + B_1(t,w)g_1(w,\hat{x})\\
\dot{\hat{x}} &= u_\tau(t,w,\hat{\varphi}_1,\hat{x},\hat{\theta})\\
\dot{z}_2 &= -K_{\varphi_2}(f_2(t,\hat{x})+\hat{\varphi}_2) - B_2(t,\hat{x})\frac{\partial g_2(\hat{x},\hat{\theta})}{\partial \hat{\theta}}u_\theta\\
\hat{\varphi}_2 &= z_2 + K_{\varphi_2}\hat{x} + B_2(t,\hat{x})g_2(\hat{x},\hat{\theta})\\
\dot{\hat{\theta}} &= u_\theta(t,\hat{x},\hat{\varphi}_2,\hat{\theta})
\end{aligned}$$

with

$$\begin{aligned}
u_\tau &= \mathrm{Proj}\Big(k_1\Gamma_1 M_1\big(\mathrm{sat}(\hat{\varphi}_1) - B_1(t,w)g_1(w,\hat{x})\big) + f_2(t,\hat{x}) + B_2(t,\hat{x})g_2(\hat{x},\hat{\theta})\Big)\\
u_\theta &= \mathrm{Proj}\Big(\Gamma_2 M_2\big(\mathrm{sat}(\hat{\varphi}_2) - B_2(t,\hat{x})g_2(\hat{x},\hat{\theta})\big)\Big)
\end{aligned}$$

where K_{φ_1}, K_{φ_2}, Γ_1 and Γ_2 are all symmetric positive definite matrices, respectively, $z_1 \subset \mathbb{R}^n$, $z_2 \subset \mathbb{R}^n$, k_1 is a positive scale. $\hat{\varphi}_1$ and $\hat{\varphi}_2$ are estimation for φ_1 and φ_2, respectively, where $\varphi_1 = B_1(t,w)g_1(w,x)$, $\varphi_2 = B_2(t,x)g_2(x,\theta)$. $\mathrm{sat}(\hat{\varphi}_1) = \hat{\varphi}_1$ if $||\hat{\varphi}_1|| \leq \Phi_1$, otherwise $\mathrm{sat}(\hat{\varphi}_1) = \frac{\hat{\varphi}_1}{||\hat{\varphi}_1||}\Phi_1$, where Φ_1 is a positive scale. This is also true for $\mathrm{sat}(\hat{\varphi}_2)$. Besides, $\mathrm{sat}(\hat{\varphi}_1) \in \Theta_4$, $\mathrm{sat}(\hat{\varphi}_2) \in \Theta_5$, where Θ_4 and Θ_5 are both compact sets, thus indicates $\hat{\varphi}_1 \in \mathbb{R}^n$, $\hat{\varphi}_2 \in \mathbb{R}^n$. The projection function is denoted as $\mathrm{Proj}(\cdot)$, refer to Appx. C.1. Due to the projection technique, it can be noted that, if $\hat{x}(t_0) \in \Theta_1$ and $\hat{\theta}(t_0) \in \Theta_2$, $\hat{x}(t)$ and $\hat{\theta}(t)$ remain in Θ_1 and Θ_2, respectively. $M_1(t,w) : \mathbb{R}_{\geq 0} \times \Theta_3 \to \mathbb{R}^{n\times n}$, $M_2(t,\hat{x},\hat{\theta}) : \mathbb{R}_{\geq 0} \times \Theta_1 \times \Theta_2 \to \mathbb{R}^{r\times n}$, where $||M_1(t,w)||$ and $||M_2(t,\hat{x},\hat{\theta})||$ are both bounded.

Remarks. *A more intuitive explanation for the proposed observer is given in the following: with measured w, $\dot{w} - f_1(t,w)$ can be used to express φ_1, then x is obtained by solving equation $\varphi_1 = B_1(t,w)g_1(w,x)$. After obtaining x, φ_2 is denoted by $\dot{x} - f_2(t,x)$. Finally θ is calculated with similar equation $\varphi_2 = B_2(t,x)g_2(x,\theta)$.*

4.4.2.2. Stability analysis

Introducing a new state $\bar{\varphi}_2 = z_2 + K_{\varphi_2}x + B_2(t,x)g_2(x,\hat{\theta})$, the error dynamics of the observer is then written as

$$\begin{aligned}\dot{\tilde{\varphi}}_1 &= \dot{\varphi}_1 - \dot{\hat{\varphi}}_1 \\ &= -K_{\varphi_1}\tilde{\varphi}_1 + d_1(t,w,\theta,\tilde{x}) + d_3(t,w,\hat{x},\tilde{\theta}),\end{aligned} \tag{4.32a}$$

$$\begin{aligned}\dot{\tilde{x}} &= \dot{x} - \dot{\hat{x}} \\ &= f_2(t,x) + B_2(t,x)g_2(x,\theta) - u_\tau(t,w,\hat{x},\varphi_1,\theta) \\ &\quad + d_4(t,w,\hat{x},\tilde{\varphi}_1,\theta) + d_5(t,w,\hat{x},\hat{\varphi}_1,\tilde{\theta}),\end{aligned} \tag{4.32b}$$

$$\begin{aligned}\dot{\tilde{\varphi}}_2 &= \dot{\varphi}_2 - \dot{\hat{\varphi}}_2 \\ &= -K_{\varphi_2}\tilde{\varphi}_2 + d_2(t,x,\tilde{\theta}) + d_6(t,\tilde{x},\hat{\varphi}_2,\hat{\theta}),\end{aligned} \tag{4.32c}$$

$$\begin{aligned}\dot{\tilde{\theta}} &= \dot{\theta} - \dot{\hat{\theta}} \\ &= -u_\theta(t,x,\varphi_2,\hat{\theta}) + d_7(t,x,\tilde{\varphi}_2,\hat{\theta}) + d_8(t,\tilde{x},\bar{\varphi}_2,\hat{x},\hat{\theta}).\end{aligned} \tag{4.32d}$$

The detailed deduction of the error dynamics and expressions for d_1 to d_8 can be found in Appx. C.2.

In the following, Fig.4.8 demonstrates the structure of the error dynamics for the observer. Denote the interconnected system $\Sigma^0_{\dot{\tilde{\theta}}}$ and $\Sigma^0_{\dot{\tilde{\varphi}}_2}$ as Σ_0 with $(\tilde{\theta},\tilde{\varphi}_2)$ as state variables, besides, $d_6(t,\tilde{x},\hat{\varphi}_2,\hat{\theta})$ and $d_8(t,\tilde{x},\bar{\varphi}_2,\hat{x},\hat{\theta})$ can be viewed as external inputs; The inter-connection of Σ_0 and $\Sigma^1_{\dot{\tilde{x}}}$ compose system Σ_1, which with $(\tilde{x},\tilde{\theta},\tilde{\varphi}_2)$ as state variables is subject to external input $d_4(t,w,\hat{x},\tilde{\varphi}_1,\theta)$; Finally, define Σ_2 as the inter-connection of Σ_1 and $\Sigma^2_{\dot{\tilde{\varphi}}_1}$ with $(\tilde{\varphi}_1,\tilde{x},\tilde{\theta},\tilde{\varphi}_2)$ as state variables. The target is to recursively stabilize the interconnected systems from the inner layer Σ_0 to outer layer Σ_2 by constructing strict Lyapunov functions. The following assumptions are put forward.

Assumption 4.4.1. *For all* $(t,w,\theta,\tilde{x}) \in \mathbb{R}_{\geq 0}\times\Theta_3\times\Theta_2\times(\Theta_1-\Theta_1)$, $||d_1(t,w,\theta,\tilde{x})|| \leq l_1||\tilde{x}||$, *where* l_1 *is a positive constant,* $(\Theta_1-\Theta_1) := \{x-\hat{x}\in\mathbb{R}^n \mid x,\hat{x}\in\Theta_1\}$;

Assumption 4.4.2. *For all* $(t,x,\tilde{\theta}) \in \mathbb{R}_{\geq 0}\times\Theta_1\times(\Theta_2-\Theta_2)$, $||d_2(t,x,\tilde{\theta})|| \leq l_2||\tilde{\theta}||$, *where* l_2 *is positive constant,* $(\Theta_2-\Theta_2) := \left\{\theta-\hat{\theta}\in\mathbb{R}^r \mid \theta,\hat{\theta}\in\Theta_2\right\}$;

Assumption 4.4.3. *For all* $(t,\tilde{x},\hat{\varphi}_2,\hat{\theta}) \in \mathbb{R}_{\geq 0}\times(\Theta_1-\Theta_1)\times\mathbb{R}^n\times\Theta_2$, $||d_6(t,\tilde{x},\hat{\varphi}_2,\hat{\theta})|| \leq l_6(K_{\varphi_2},\Gamma_2)||\tilde{x}||$, *where* $l_6(K_{\varphi_2},\Gamma_2)$ *is a positive variable determined by* K_{φ_2} *and* Γ_2.

Assumption 4.4.4. *For all* $(t,\tilde{x},\bar{\varphi}_2,\hat{x},\hat{\theta}) \in \mathbb{R}_{\geq 0}\times(\Theta_1-\Theta_1)\times\mathbb{R}^n\times\Theta_1\times\Theta_2$, $||d_8(t,\tilde{x},\bar{\varphi}_2,\hat{x},\hat{\theta})|| \leq l_8(K_{\varphi_2},\Gamma_2)||\tilde{x}||$, *where* l_8 *is a positive variable and determined by* K_{φ_2} *and* Γ_2.

Assumption 4.4.5. *Suppose that there exists a piecewise continuous function* $p_1(t,w) : \mathbb{R}_{\geq 0}\times\Theta_3 \to \mathbb{R}_{>0}$ *with* $p_1(t,w) > p_1^*$, *where* p_1^* *is a positive constant, and a function*

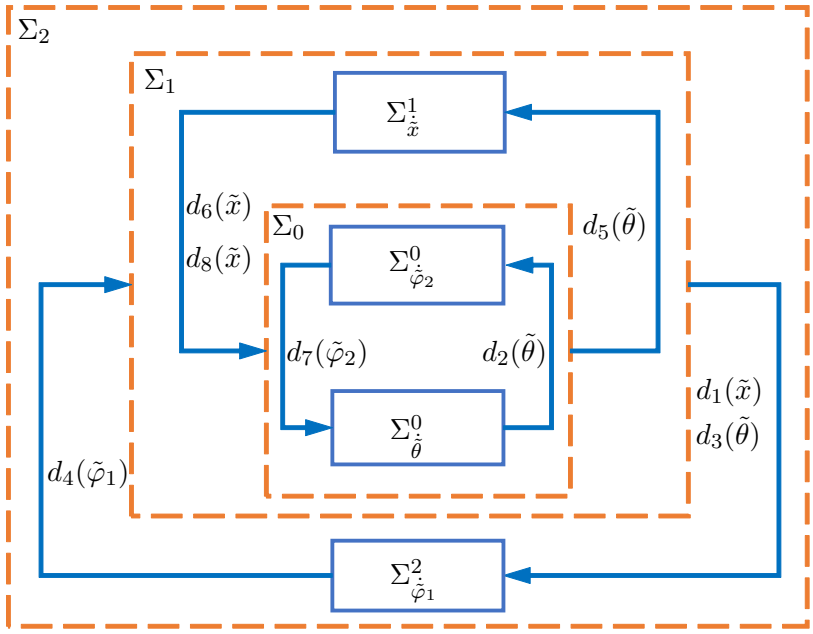

Figure 4.8.: Structure of error dynamics for the observer.

$M_1(t,w) : \mathbb{R}_{\geq 0} \times \Theta_3 \to \mathbb{R}^{n\times n}$, such that for all $t \in \mathbb{R}_{\geq 0}$, $w \in \Theta_3$ and $x \in \Theta_1$ as well as arbitrarily large $k_1 > 0$,

$$\begin{aligned} & M_1(t,w)B_1(t,w)\frac{\partial g_1(w,x)}{\partial x} + \frac{\partial g_1^T(w,x)}{\partial x}B_1^T(t,w)M_1^T(t,w) \\ & -\frac{1}{k_1}\Gamma_1^{-1}\frac{\partial(f_2(t,x)+B_2(t,x)g_2(x,\theta))}{\partial x} - \frac{1}{k_1}\frac{\partial(f_2(t,x)+B_2(t,x)g_2(x,\theta))^T}{\partial x}\Gamma_1^{-1} \\ \geq \; & 2p_1(t,w)I \end{aligned} \tag{4.33}$$

Assumption 4.4.6. *Suppose that there exists a piecewise continuous function $P_2(t,x) : \mathbb{R}_{\geq 0}\times\Theta_1 \to \mathbb{S}_{r+}$, where $\mathbb{S}_{r+}$ is the cone of $r\times r$ symmetric positive-semidefinite matrices[5], and a function $M_2(t,x,\theta) : \mathbb{R}_{\geq 0} \times \Theta_1 \times \Theta_2 \to \mathbb{R}^{r\times n}$, such that for all $t \in \mathbb{R}_{\geq 0}$, $x \in \Theta_1$ and for all pairs of $\theta_1, \theta_2 \in \Theta_2$*

$$M_2(t,x,\theta_1)B_2(t,x)\frac{\partial g_2(x,\theta_2)}{\partial\theta} + \frac{\partial g_2^T(x,\theta_2)}{\partial\theta}B_2^T(t,x)M_2^T(t,x,\theta_1) \;\geq\; 2P_2(t,x), \tag{4.34}$$

[5]The set of all symmetric positive-semidefinite matrices of particular dimension is called the positive semidefinite cone.

Suppose furthermore that there exist scales $T_2 > 0$, $\epsilon_2 > 0$, such that, for all $t \in R_{\geq 0}$,

$$\int_t^{t+T_2} P_2(\tau, x(\tau))d\tau \quad \geq \quad \epsilon_2 I, \tag{4.35}$$

and that for all $(t, \theta) \in R_{\geq 0} \times \Theta_2$,

$$||B_2(t,x)(g_2(x,\theta) - g_2(x,\hat{\theta}))|| \quad \leq \quad l_{g2}(\tilde{\theta}^T P_2(t,x)\tilde{\theta})^{\frac{1}{2}}, \tag{4.36}$$

for some $l_{g2} > 0$ [40].

Remarks. *Assumptions 4.4.1 - 4.4.4 are some Lipschitz type conditions, especially for Assumption 4.4.4 regarding $d_8(t, \tilde{x}, \bar{\varphi}_2, \hat{x}, \hat{\theta})$, in which term $u_\theta(t, \hat{x}, \bar{\varphi}_2, \hat{\theta}) - u_\theta(t, \hat{x}, \hat{\varphi}_2, \hat{\theta})$ is actually also related to $\tilde{x}$; Assumption 4.4.5 is the monotonic condition for estimation of x; Assumption 4.4.6 is the monotonic and persistent excitation condition for estimation of θ.*

There are also properties for d_3, d_4, d_5, d_7.

Property 4.4.1. *For all $(t, w, \hat{x}, \tilde{\theta}) \in \mathbb{R}_{\geq 0} \times \Theta_3 \times \Theta_1 \times (\Theta_2 - \Theta_2)$, $||d_3(t, w, \hat{x}, \tilde{\theta})|| \leq l_3||\tilde{\theta}||$, where l_3 is a positive constant;*

Property 4.4.2. *For all $(t, w, \hat{x}, \tilde{\varphi}_1, \theta) \in \mathbb{R}_{\geq 0} \times \Theta_3 \times \Theta_1 \times (\Theta_4 - \mathbb{R}^n) \times \Theta_2$, $||d_4(t, w, \hat{x}, \tilde{\varphi}_1, \theta)|| \leq l_4(\Gamma_1, k_1)||\tilde{\varphi}_1||$, where l_4 is a positive variable determined by Γ_1 and k_1, $(\Theta_4 - \mathbb{R}^n) := \{\varphi_1 - \hat{\varphi}_1 \in \mathbb{R}^n \mid \varphi_1 \in \Theta_4, \hat{\varphi}_1 \in \mathbb{R}^n\}$;*

Property 4.4.3. *For all $(t, w, \hat{x}, \hat{\varphi}_1, \tilde{\theta}) \in \mathbb{R}_{\geq 0} \times \Theta_3 \times \Theta_1 \times \mathbb{R}^n \times (\Theta_2 - \Theta_2)$, $||d_5(t, w, \hat{x}, \hat{\varphi}_1, \tilde{\theta})|| \leq l_5||\tilde{\theta}||$, where l_5 is a positive constant.*

Property 4.4.4. *For all $(t, x, \tilde{\varphi}_2, \hat{\theta}) \in \mathbb{R}_{\geq 0} \times \Theta_1 \times (\Theta_5 - \mathbb{R}^n) \times \Theta_2$, $||d_7(t, x, \tilde{\varphi}_2, \hat{\theta})|| \leq l_7(\Gamma_2)||\tilde{\varphi}_2||$, where l_7 is a positive variable determined by Γ_2, $(\Theta_5 - \mathbb{R}^n) := \{\varphi_2 - \bar{\varphi}_2 \in \mathbb{R}^n \mid \varphi_2 \in \Theta_5, \bar{\varphi}_2 \in \mathbb{R}^n\}$;*

Proof. For $d_3(t, w, \hat{x}, \tilde{\theta})$, since $||B_1(t, w)||$, $||\frac{\partial g_1(w,\hat{x})}{\partial \hat{x}}||$, $||B_2(t, \hat{x})||$ are all bounded, and $g_2(x, \theta)$ are local Lipschitz in their arguments, $||d_3(t, w, \hat{x}, \tilde{\theta})|| \leq l_3||\tilde{\theta}||$ is deduced.

For $d_4(t, w, \hat{x}, \tilde{\varphi}_1, \theta)$, according to Lipschitz continuity [40], with $(t, w, \hat{x}, \tilde{\varphi}_1, \theta) \in \mathbb{R}_{\geq 0} \times \Theta_3 \times \Theta_1 \times (\Theta_4 - \mathbb{R}^n) \times \Theta_2$, projection can be discarded. Therefore,

$$\begin{array}{rcl} ||d_4(t, w, \hat{x}, \tilde{\varphi}_1, \theta)|| & = & ||u_\tau(t, w, \hat{x}, \varphi_1, \theta) - u_\tau(t, w, \hat{x}, \hat{\varphi}_1, \theta)|| \\ \leq & l_4(\Gamma_1, k_1)||\varphi_1 - sat(\hat{\varphi}_1)|| & \leq \quad l_4(\Gamma_1, k_1)||\tilde{\varphi}_1|| \end{array} \tag{4.37}$$

The proof procedure from d_4 also holds for d_5, d_7. □

Besides, there are also two propositions.

Proposition 4.4.1. *Suppose assumption 4.4.5 holds, then the Lyapunov function*

$$V_x(t,\tilde{x}) \quad = \quad \frac{1}{2}\tilde{x}^T\Gamma_1^{-1}\tilde{x}, \tag{4.38}$$

and its derivation satisfies following inequations:

$$\dot{V}_x(t,\tilde{x}) \quad \leq \quad -\alpha_1||\tilde{x}||^2 + \beta_1(\tilde{\varphi}_1,\tilde{\theta})||\tilde{x}||, \tag{4.39}$$

where $\alpha_1 = k_1 p_1^*$, $\beta_1(\tilde{\varphi}_1,\tilde{\theta}) = ||\Gamma_1^{-1}||(l_4(\Gamma_1,k_1)||\tilde{\varphi}_1|| + l_5||\tilde{\theta}||)$. *Besides,*

$$\frac{1}{2}\lambda_{\min}(\Gamma_1^{-1})||\tilde{x}||^2 \quad \leq \quad V_x(t,\tilde{x}) \quad \leq \quad \frac{1}{2}\lambda_{\max}(\Gamma_1^{-1})||\tilde{x}||^2 \tag{4.40}$$

Proof. See Appx. C.3. □

Proposition 4.4.2. *Suppose Assumption 4.4.6 holds, then the Lyapunov function*

$$V_\theta(t,\tilde{\theta}) \quad = \quad \frac{1}{2}\tilde{\theta}^T(\Gamma_2^{-1} - \psi\int_t^\infty \exp(t-\tau)P_2(\tau,x(\tau))d\tau)\tilde{\theta}, \tag{4.41}$$

satisfies following inequations:

$$\dot{V}_\theta(t,\tilde{\theta}) \quad \leq \quad -\alpha_2(\Gamma_2)||\tilde{\theta}||^2 + \lambda_{\max}(\Gamma_2^{-1})||\tilde{\theta}||\big(l_7(\Gamma_2)||\tilde{\varphi}_2|| + l_8(K_{\varphi_2},\Gamma_2)||\tilde{x}||\big), \tag{4.42}$$

where α_2 *is a positive variable determined by* Γ_2. *Besides,*

$$\tfrac{1}{2}(\lambda_{\min}(\Gamma_2^{-1}) - \psi\lambda_2^*)||\tilde{\theta}||^2 \quad \leq \quad V_\theta(t,\tilde{\theta}) \quad \leq \quad \tfrac{1}{2}\lambda_{\max}(\Gamma_2^{-1})||\tilde{\theta}||^2, \tag{4.43}$$

where $\psi < \frac{\lambda_{\min}(\Gamma_2^{-1})}{\lambda_2^*}$, λ_2^* *is the upper boundary of* $\int_t^\infty \exp(t-\tau)P_2(\tau,x(\tau))d\tau$.

Proof. The reader can refer to the proposition 4 in [81]. □

Theorem 4.4.1. *Suppose that Assumptions 4.4.1 — 4.4.6 hold, then there exists a positive definite matrix* K_{φ_1}, *such that if* $\lambda_{\min}(K_{\varphi_1})$ *is large enough, then the error dynamics of (4.32a)-(4.32d) are uniformly exponentially stable for* $\left(\tilde{\varphi}_1,\tilde{x},\tilde{\varphi}_2,\tilde{\theta}\right) \in (\Theta_4 - \mathbb{R}^n) \times (\Theta_1 - \Theta_1) \times (\Theta_5 - \mathbb{R}^n) \times (\Theta_2 - \Theta_2)$.

Proof. First, set $X_2 = [\tilde{\varphi}_2^T, \tilde{\theta}^T]^T$ and choose $V_2(t,X_2) = V_\theta(t,\tilde{\theta}) + \frac{1}{2}\tilde{\varphi}_2^T\tilde{\varphi}_2$. By applying

Proposition 4.4.2,

$$\begin{aligned}
\dot{V}_2(t,X_2) &\leq -\alpha_2(\Gamma_2)||\tilde{\theta}||^2 + \lambda_{\max}(\Gamma_2^{-1})||\tilde{\theta}||\Big(l_7(\Gamma_2)||\tilde{\varphi}_2|| + l_8(K_{\varphi_2},\Gamma_2)||\tilde{x}||\Big) \\
&\quad -\tilde{\varphi}_2^T K_{\varphi_2}\tilde{\varphi}_2 + \tilde{\varphi}_2^T\Big(d_2(t,x,\tilde{\theta}) + d_6(t,\tilde{x},\hat{\varphi}_2,\hat{\theta})\Big) \\
&\leq -\alpha_2(\Gamma_2)||\tilde{\theta}||^2 - \lambda_{\min}(K_{\varphi_2})||\tilde{\varphi}_2||^2 + \Big(l_7(\Gamma_2)\lambda_{\max}(\Gamma_2^{-1}) + l_2\Big)||\tilde{\theta}||||\tilde{\varphi}_2|| \\
&\quad +\Big(l_8(K_{\varphi_2},\Gamma_2)\lambda_{\max}(\Gamma_2^{-1})||\tilde{\theta}|| + l_6(K_{\varphi_2},\Gamma_2)||\tilde{\varphi}_2||\Big)||\tilde{x}|| \\
&\leq -[||\tilde{\varphi}_2||,||\tilde{\theta}||]Q_2[||\tilde{\varphi}_2||,||\tilde{\theta}||]^T \\
&\quad +\Big(l_8(K_{\varphi_2},\Gamma_2)\lambda_{\max}(\Gamma_2^{-1}) + l_6(K_{\varphi_2},\Gamma_2)\Big)||X_2||||\tilde{x}||
\end{aligned}$$

is deduced, where

$$Q_2 = \begin{bmatrix} \lambda_{\min}(K_{\varphi_2}) & -\frac{l_7(\Gamma_2)\lambda_{\max}(\Gamma_2^{-1})+l_2}{2} \\ -\frac{l_7(\Gamma_2)\lambda_{\max}(\Gamma_2^{-1})+l_2}{2} & \alpha_2(\Gamma_2) \end{bmatrix}.$$

Then, as long as $\lambda_{\min}(K_{\varphi_2}) > \frac{(l_7(\Gamma_2)\lambda_{\max}(\Gamma_2^{-1})+l_2)^2}{4\alpha_2(\Gamma_2)}$, Q_2 is positive definite. It can be subsequently deduced that

$$\dot{V}_2(t,X_2) \leq -\lambda_{\min}(Q_2)||X_2||^2 + \Big(l_8(K_{\varphi_2},\Gamma_2)\lambda_{\max}(\Gamma_2^{-1}) + l_6(K_{\varphi_2},\Gamma_2)\Big)||X_2||||\tilde{x}||.$$

Then choose $V_f(t,\tilde{x},\tilde{\varphi}_1,X_2) = V_x(t,\tilde{x}) + \frac{1}{2}\tilde{\varphi}_1^T\tilde{\varphi}_1 + V_2(t,X_2)$. Implementing 4.4.1 and aforementioned Properties,

$$\begin{aligned}
\dot{V}_f &= \dot{V}_2(t,X_2) - k_1 p_1^*||\tilde{x}||^2 + \beta_1(\tilde{\varphi}_1,\tilde{\theta})||\tilde{x}|| \\
&\quad +\tilde{\varphi}_1^T\Big(-K_{\varphi_1}\tilde{\varphi}_1 + d_1(t,w,\theta,\tilde{x}) + d_3(t,w,\hat{x},\tilde{\theta})\Big) \\
&\leq -k_1 p_1^*||\tilde{x}||^2 - \lambda_{\min}(K_{\varphi_1})||\tilde{\varphi}_1||^2 - \lambda_{\min}(Q_2)||X_2||^2 \\
&\quad +\Big(l_1 + l_4(\Gamma_1,k_1)||\Gamma_1^{-1}||\Big)||\tilde{\varphi}_1||||\tilde{x}|| + l_3||\tilde{\varphi}_1||||X_2|| \\
&\quad +\Big(l_5||\Gamma_1^{-1}|| + l_6(K_{\varphi_2},\Gamma_2) + l_8(K_{\varphi_2},\Gamma_2)\lambda_{\max}(\Gamma_2^{-1})\Big)||X_2||||\tilde{x}|| \\
&= -[||\tilde{\varphi}_1||,||\tilde{x}||,||X_2||]Q[||\tilde{\varphi}_1||,||\tilde{x}||,||X_2||]^T
\end{aligned}$$

is deduced, with

$$Q = \begin{bmatrix} \lambda_{\min}(K_{\varphi_1}) & -\iota_1 & -\iota_2 \\ -\iota_1 & k_1 p_1^* & -\iota_3 \\ -\iota_2 & -\iota_3 & \lambda_{\min}(Q_2) \end{bmatrix},$$

where

$$\begin{aligned}\iota_1 &= \Big(l_1 + l_4(\Gamma_1, k_1)||\Gamma_1^{-1}||\Big)/2,\\ \iota_2 &= l_3/2,\\ \iota_3 &= \Big(l_5||\Gamma_1^{-1}|| + l_6(K_{\varphi_2}, \Gamma_2) + l_8(K_{\varphi_2}, \Gamma_2)\lambda_{\max}(\Gamma_2^{-1})\Big)/2.\end{aligned}$$

Choose a suitable $k_1 > \frac{\iota_3^2}{p_1^*\lambda_{\min}(Q_2)}$, then select an appropriate K_{φ_1} to ensure that $\lambda_{\min}(K_{\varphi_1})$ is sufficiently large, such that Q is positive definite. This is achievable, since only the first item in Q is related to K_{φ_1}. Then $\dot{V}_f(t,\xi) \leq -\lambda_{\min}(Q)||\xi||^2$ is obtained, where $\xi = [\tilde{\varphi}_1^T, \tilde{x}^T, \tilde{\varphi}_2^T, \tilde{\theta}^T]^T$. Since

$$\begin{cases}\varpi_1||\xi||^2 &\leq V_f(t,\xi) \leq \varpi_2||\xi||^2\\ \dot{V}_f(t,\xi) &\leq -\lambda_{\min}(Q)||\xi||^2,\end{cases} \tag{4.44}$$

where $\varpi_1 = \min\{\frac{1}{2}\lambda_{\min}(\Gamma_1^{-1}), \frac{1}{2}, \frac{1}{2}(\lambda_{\min}(\Gamma_2^{-1}) - \psi\lambda_2^*)\}$, $\varpi_2 = \max\{\frac{1}{2}\lambda_{\max}(\Gamma_1^{-1}), \frac{1}{2}, \frac{1}{2}\lambda_{\max}(\Gamma_2^{-1})\}$, applying theorem 4.10 in [66], the error dynamics of (4.32a)-(4.32d) are uniformly exponentially stable for $\Big(\tilde{\varphi}_1, \tilde{x}, \tilde{\varphi}_2, \tilde{\theta}\Big) \in (\Theta_4 - \mathbb{R}^n) \times (\Theta_1 - \Theta_1) \times (\Theta_5 - \mathbb{R}^n) \times (\Theta_2 - \Theta_2)$. □

4.4.3. Vehicle application

4.4.3.1. Verification of the assumptions

In this part, the nonlinear adaptive observer design procedure proposed in section 4.4.2.1 is applied to the tire-road friction coefficient estimation problem given in (4.6).

To set the system (4.30) in the same framework of the general structure (4.31), $w = \omega$, $x = x_f$, $\theta = \frac{1}{\mu_{\max}}$, $f_1(t,w) = q_1(t)$, $B_1(t,w) = q_2(t)$, $g_1(w,x) = v_1(x_f)$, $f_2(t,x) = q_3(t,x_f)$, $B_2(t,x) = q_4(t)$, $g_2(x,\theta) = v_2(\mu_{\max})$, $y = \omega$ are defined. Then whether the

assumptions are satisfied or not is checked. Firstly there are

$$\begin{aligned} d_1(t,\theta,\tilde{x}) &= B_1(t)\big(\frac{\partial g_1(x)}{\partial x}f_2(t,x) - \frac{\partial g_1(\hat{x})}{\partial \hat{x}}f_2(t,\hat{x})\big) + \frac{\partial B_1(t)}{\partial t}\big(g_1(x) - g_1(\hat{x})\big) \\ &\quad + B_1(t)\big(\frac{\partial g_1(x)}{\partial x}B_2(t)g_2(\theta) - \frac{\partial g_1(\hat{x})}{\partial \hat{x}}B_2(t)g_2(\theta)\big), \\ d_2(t,\tilde{\theta}) &= \frac{\partial B_2(t)}{\partial t}(g_2(\theta) - g_2(\hat{\theta})), \\ d_6(t,\tilde{x}) &= -K_{\varphi_2}\big(K_{\varphi_2}x - K_{\varphi_2}\hat{x} + f_2(t,x) - f_2(t,\hat{x})\big), \\ d_8(t,\tilde{x},\tilde{\theta}) &= \mathrm{Proj}\left(\Gamma_2 M_2(t,\hat{\theta})(\mathrm{sat}(\bar{\varphi}_2) - B_2(t)g_2(\hat{\theta}))\right) \\ &\quad - \mathrm{Proj}\left(\Gamma_2 M_2(t,\hat{\theta})(\mathrm{sat}(\hat{\varphi}_2) - B_2(t)g_2(\hat{\theta}))\right). \end{aligned}$$

With respect to $d_1(t,\theta,\tilde{x})$, there is

$$\begin{aligned} d_1(t,\theta,\tilde{x}) &= B_1(t)f_2(t,x)\big(\frac{\partial g_1(x)}{\partial x} - \frac{\partial g_1(\hat{x})}{\partial \hat{x}}\big) + B_1(t)\frac{\partial g_1(\hat{x})}{\partial \hat{x}}\big(f_2(t,x) - f_2(t,\hat{x})\big) \\ &\quad + \frac{\partial B_1(t)}{\partial t}\big(g_1(x) - g_1(\hat{x})\big) + B_1(t)B_2(t)g_2(\theta)\big(\frac{\partial g_1(x)}{\partial x} - \frac{\partial g_1(\hat{x})}{\partial \hat{x}}\big). \end{aligned}$$

In the $\mu_{\max}$ estimation problem, $g_1(\cdot)$ is C^2, and w, θ, x all belong to compact set, $||B_1(t)||$, $||B_2(t)||$, $||g_2(\theta)||$, $||f_2(t,x)||$ and $||\frac{\partial B_1(t)}{\partial t}||$ are bounded, $f_2(t,x)$ is locally Lipschitz w.r.t x and uniformly in t. Therefore, it can be deduced that

$$||d_1(t,\theta,\tilde{x})|| \leq l_1||\tilde{x}||,$$

where l_1 is positive constant, demonstrating that Assumption 4.4.1 holds. It can be easily derived that Assumption 4.4.2 and 4.4.3 are also satisfied.

As for $d_8(t,\tilde{x},\hat{\theta})$ in Assumption 4.4.4, it can be deduced that

$$\begin{aligned} ||d_8(t,\tilde{x},\hat{\theta})|| &\leq l(\Gamma_2)||(\mathrm{sat}(\bar{\varphi}_2) - \mathrm{sat}(\hat{\varphi}_2))|| \\ &\leq l(\Gamma_2)||K_{\varphi_2}x - K_{\varphi_2}\hat{x}|| \\ &\leq l_8(\Gamma_2, K_{\varphi_2})||\tilde{x}||, \end{aligned}$$

where $l_8(\Gamma_2, K_{\varphi_2})$ is a positive variable determined by Γ_2 and K_{φ_2}.

For Assumption 4.4.5, this does not hold. When the front axle total aligning torque τ_{zf} in $q_2(t)$ of (4.30) is zero, indicating $B_1(t) = 0$, there is no such a positive p_1^* smaller than $p_1(t,w)$ for a arbitrarily large k_1. A feasible solution will be described in 4.4.3.2.

For Assumption 4.4.6, $\frac{\partial g_2(\theta)}{\partial \theta} = \frac{\partial \theta}{\partial \theta} = 1$ and if $M_2(t)$ is defined as $\mathrm{sign}(B_2(t))$, the

condition (4.34) is reduced to $||B_2(t)|| \geq ||P_2(t)||$. This condition will be satisfied, since there always exists a $P_2(t)$, such that $||B_2(t)|| = ||P_2(t)||$, indicating $||B_2(t)|| \geq ||P_2(t)||$. With $||P_2(t)||$ being equal to $||B_2(t)||$, it is also easy to check that there exists a l_{g2} satisfying the condition (4.36). Furthermore, persistent excitation condition (4.35) is reasonable and necessary.

Therefore, except for Assumption 4.4.5, the remaining are all satisfied.

4.4.3.2. Modification of the nonlinear adaptive observer

4.4.3.2.1. When to activate the $\mu_{\max}$ estimation In 4.4.3.1, it can be noticed that Assumption 4.4.5 cannot be satisfied when τ_{zf} is zero, leading to unstable nonlinear adaptive observer and generation of inferior estimated $\mu_{\max}$. A feasible solution is to freeze $\mu_{\max}$ estimation when $|\tau_{zf}|$ is very small and activate it again when $|\tau_{zf}|$ becomes large. However, due to the poor quality of the τ_{zf} in the real application, auxiliary criteria is also introduced to reduce the mis-activation of $\mu_{\max}$ estimation: when $|\hat{x}_f|$ is less than a positive threshold $x_{f,a}$ or $|a_y|$ is less than a positive threshold $a_{y,\text{thres}}$, $\mu_{\max}$ estimation is frozen. During the freeze of $\mu_{\max}$ estimation, the update of x_f is open-loop. The criteria for activating $\mu_{\max}$ estimation are demonstrated in Table 4.2, where τ_{thres} is a threshold for front axle total aligning torque, θ is equal to $\frac{1}{\mu_{\max}}$.

Table 4.2.: Criteria for the activation of $\mu_{\max}$ estimation

$\|\hat{x}_f\| \geq x_{f,a}$ & $\|\tau_{zf}\| \geq \tau_{\text{thres}}$ & $\|a_y\| \geq a_{y,\text{thres}}$	$\|\hat{x}_f\| < x_{f,a}$ | $\|\tau_{zf}\| < \tau_{\text{thres}}$ | $\|a_y\| < a_{y,\text{thres}}$
$\dot{\hat{\theta}} = u_\theta(t, \hat{x}_f, \hat{\varphi}_2, \hat{\theta}),$ $\dot{\hat{x}}_f = u_\tau(t, w, \hat{\varphi}_1, \hat{x}_f, \hat{\theta}),$	$\dot{\hat{\theta}} = 0,$ $\dot{\hat{x}}_f = f_2(t, \hat{x}_f) + B_2(t, \hat{x}_f) g_2(\hat{x}_f, \hat{\theta}),$

4.4.3.2.2. When to output a reliable $\mu_{\max}$ estimation result From 4.4.3.2.1, it can be known that when the $\mu_{\max}$ estimation is activated, an updated $\mu_{\max}$ is obtained. However, whether this estimated result is reliable enough for application in some vehicle control system functions, more investigations should be conducted. From the tire characteristics in Fig.4.1, an intuition is given that the more nonlinearity the tire reaches, the richer the $\mu_{\max}$ information is contained. Therefore, if more tire characteristics information in the part of nonlinearity is utilized, more reliable $\mu_{\max}$ estimation result is obtained. This intuition is also analytically validated in Fig.4.9, where the larger the

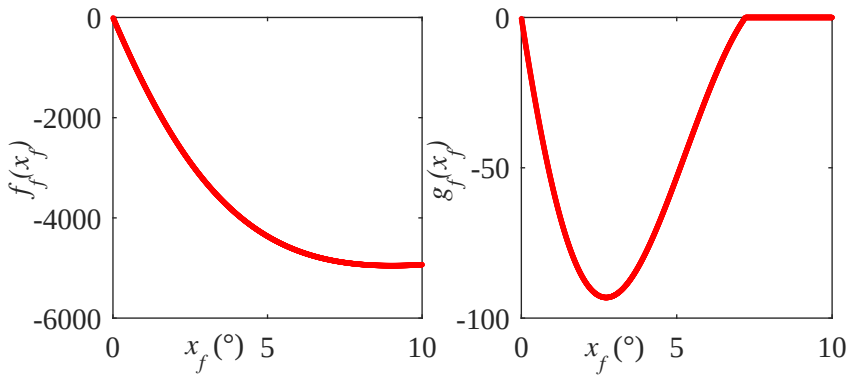

Figure 4.9.: Sensitivity analysis of F_{yf} and M_{zf} with respect to $\mu_{\max}$ under normal force 4000 N, where $F_{yf} = \mu_{\max} f_f(x_f)$ and $M_{zf} = \mu_{\max} g_f(x_f)$, $f_f(x_f) = \frac{\partial F_{yf}(x_f,\mu_{\max})}{\partial \mu_{\max}}$, $g_f(x_f) = \frac{\partial M_{zf}(x_f,\mu_{\max})}{\partial \mu_{\max}}$.

absolute value of x_f is, the more robust of $\mu_{\max}$ to the varying of F_{yf} while the absolute value of $\frac{\partial M_{zf}}{\partial \mu_{\max}}$ grows at first then falls down to zero. So, the value of x_f can be used to indicate the reliability of $\mu_{\max}$ estimation. Hence, another criterion is proposed to output the reliable $\mu_{\max}$ estimation result as follows:

$$\begin{cases} \mu_{\max,\text{es}} = \mu_{\max,\text{up}}; \ \textbf{if} \ |\hat{x}_f| \geq x_{f,c} \\ \mu_{\max,\text{es}} = \mu_{\max,\text{t-1}}; \ \textbf{if} \ |\hat{x}_f| < x_{f,c} \end{cases} \tag{4.46}$$

where $\mu_{\max,\text{es}}$ is the output of the $\mu_{\max}$ estimation for application in some vehicle control system functions, $\mu_{\max,\text{up}}$ the estimated $\mu_{\max}$ from the nonlinear adaptive observer, $\mu_{\max,\text{t-1}}$ the output of the $\mu_{\max}$ in the previous time step, $x_{f,c}$ is the corresponding threshold for the criterion.

For better understanding of the proposed criteria in both 4.4.3.2.1 and 4.4.3.2.2, Fig. 4.10 is illustrated to explain the whole structure in detail. The criteria proposed in 4.4.3.2.1 is realized in the "Tire-road friction estimation activation block" which is used to activate the tire-road friction estimation in the nonlinear adaptive observer. And the criterion proposed in 4.4.3.2.2 is corresponding to "Tire-road friction output decision block".

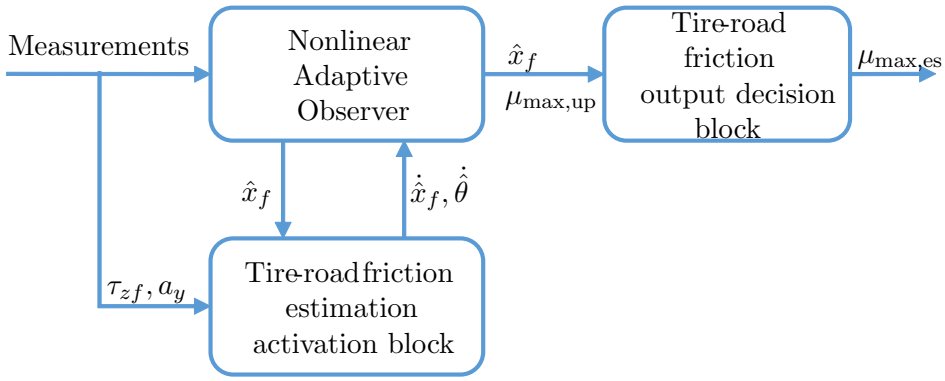

Figure 4.10.: Overall structure of the method II. "Tire-road friction estimation activation block" is used to decide when to activate the $\mu_{\max}$ estimation in the nonlinear adaptive observer, while "Tire-road friction output decision block" is used to judge if the estimated $\mu_{\max}$ from observer is reliable enough to output for application in vehicle control systems.

Table 4.3.: Basic information of AVE and NAO as well as EKF

	State equations	Measurements	States illustrated in figures
AVE	$\begin{cases} \dot{x}_f = c_1(t)f_f(x_f,t) + c_2(t)\theta \\ \dot{\theta} = 0 \end{cases}$	$ma_y, \tau_{zf} \rightarrow y(x_f,t)$	x_f, $\frac{1}{\theta}$
NAO	$\begin{cases} \dot{\omega} = q_1(t) + q_2(t)v_1(x_f) \\ \dot{x}_f = q_3(t,x_f) + q_4(t)v_2(\mu_{\max}) \\ \dot{\mu}_{\max} = 0 \end{cases}$	ω	x_f, $\mu_{\max}$
EKF	$\begin{cases} \dot{\alpha}_f = aF_{yf} + bF_{yr} - w - \dot{\delta} \\ \dot{\mu}_{\max} = 0 \end{cases}$	ma_y, τ_{zf}	$\frac{\alpha_f}{\mu_{\max}}$, $\mu_{\max}$

Table 4.4.: Gains and thresholds in the criteria for AVE in the simulations and experiments

	Simulation	Experiment
Gains	$k_a = 1$ $k_b(t) = \frac{k_c}{\max(\lvert c_2(t)\rvert, \epsilon)}$ where $k_c = 0.25$, $\epsilon = 0.02$	$k_a = 0.3$ $k_b(t) = \frac{k_c}{\max(\lvert c_2(t)\rvert, \epsilon)}$ where $k_c = 0.03$, $\epsilon = 0.25$
Thresholds in the criteria	$x_{f,c} = 0.01$ rad $\tau_{thres} = 35$ Nm $a_{y,thres} = 1$ m/s^2 $F_{yf,thres} = 900$ N	$x_{f,c} = 0.02$ rad $\tau_{thres} = 40$ Nm $a_{y,thres} = 1$ m/s^2 $F_{yf,thres} = 900$ N

Table 4.5.: Gains and thresholds in the criteria for NAO in the simulations and experiments

	Simulation	Experiment
Gains	$k_1 = 1$ $K_{\varphi_1} = 20$, $\Gamma_1 = 10$ $K_{\varphi_2} = 10$, $\Gamma_2 = 35$	$k_1 = 1$ $K_{\varphi_1} = 10$, $\Gamma_1 = 1$ $K_{\varphi_2} = 10$, $\Gamma_2 = 15$
Thresholds	$x_{f,a} = 0.001$ rad $\tau_{thres} = 35$ Nm $a_{y,thres} = 1$ m/s^2 $x_{f,c} = 0.01$ rad	$x_{f,a} = 0.005$ rad $\tau_{thres} = 40$ Nm $a_{y,thres} = 1$ m/s^2 $x_{f,c} = 0.02$ rad

Table 4.6.: Settings for EKF in simulations and experiments

	Simulation	Experiment
Covariance of the process noise	$Q = [0.00053, 0; 0, 0.3]$	$Q = [0.003, 0; 0, 0.3]$
Covariance of the observation noise	$R = [10000, 0; 0, 50]$	$R = [90000, 0; 0, 400]$
Condition for freezing $\mu_{\max}$ estimation	$\lvert a_y\rvert \leq 1$ m/s^2 or $\lvert \tau_{zf}\rvert \leq 35$ Nm	$\lvert a_y\rvert \leq 1$ m/s^2 or $\lvert \tau_{zf}\rvert \leq 40$ Nm

Table 4.7.: Statistical analysis of the estimated x_f from ave, nao and ekf in simulations and experiments: MVE means mean value of estimation error and RMS denotes root mean square of estimation error. Besides, Sinus., S. steer, DLC, Rand. denote sinusoidal steer, step steer, double lane change, random maneuver, respectively.

		MVE ($x_f(^\circ)$)			RMS ($x_f(^\circ)$)		
		ave	nao	ekf	ave	nao	ekf
Simulation	Sinus. (mixed $\mu_{\max}$)	0.005	0.007	-0.009	0.107	0.109	0.205
	S. steer (mixed $\mu_{\max}$)	0.027	0.003	-0.032	0.253	0.216	0.283
	DLC (mixed $\mu_{\max}$)	-0.024	-0.058	-0.073	0.132	0.163	0.266
	Rand. (mixed $\mu_{\max}$)	0.106	0.078	0.064	0.383	0.329	26.414
Experiment	Sinus. (high $\mu_{\max}$)	0.052	0.023	0.001	0.536	0.431	0.401
	S. steer (high $\mu_{\max}$)	0.226	0.256	0.065	0.516	0.541	0.380
	Rand. (low $\mu_{\max}$)	-0.146	-0.249	-1.249	1.701	1.205	33.348

Table 4.8.: Statistical analysis of the estimated $\mu_{\max}$ from ave, nao and ekf in simulations and experiments: MVE means mean value of estimation error and RMS denotes root mean square of estimation error. Besides, Sinus., S. steer, DLC, Rand. denote sinusoidal steer, step steer, double lane change, random maneuver, respectively.

		MVE ($\mu_{\max}$)			RMS ($\mu_{\max}$)		
		ave	nao	ekf	ave	nao	ekf
Simulation	Sinus. (mixed $\mu_{\max}$)	0.023	0.007	-0.020	0.132	0.130	0.160
	S. steer (mixed $\mu_{\max}$)	-0.024	-0.045	-0.059	0.208	0.216	0.233
	DLC (mixed $\mu_{\max}$)	0.014	-0.021	-0.052	0.265	0.263	0.274
	Rand. (mixed $\mu_{\max}$)	0.139	0.108	0.221	0.279	0.266	0.574
Experiment	Sinus. (high $\mu_{\max}$)	0.207	0.201	0.154	0.364	0.362	0.355
	S. steer (high $\mu_{\max}$)	0.198	0.196	0.124	0.396	0.408	0.389
	Rand. (low $\mu_{\max}$)	-0.155	-0.208	-0.198	0.388	0.395	0.418

4.5. Simulation and experiment results

4.5.1. Simulation results of the tire-road friction estimation

In this section, based on a nonlinear single track model including lateral load transfer, which is the same as the one used for the observer design, four different maneuvers — sinusoidal, step steer, double lane change as well as a random maneuver — are simulated to show tire-road friction coefficient estimation results among AVE, NAO and EKF. An EKF based on the work in [85][6] is chosen for comparison, because linearization based methods (like EKF) are widely used in $\mu_{\max}$ estimation with lateral dynamics [85, 52, 20]. For AVE, the estimated front axle lateral force results are additionally demonstrated. The basic information of the three methods is listed in Table 4.3. It can be noticed that though the state variables used for estimation are different among AVE, NAO and EKF, the states illustrated in the figures (both in simulations and experiments) are the same[7] for a better comparison. The settings of AVE, NAO and EKF for both simulations and experiments are listed in Table 4.4, Table 4.5 as well as Table 4.6, respectively.

The simulation results of four maneuvers are illustrated in Fig. 4.11, Fig. 4.12, Fig. 4.13 as well as Fig. 4.14, separately. Besides, Table 4.7 and Table 4.8 show the statistical analysis (mean value of estimation error (MVE) and root mean square of estimation error (RMS[8])) of x_f and $\mu_{\max}$ estimation results from AVE, NAO and EKF, respectively. As can be seen, in AVE, the front axle tire lateral force can be estimated well in all four maneuvers. Besides, by comparing F_{yf} estimation result under different frequency in sinusoidal maneuver (there is also a part of sinusoidal maneuver in random maneuver), it can be noticed that, the higher the frequency in the sinusoidal maneuver is, the less accuracy the estimation result is. In the step steer and double lane change maneuver, $\hat{F}_{yf,ave}$ is observed with small delay at first due to sudden change of front wheel steering angle and then converges to the real values. Regarding $\mu_{\max}$ estimation, results from AVE and NAO demonstrate better stability property compared to those from EKF. Meanwhile, NAO and AVE as well as EKF (under stable situation) show similar performance w.r.t. RMS. In sinusoidal and step steer maneuvers, $\mu_{\max}$ estimation results from AVE and

[6] In [85], the authors originally did not use a_y as measurement. For a fair comparison, a_y is introduced as an extra measurement in the application and the single track model is transformed into a form with α_f and $\mu_{\max}$ as state variables.

[7] $x_f = \frac{\alpha_f}{\mu_{\max}}, \frac{1}{\theta} = \mu_{\max}$

[8] It has to be mentioned that the RMS is calculated based on the whole time range of one maneuver. Hence, the RMS of $\mu_{\max}$ can be quite large if the road condition changes and the $\mu_{\max}$ estimator is not activated due to too less excitation. However, these situations occur for AVE, NAO and EKF and thus the comparison of RMS among these methods is still valuable.

NAO can converge slightly faster than those from EKF and afterwards show similar accuracy. W.r.t. RMS, these three methods only illustrate slight difference. It can be noticed that, in sinusoidal maneuver in Fig. 4.11 (around the 4th second), the $\mu_{\max,ave}$ and $\mu_{\max,nao}$ are not updated until some excitation level is reached, though during this time period the real $\mu_{\max}$ changes. This is contributed by the tire-road friction excitation detection block (AVE) and the tire-road friction output decision block (NAO), where the criteria are formulated (described in section 4.3.3.1 and section 4.4.3.2.2, respectively) for guaranteeing reliable $\mu_{\max}$ estimation. $\mu_{\max,ekf}$ is also frozen for short time around the 4th second due to the activation of condition for freezing $\mu_{\max}$. In the double lane change maneuver, from 0 s to 5 s under a low friction condition of 0.4, $\mu_{\max,ave}$ and $\mu_{\max,nao}$ are observed accurately and converge slightly faster than $\mu_{\max,ekf}$. From 5 s to 10 s, the $\mu_{\max}$ is changed to 0.7, and all $\mu_{\max,ave}$, $\mu_{\max,nao}$ as well as $\mu_{\max,ekf}$ do not react directly until the other half of double lane change is conducted. It can be noted that $\mu_{\max,nao}$ and $\mu_{\max,ekf}$ achieve similar performance and are both slightly better than $\mu_{\max,ave}$, this is because there is relative large estimation error in $F_{yf,ave}$, leading to inferior $\mu_{\max,ave}$. W.r.t. RMS, AVE(0.265), NAO(0.263) and EKF(0.274) demonstrate close results. In random maneuver, with a poor initial guess, $\mu_{\max,ekf}$ diverges during the whole time period while $\mu_{\max,ave}$, $\mu_{\max,nao}$ are always stable, demonstrating large attraction domain of AVE and NAO. The estimation of $\mu_{\max,ave}$ shows similar performance with $\mu_{\max,nao}$ from 0 s to 8 s, afterwords, $\mu_{\max,nao}$ performs slightly better than $\mu_{\max,ave}$ since $F_{yf,ave}$ estimation error becomes large.

In summary, w.r.t. simulations with no measurement noise under nominal system, both AVE and NAO can guarantee stability of $\mu_{\max}$ estimation in a wider range of vehicle operations than EKF. Besides, w.r.t. root mean square of estimation error (RMS) of $\mu_{\max}$, AVE and NAO shows similar performance with EKF (in stable situations).

4.5.2. Vehicle experiment results of the tire-road friction estimation

The vehicle experiments are conducted both in Nardò [5] (concrete test track) and Arjeplog [4] (grinded ice test track) with a racing car called Roding Roadster, see Fig. 4.15, with validated vehicle parameters available in Appx. A. The real values of front axle tire lateral force, $\mu_{\max}$ as well as x_f are obtained as follows: for the front axle tire lateral force, it is represented by $\frac{I_z\dot{\omega}+l_r m a_y}{l\cos\delta}$ which is deduced from a single track model. The actual friction coefficients are inferred from full brake[9] on the concrete test track

[9]The tire-road friction coefficient obtained from the vehicle longitudinal and lateral dynamics may be slightly different. But, in this thesis, it is assumed that they are the same.

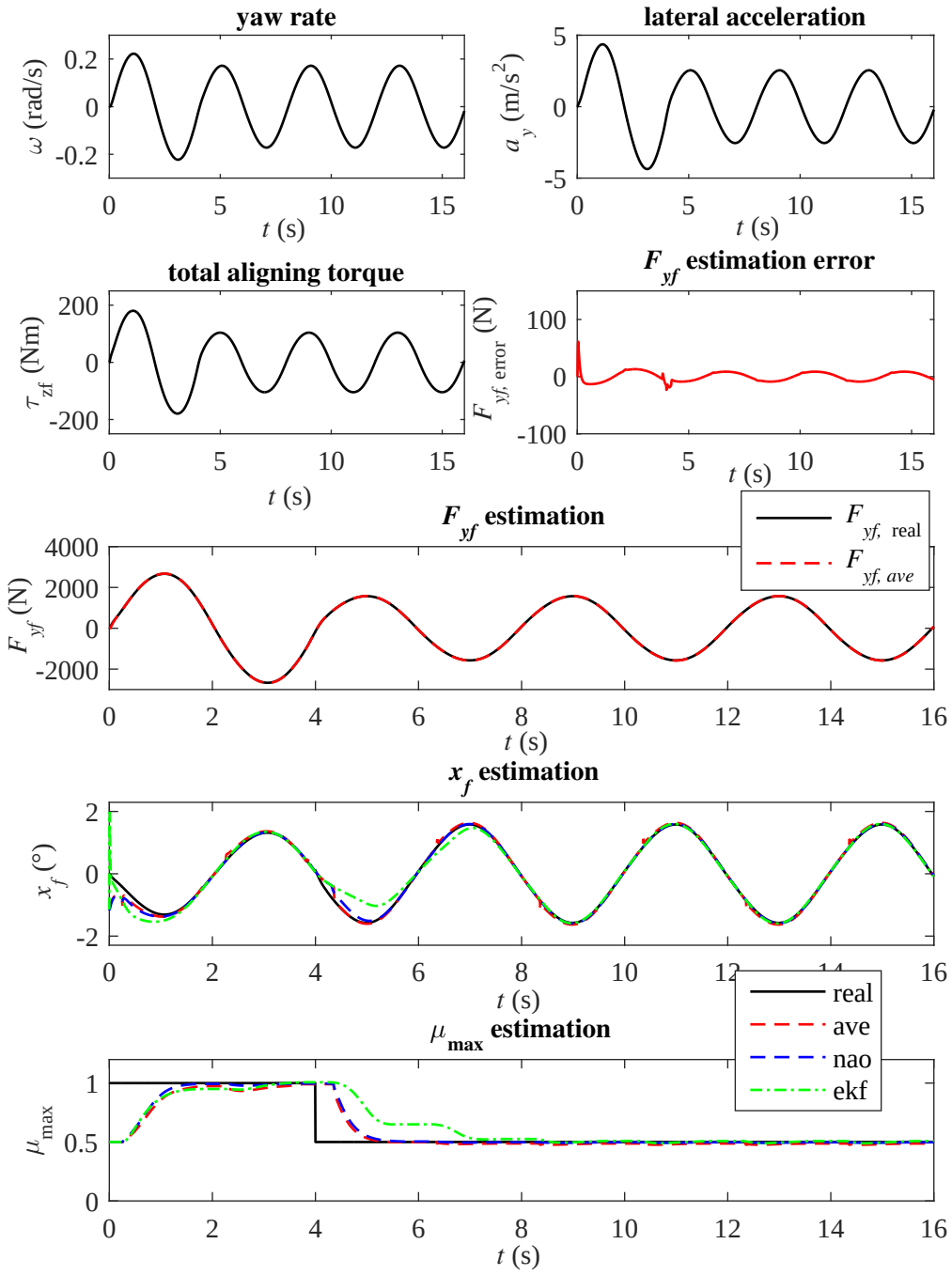

Figure 4.11.: Sinusoidal maneuver from high friction (v_x = 20 m/s) to low friction road condition (v_x = 15 m/s): wheel steering angle amplitude is 0.03 rad, frequency is 0.25 Hz.

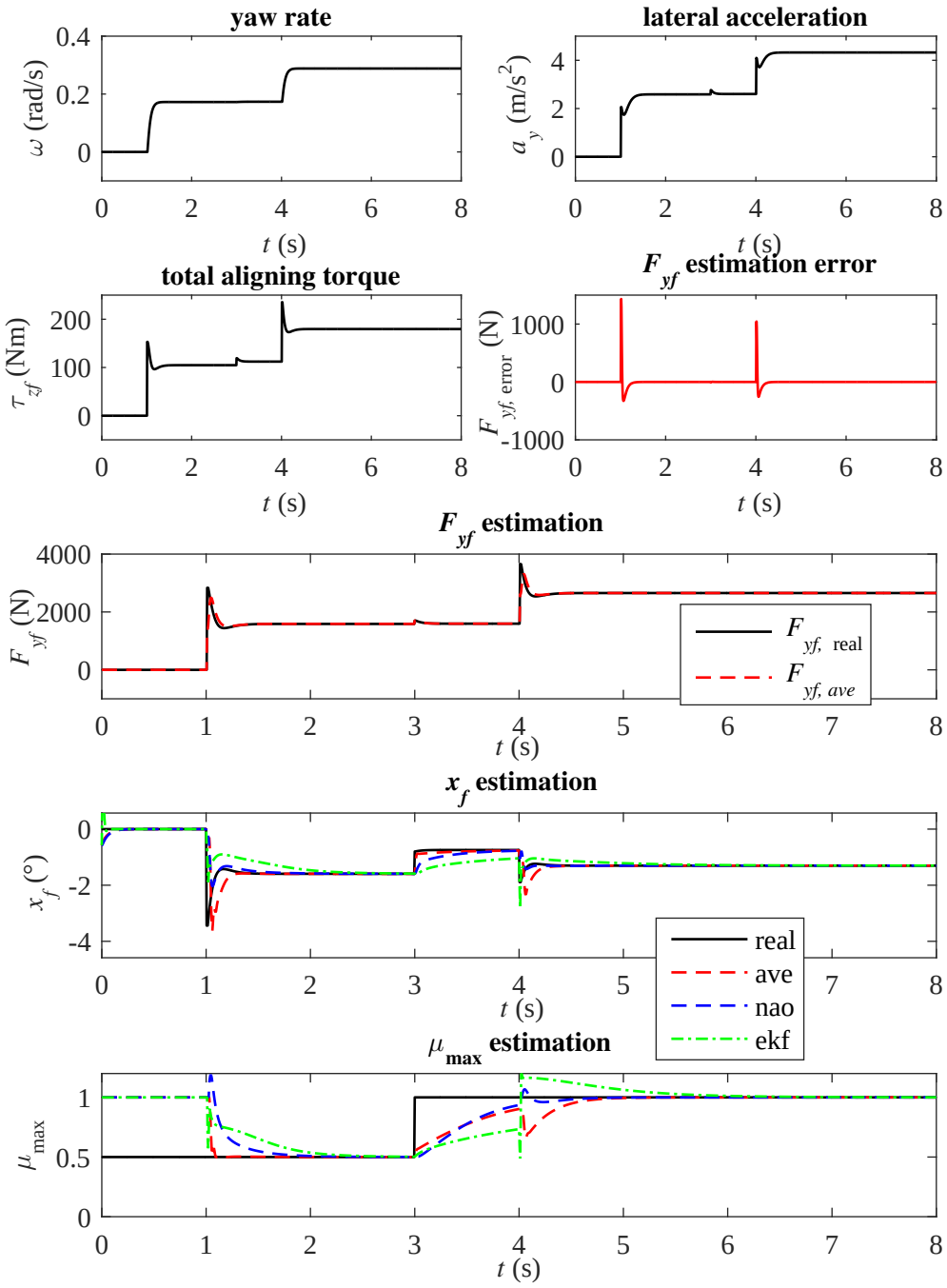

Figure 4.12.: Step steer maneuver from low friction to high friction road condition: $v_x = 15$ m/s. Under low friction road condition, the wheel steering angle jumps from 0 to 0.03 rad and then from 0.03 rad to 0.05 rad under high friction road condition.

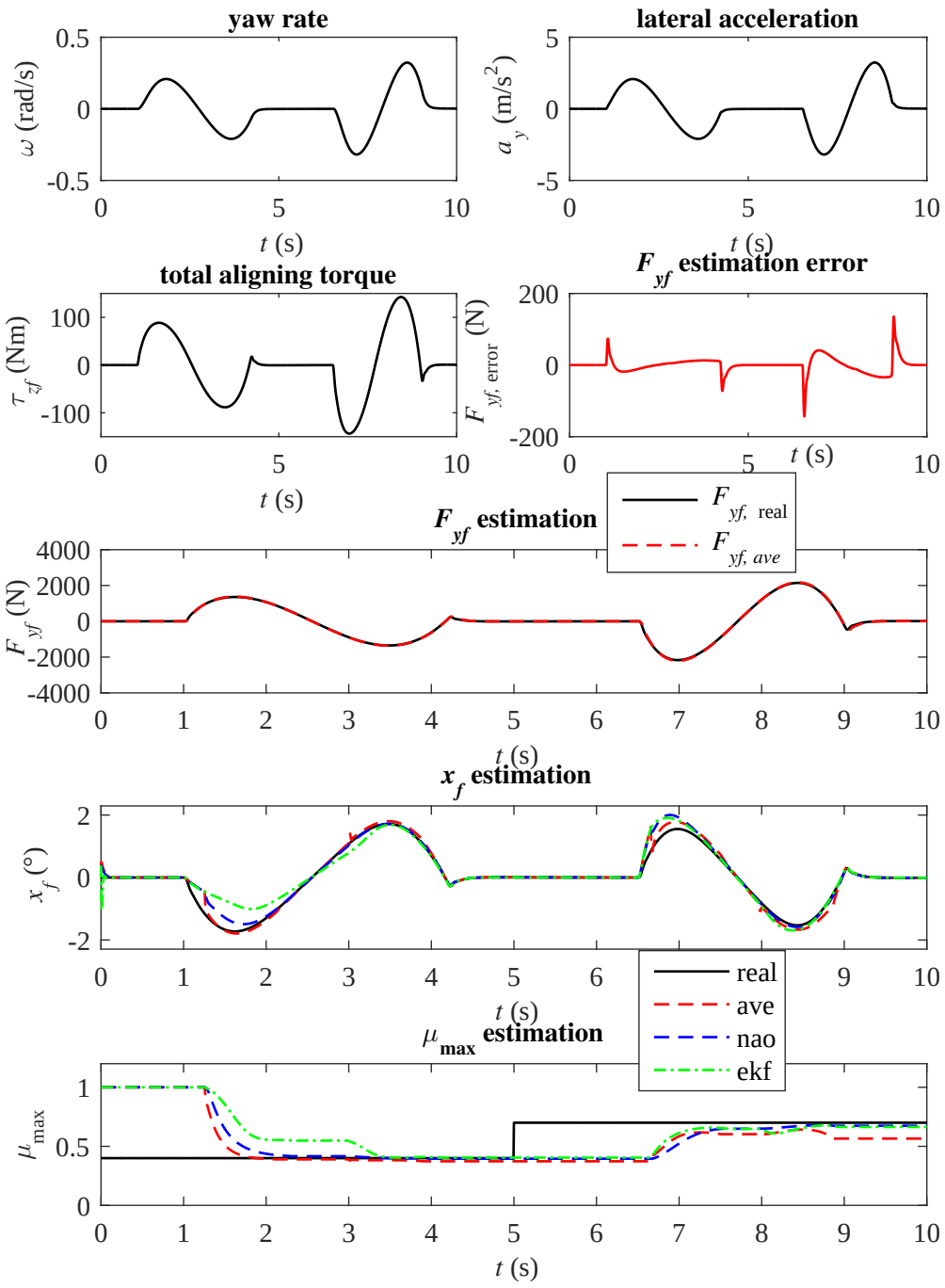

Figure 4.13.: Double lane change maneuver from low friction to medium friction road condition: $v_x = 10$ m/s.

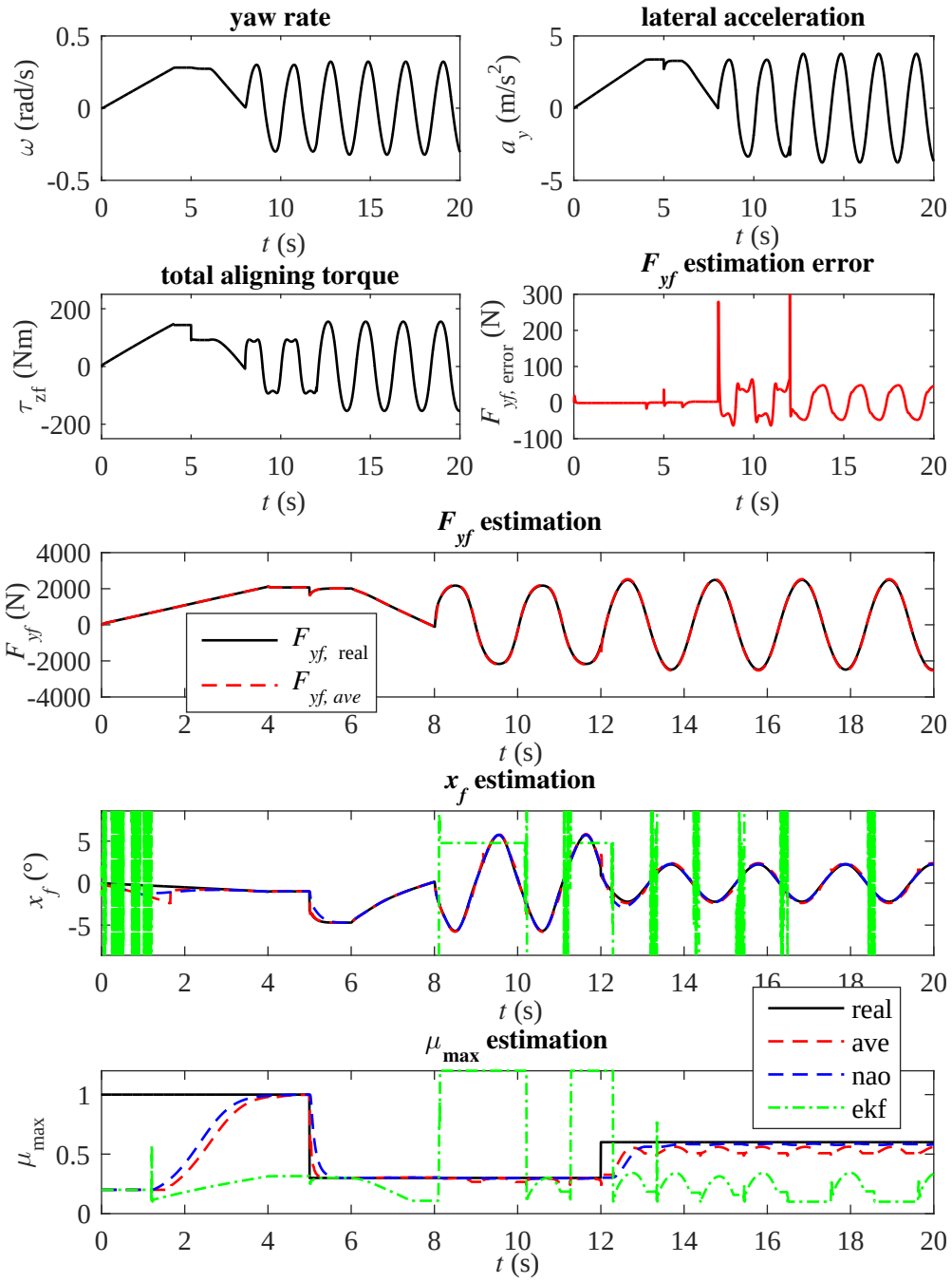

Figure 4.14.: Random maneuver from high friction to low friction, finally to medium road condition: $v_x = 12$ m/s.

Figure 4.15.: test racing car Roding Roadster. ©Foto: thyssenkrupp.

and lateral limit handling on the grinded ice test track, respectively. The actual lateral velocity is measured using a speed sensor [18] on concrete test track and is replaced by simulated lateral velocity based on a well parametrized nonlinear single track model[10] (considering lateral load transfer) on the grinded ice test track. Combining the inferred $\mu_{\max}$ with measured lateral velocity, x_f is obtained. The rest of the signals applied in the proposed method are obtained as follows: signals like lateral acceleration and yaw rate are directly measured; The wheel steering angle of front left and right is obtained based on measured steering wheel angle and a lookup table; The longitudinal velocity is measured by a speed sensor [18]. For the front axle total aligning torque, at first the tie rod forces are measured with strain gauge sensors, then the equation (3.18) is applied to calculate the total aligning torque. Furthermore, the settings for AVE, NAO as well as EKF for experiments can refer to Table 4.4, Table 4.5 and Table 4.6, respectively. It can be noticed that the gains for AVE and NAO are quite different in simulations and experiments, which are determined based on the balance between estimation convergence rate and sensitivity of estimation results to noise as well as uncertainties. Besides, the covariance of the process and observation noise in EKF for simulations and experiments are decided by considering noise level and model uncertainties.

On the concrete test track, Fig. 4.16 demonstrates a sinusoidal maneuver with a 0.2 Hz steering input and constant velocity 20 m/s. Fig. 4.17 shows step steer maneuver

[10] Due to sensor reasons the lateral velocity can not be well measured on the grinded ice test track, which is however not important, because attention is only paid to tire-road friction coefficient estimation in this study. Furthermore, tire parameters are already identified by a test truck in Switzerland (for parameters of F_y) and by vehicle tests in Nardò Italy (for parameters of M_z), separately. Therefore, the only function of the lateral velocity on the grinded ice test track is to become a reference value for comparing with estimated x_f.

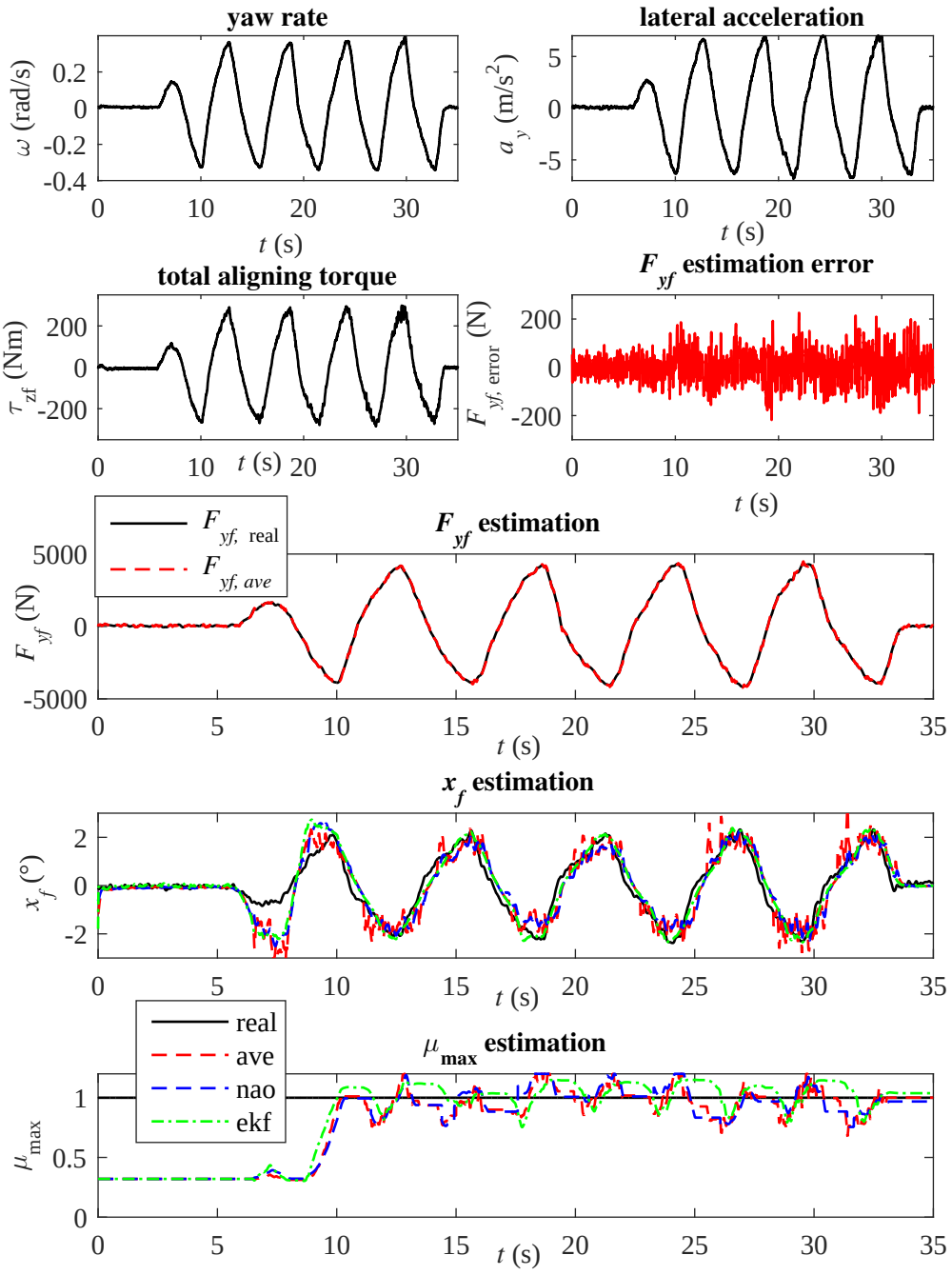

Figure 4.16.: Sinusoidal maneuver on high friction road condition: $v_x = 20$ m/s with frequency 0.2 Hz.

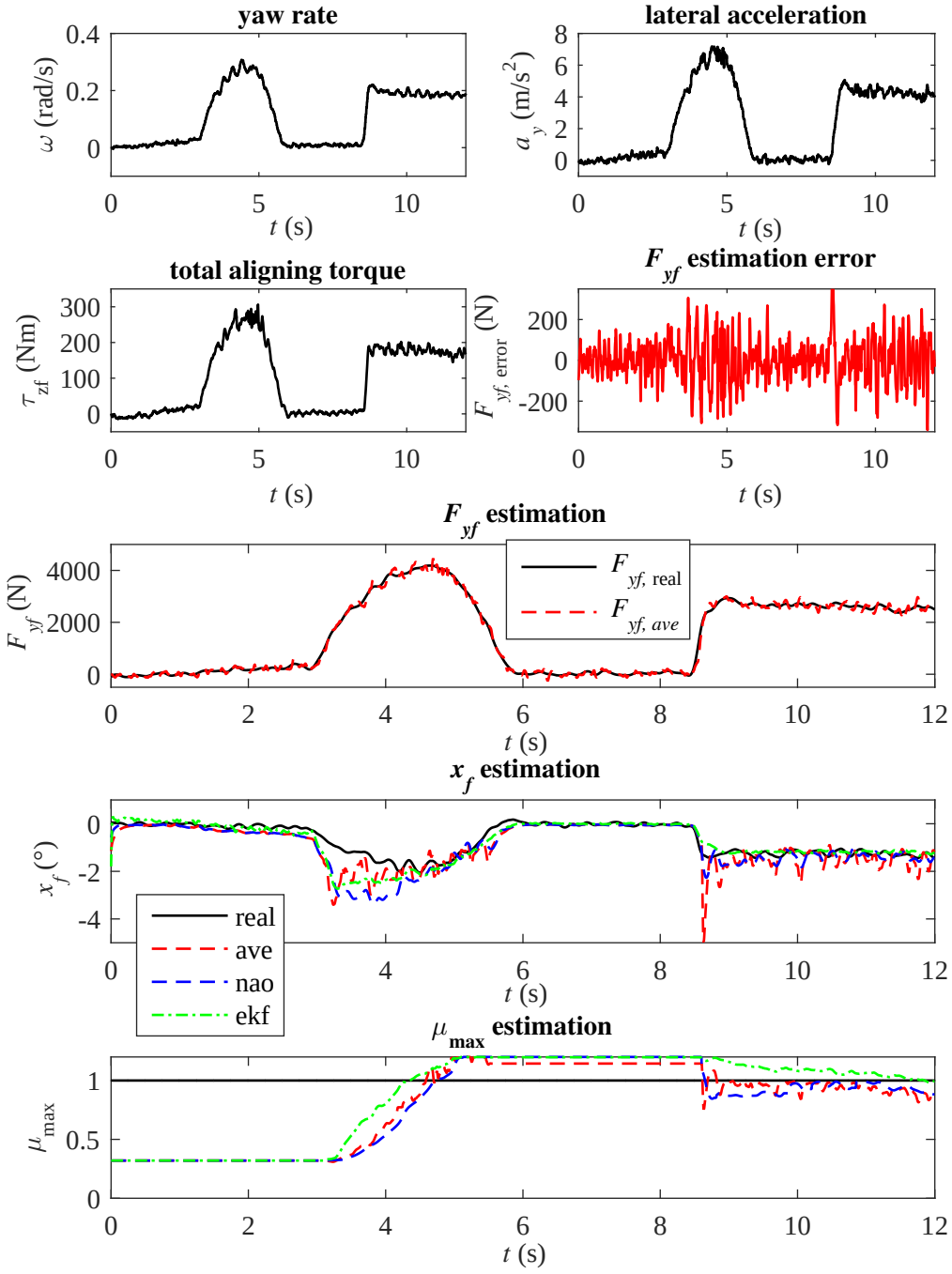

Figure 4.17.: Step steer maneuver on high friction road condition: $v_x = 25$ m/s.

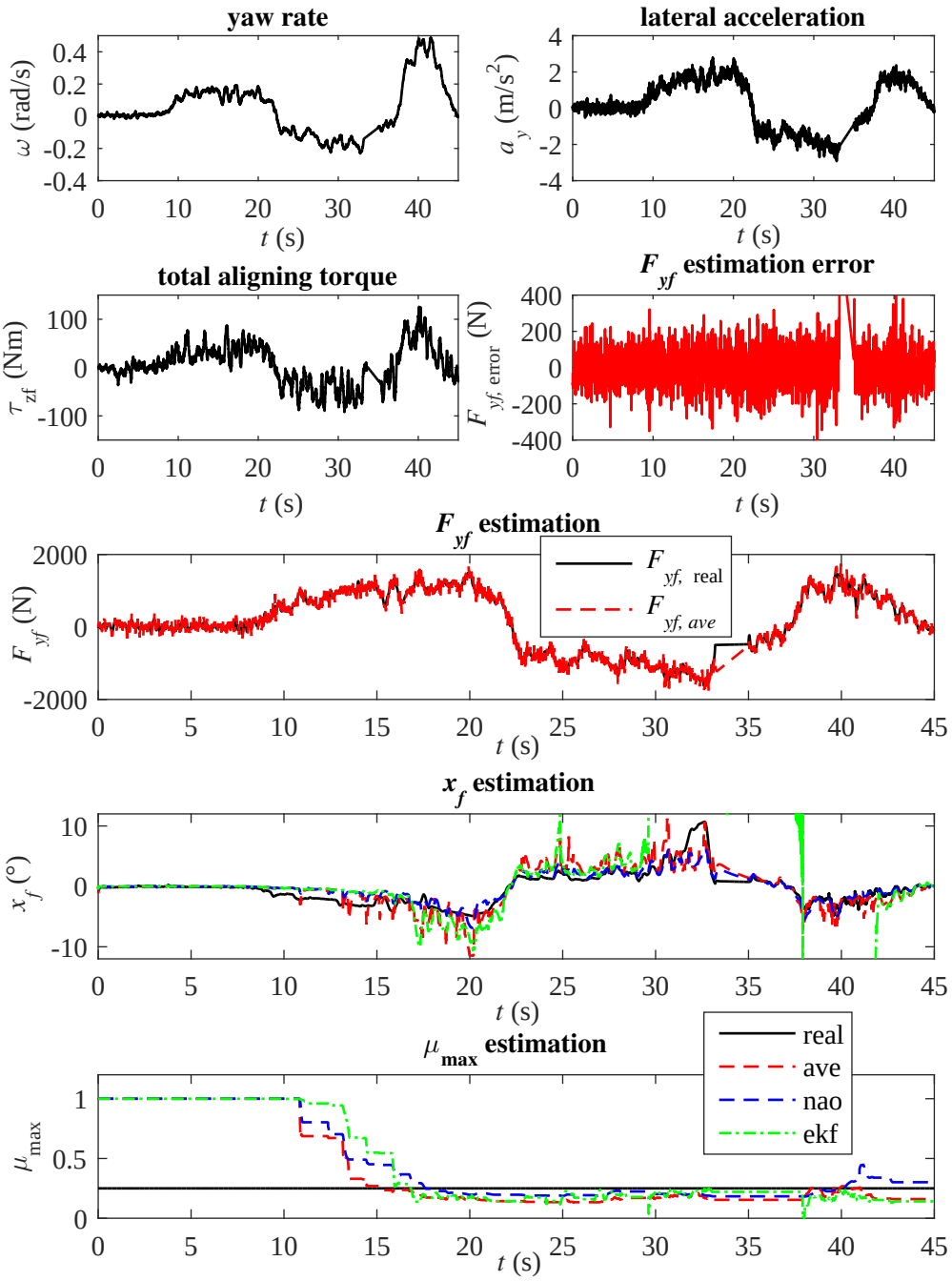

Figure 4.18.: Random steering maneuver on low friction road condition: v_x is slow varying around 12 m/s from 0 to 25 s, then changes to 7 m/s and stay around it.

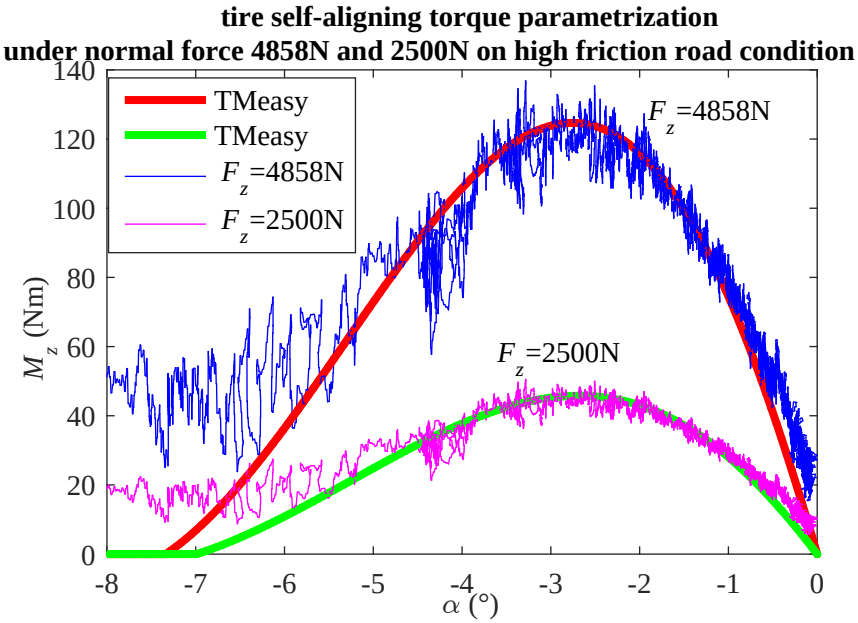

Figure 4.19.: Self-aligning torque parametrization for normal forces 4858 N and 2500 N on nominal tire-road condition $\mu_0 = 1$ with a constant radius (30 m) circular driving maneuver.

with a constant velocity of 25 m/s. Both maneuvers illustrate similar estimation results from AVE, NAO and EKF w.r.t. root mean square of estimation error (RMS) of x_f and $\mu_{\max}$ shown in Table 4.7 and Table 4.8, respectively. In Fig. 4.16, $\hat{F}_{yf,ave}$ is estimated accurately with low estimation error. And $\hat{x}_f$ is over-estimated by AVE, NAO and EKF at first, then converges to the real one, among which $x_{f,ave}$ is the noisiest. Besides, $\hat{\mu}_{\max}$ can be estimated accurately by AVE, NAO and EKF with similar convergent rate. In Fig. 4.17, the $\hat{F}_{yf,ave}$ estimation quality is not as good as that in sinusoidal maneuvers, especially around the 5th second, because the signal quality of yaw rate and lateral acceleration is worse than that in sinusoidal maneuver. The $\hat{x}_f$ increases faster than the real one from zero to around 3° for AVE, NAO and EKF between 0 s to 3 s, because the tire-road friction estimation results are frozen this time. For AVE, due to the indirect measurement $y(x_f, t)$ selection rule, gains k_a and k_b are set to zero, while for NAO and EKF, the conditions for freezing $\hat{\mu}_{\max}$ are still satisfied. Thus, $\hat{x}_f$ is estimated with underestimated $\hat{\mu}_{\max}$ in AVE, NAO and EKF. Afterwards, $x_{f,ave}$, $x_{f,nao}$ and $x_{f,ekf}$ converge to the real value. $\hat{\mu}_{\max}$ results from AVE, NAO and EKF are similar, but results from EKF can converge a little bit faster. The readers may feel confused why so

large excitation is needed to estimate the $\mu_{\max}$ on concrete test track, this is because racing car tires are utilized, with tire lateral force and self-aligning torque characteristics being linear until quite large tire slip angle, see Fig. 4.19. From this figure it can be noticed that the value of tire slip angle with respect to peak point of tire self-aligning torque is roughly $-2.8°$. However, in both of these experimental maneuvers, peak value of real x_f[11] does not reach $-2.8°$. So, such excitation is necessary for tire-road friction coefficient estimation on the concrete test track.

On the grinded ice test track, Fig. 4.18 shows a random steering maneuver, in which v_x is slow varying around 12 m/s from 0 to 25 s and then changes to 7 m/s and stays around it. Fig. 4.18 demonstrates that the estimation errors of $\hat{F}_{yf,ave}$ are small. Besides, $\hat{x}_f$ and $\hat{\mu}_{\max}$ demonstrate good stability property from AVE and NAO but not from EKF. More specifically, in Fig. 4.18, $\hat{x}_f$ from EKF diverges between 29 s and 38 s, so does the $\hat{\mu}_{\max}$ from EKF (around 29 s and 38 s separately). On the contrary, both $\hat{x}_f$ and $\hat{\mu}_{\max}$ from AVE and NAO are stable and show similar performance.

In summary, w.r.t. experiments, both AVE and NAO can guarantee stability of $\mu_{\max}$ estimation in a wider range of vehicle operations than EKF. Besides, $\mu_{\max}$ estimation results from AVE and NAO achieve similar accuracy with those from EKF (in stable situation) w.r.t. RMS.

4.6. Discussion

In this chapter, two methods (AVE and NAO) were proposed for estimating $\mu_{\max}$ based on tire self-aligning torque with vehicle lateral dynamics. In these methods, the origin of the observers' error dynamics are both asymptotically stable[12] for $(\tilde{x}_f, \tilde{\theta}) \in (\Theta_1 - \Theta_1) \times (\Theta_2 - \Theta_2)$ [13] with Θ_1 and Θ_2 being $\{x_f \in \mathbb{R} | -x_s \leq x_f \leq x_s\}$ and $\{\theta \in \mathbb{R} | 0.8 \leq \theta \leq 10\}$[14] separately, demonstrating that the two observers work in a wide range of vehicle operations. Besides, both AVE and NAO are able to run in real time. Furthermore, the sensors applied for observers design are from mass produced vehicles except for tie rod force sensors, which, however, are unnecessary if EPS or AFS available in mass produced vehicles are installed. Finally, by comparing the proposed two methods with EKF under

[11] On the concrete test track, since $\mu_{\max}$ is equal to 1, x_f is actually equivalent to the tire slip angle.

[12] In NAO, the origin of the error dynamics is exponentially stable, which is stronger than asymptotically stable, i.e. exponential stability implies asymptotic stability.

[13] In AVE, the equilibrium $(\tilde{x}_f, \tilde{\theta})$ is asymptotically stable for $(\tilde{x}_f, \tilde{\theta}) \in (\Theta_1 - \mathbb{R}) \times (\Theta_2 - \mathbb{R})$, indicating that $(\tilde{x}_f, \tilde{\theta}) \in (\Theta_1 - \Theta_1) \times (\Theta_2 - \Theta_2)$ is contained in this region of attraction.

[14] $\theta = \frac{1}{\mu_{\max}}$.

various simulations and experiments, it can be shown that 1) both AVE and NAO can guarantee stability of $\mu_{\max}$ estimation in a wider range of vehicle operations than EKF; 2) In terms of root mean square of $\mu_{\max}$ estimation error (RMS), the performance from AVE, NAO and EKF (in stable situation) is similar. Therefore, the criteria presented in the objective for tire-road friction estimation algorithms in this thesis are satisfied.

5. Tire-road friction coefficient estimation without tire self-aligning torque

This chapter describes a method to estimate $\mu_{\max}$ without utilizing the tire self-aligning torque information and this method is named as **method III**. It proposes an innovative scheme consisting of a non-convex optimization part and an integration part. The non-convex optimization is only utilized to estimate side slip angle and $\mu_{\max}$ as initial value for integration, thus, there is sufficient time left for finding the global optima through adaptive resolution based grid-search. During the search of the global optima, the integration was applied based on previously obtained initial value to calculate side slip angle and $\mu_{\max}$. This can be realized since the derivative of side slip angle is measurable and the derivative of $\mu_{\max}$ is assumed to be zero. Therefore, by interweaving discrete time solution of the optimization and continuous integration of derivatives from sensor data, the scheme allows for sufficient time for finding the global optima. Meanwhile, despite of the non-convex optimization, the observation scheme is able to run in real time. One advantage of the proposed observer is that, under no model uncertainty and measurement noise influence, the estimation error does not grow even when the system lacks observability. When observability requirement is satisfied, global asymptotic stability of the observer can also be guaranteed. The estimation results from the proposed observer and a linearization based observer[1] (lbo) are finally compared under various tire-road conditions with simulations and experiments. The results showed that **method III** performs overall better than lbo w.r.t. root mean square of estimation error (RMS) and can always guarantee stability in a wide range of vehicle operations while lbo cannot.

[1]Here, a linearization based observer (lbo) is utilized for comparison with the proposed observer. This is because lbo is widely implemented for simultaneously side-slip angle and tire-road friction estimation[37, 67, 68].

5.1. Vehicle and tire model

5.1.1. Vehicle model

With the side slip angle β and yaw rate ω as state variables, single track model (3.1) can be written as

$$\begin{aligned} \dot{\beta} &= \frac{a_y(\alpha_f, \alpha_r, \mu_{\max})}{v_x} - \omega, \\ \dot{\omega} &= \frac{l_f F_{yf}(\alpha_f, \mu_{\max})\cos\delta}{I_z} - \frac{l_r F_{yr}(\alpha_r, \mu_{\max})}{I_z}, \\ \dot{\mu}_{\max} &= 0, \end{aligned} \tag{5.1}$$

where

$$a_y = \frac{F_{yf}\cos\delta + F_{yr}}{m},\ \alpha_f = \beta + \frac{l_f\omega}{v_x} - \delta,\ \alpha_r = \beta - \frac{l_r\omega}{v_x}.$$

The system outputs that can be measured are collected as $y = [a_y\ \omega]^T$. Besides $[v_x\ \delta]^T$ are regarded as external measurable signals.

5.1.2. Tire model

A modified TMsimple for calculating the tire lateral force is utilized in this chapter, such that better solutions of the proposed algorithm in the applications can be obtained. The modified TMsimple is described as follows:

$$\begin{aligned} F_y &= -K\sin[B(1 - e^{\frac{-|\alpha|}{A}})\mathrm{sign}(\alpha)] \quad |\alpha| \le -A\ln(1 - \frac{\pi}{2B}), \\ F_y &= -K\mathrm{sign}(\alpha) \qquad\qquad\qquad\qquad\quad |\alpha| > -A\ln(1 - \frac{\pi}{2B}), \end{aligned} \tag{5.2}$$

with

$$\begin{aligned} K &= Y_{\max}(F_z, \mu_{\max}), \\ B &= \pi - \arcsin\frac{Y_\infty(F_z, \mu_{\max})}{Y_{\max}(F_z, \mu_{\max})} \qquad Y_\infty(F_z, \mu_{\max}) \le Y_{\max}(F_z, \mu_{\max}), \\ A &= \frac{KB}{dY_0(F_z)}, \end{aligned} \tag{5.3}$$

where $-A\ln(1 - \frac{\pi}{2B})$ is the absolute value of wheel slip angle corresponding to the peak point of lateral force. Descriptions of $Y_{\max}(F_z, \mu_{\max})$, $Y_\infty(F_z, \mu_{\max})$ as well as $dY_0(F_z)$

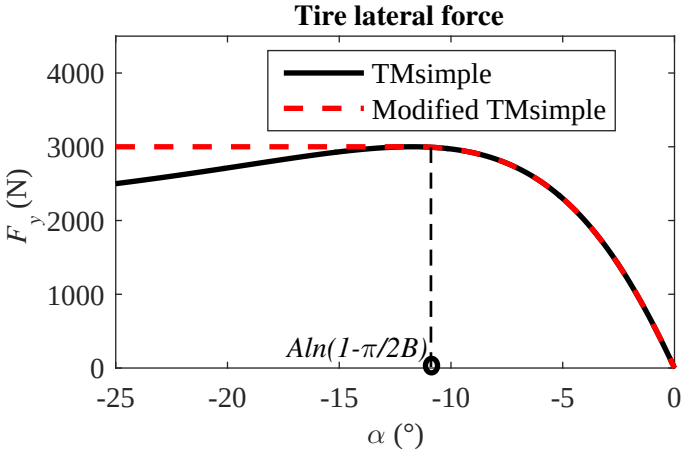

Figure 5.1.: Difference between modified TMsimple and its original version. The corresponding value of α w.r.t. the peak F_y is $A \ln(1 - \frac{\pi}{2B})$

can refer to (3.9). The difference between modified TMsimple and its original version is illustrated in Fig. 5.1

5.2. Method III: optimization based real time tire-road friction coefficient estimation

Various approaches have been developed for tire-road friction estimation. The state-of-the-art is presented in section 2.2, but how to design an observer which guarantees stability in wide range of vehicle operations is still an open question. Some researchers proposed utilizing optimization based observers, such as moving horizon estimation (MHE) [112, 128] or nonlinear recursive least squares (NRLS) [31, 9], to estimate tire-road friction coefficient. However, as the optimization process in these methods is non-convex, there is no guarantee to find the global minimum without an accurate initial guess. Consequently, the observation error can be excessively large in some situations. Global optimization algorithms like differential evolution [111] (DE), particle swarm optimization [63] (PSO) are usually able to obtain the optimum solution of non-convex optimization independent of initial guess, but the inferior real time capability of these methods is a great barrier for their application on the tire-road friction estimation.

Hence, in this research, an innovative optimization based framework to simultaneously estimate tire-road friction coefficient and side slip angle is proposed. The observation

problem is formulated as a non-convex optimization. A novelty of the framework is that the side slip angle and tire-road friction coefficient can be real time accurately estimated without a good initial guess for the non-convex optimization. A key observation is that the time derivative of side slip angle can be computed based on measurement and the time derivative of $\mu_{\max}$ is assumed to be zero. This allows the observed variables to be updated at a relatively low frequency w.r.t. the solution of the optimization problem. During the interval between each two neighbouring updating time, the observer estimates the side slip angle and tire-road friction coefficient by integrating sensor information based on the last update. To find the global optima approximately, a grid search method is implemented for solving non-convex optimization.

5.2.1. Notion of T-observability

To facilitate the analysis of the observer performance, the notion of T-observability is defined.

Definition 5.2.1. *Let $\iota_i(t_0)$, $i = 1, 2$ be two initial states of system (2.16) and $y_i(t)$ be the output corresponding to the trajectory $\iota_i(t)$. Then the system (2.16) is T-observable w.r.t ι at time $t' > t_0 + T$ for some positive T, if $y_1(t) = y_2(t)$, $\forall t \in [t' - T, t']$ implies $\iota_1(t') = \iota_2(t')$.*

Remarks. *If T can be chosen arbitrarily small, the definition of T-observability is equal to the traditional definition of observability for a dynamic system [108]. Hence, the T-observability in this thesis is a looser condition for observability.*

5.2.2. Observer design

5.2.2.1. An optimization based observer

Rewrite (5.1) concisely as

$$\begin{aligned} \dot{\beta} &= f_1(x, t), \\ \dot{\omega} &= f_2(x, t), \end{aligned} \tag{5.4}$$

where $x = [\beta \ \mu_{\max}]^T$. The expression of both f_1 and f_2 can be obtained by comparing (5.1) with (5.4). Besides, denote $[f_1(x,t) \ f_2(x,t)]^T$ as $f(x,t)$. Since the components[2] in $f_1(x,t)$ are all measurable, $f_1(x,t)$ is actually indirectly measured. Let the indirect

[2] They are a_y, ω, v_x.

measured signal of $f_1(x(t), t)$ be $f_{1m}(t)$. With measurement error ignored, there is

$$f_1(x(t), t) = f_{1m}(t).$$

Let

$$\Phi = [\beta_l, \beta_r] \times [\mu_{\max,l}, \mu_{\max,r}]$$

be the domain of all possible values of $(\beta, \mu_{\max})$. Pick a positive number T as the optimization horizon, whose role will soon be clear.

What is particular about the problem in study is that the derivative of both unknown variables are either known or measurable. As a matter of fact, the value of $\dot{\beta}(t)$ can be measured and according to the assumption $\dot{\mu}_{\max}(t) = 0$ whenever $\mu_{\max}(t)$ is continuous. Consequently, if the value of $\beta(t-T)$ is known, $\beta(t)$ can be obtained by integrating $f_{1m}(t)$ over time.

For $t \geq 0$, $0 \leq \tau \leq t$ and $p = [p_\beta \ p_{\mu_{\max}}]^T \in \Phi$, define

$$\begin{aligned} \bar{\beta}_t(\tau|p_\beta) &= p_\beta - \int_{t-\tau}^{t} f_{1m}(s)ds \\ \bar{\mu}_{\max,t}(\tau|p_{\mu_{\max}}) &= p_{\mu_{\max}} \\ \bar{x}_t(\tau|p) &= [\bar{\beta}_t(\tau|p_\beta) \ \bar{\mu}_{\max,t}(\tau|p_{\mu_{\max}})]^T \end{aligned} \tag{5.5}$$

Then given $p_\beta = \beta(t)$ and $p_{\mu_{\max}} = \mu_{\max}(t)$, there are

$$\begin{aligned} \bar{\beta}_t(\tau|p_\beta) &= \beta(t-\tau) \\ \bar{\mu}_{\max,t}(\tau|p_{\mu_{\max}}) &= \mu_{\max}(t-\tau). \end{aligned} \tag{5.6}$$

Introduce the following error functions e_1, e_2 :

$$\begin{aligned} e_1(t|p) &= \int_{t-T}^{t} \Big(f_{1m}(s) - f_1(\bar{x}_t(t-s|p), s) \Big)^2 ds \\ e_2(t|p) &= \int_{t-T}^{t} \Big(\int_{t-T}^{q} f_2(\bar{x}_t(t-s|p), s)ds - \omega(q) + \omega(t-T) \Big)^2 dq \end{aligned} \tag{5.7}$$

Remarks. *Error function $e_1(t|p)$ represents the integration of squared difference between the measured $f_{1m}(t)$ and $f_1(x,t)$ from vehicle model along the optimization horizon T. Besides, $e_2(t|p)$ expresses the integration of squared difference between the measured yaw rate and the one deduced from vehicle model along the optimization horizon T.*

Then, it comes the cost function J:

$$J(t|p) = e_1(t|p) + w \cdot e_2(t|p) \tag{5.8}$$

where w is the weight that reflects the importance of e_2 relative to e_1. It is easy to see that if p_β, $p_{\mu_{\max}}$ are the true values of $\beta(t)$ and $\mu_{\max}(t)$ respectively, then there must be $J(t|p) = 0$. Therefore one can find the set $\mathcal{P}(t)$ that contain the true value of $x(t)$ by solving the equation $J(t|p) = 0$. However this equation may not even have a solution in practice as modelling errors and measurement noises are inevitable. Therefore, instead, the following optimization problem is considered:

$$\mathcal{P}(t) = \text{Arg}\min_{p\in\Phi} J(t|p), \tag{5.9}$$

which is normally a non-convex optimization problem and is solved with a grid search based method, which will be introduced later. Now, the proposed observer is introduced. Define $\mathcal{D}(t)$ as the smallest rectangular that contains $\mathcal{P}(t)$ and define a sequence of discrete time t_k, $k = 1, 2, ...$ defined as $t_k = k\Delta t$, where Δt is the update period of $\mathcal{D}(t)$ from the optimization problem. Let $\hat{\beta}(t)$ and $\hat{\mu}_{\max}(t)$ be the estimated value of β and $\mu_{\max}$ at time t respectively. The observer dynamics is described by the following equations for any $t \in [t_k, t_{k+1})$:

$$\begin{aligned} x^*_{k-1} &= \text{Arg}\min_{p\in\mathcal{D}(t_{k-1})} ||p - x_r(t_{k-1})||, \qquad (5.10)\\ \beta_r(t) &= \beta^*_{k-1} + \int_{t_{k-1}}^{t} f_{1m}(s)ds,\\ \mu_{\max,r}(t) &= \mu^*_{\max,k-1},\\ \dot{\hat{x}}(t) &= -K_\epsilon \cdot \tilde{x}_r(t) + \dot{x}_r(t), \qquad (5.11) \end{aligned}$$

where $x^*_{k-1} = [\beta^*_{k-1} \;\; \mu^*_{\max,k-1}]^T$ which is supposed to be the best solution of x at time t_{k-1} from non-convex optimization, $x_r = [\beta_r \; \mu_{\max,r}]^T$ which is estimated by integrating the measurements based on x^*_{k-1}, $\hat{x} = [\hat{\beta} \; \hat{\mu}_{\max}]^T$ which is the filtered signal of x_r without phase delay, $\tilde{x}_r = \hat{x} - x_r$, $x_r(t_{k-1}) = x^*_{k-2} + [\int_{t_{k-2}}^{t_{k-1}} f_{1m}(s)ds, 0]^T$, K_ϵ is a positive definite matrix as the feedback gain. $\dot{x}_r(t) = [f_{1m}(t) \; 0]^T$ for any $t \in (t_k, t_{k+1})$, otherwise, $\dot{x}_r(t) = \frac{x_r(t) - x_r(t-\Delta s)}{\Delta s}$, where Δs is the sampling time.

The overall diagram of observation process can be seen in Fig. 5.2. At the beginning of each interval $[t_{k-1}, t_k)$, the computing unit collects all the data from the sensors and finish solving the optimization problem in (5.10) before time t_k. Therefore at t_k, the

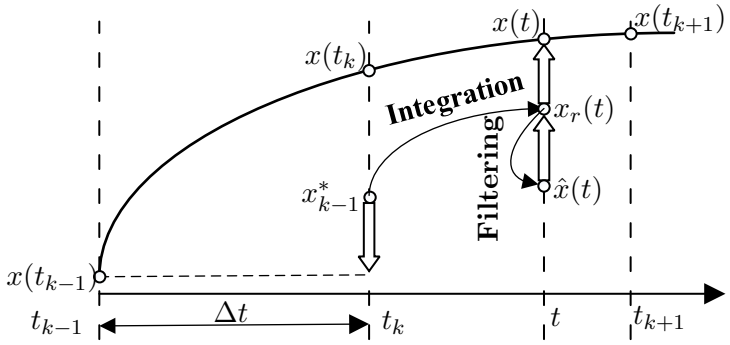

Figure 5.2.: Illustration of the observation process. The variable at the root of a hollow arrow will converge to the variable pointed by that arrow under certain conditions.

value of x^*_{k-1} should already be available. It can be deduced that $x^*_{k-1} = x(t_{k-1})$ if the system is T-observable at t_{k-1}, which implies that the solution of (5.10) at t_{k-1} is unique. For the observer to operate in real-time, it is crucial that Δt is sufficiently large for solving the optimization problem defined in (5.10). After obtaining x^*_{k-1} at t_k, $x_r(t)$ is deduced based on x^*_{k-1} as well as the integration of the measured signal $\dot{x}(t)$. In reality, the model uncertainty, measurement noise and other disturbance will result in jumps in the $x_r(t)$ signal at each t_k. To alleviate this problem, we introduce $\hat{x}$ as the filtered signal of x_r, such that the estimated states $\hat{x}$ is continuous. Finally, the whole observer is summarized in a compact way in Fig. 5.3.

5.2.2.2. Stability and convergence

If the modelling and measurements are assumed to be perfect, then it can be deduced that the observation scheme described above possesses some important properties regarding the stability and convergence of the estimation error. Lyapunov stability of the estimation error can be guaranteed even when the system lacks observability. In the more favorable situation where the trajectory is T-observable at t_k for each positive integer k, global asymptotic stability follows. In the following, these issues will be discussed in detail.

At first, introduce the error variables: $e^{(a)}_k = x^*_k - x(t_k)$, $e^{(b)}(t) = x_r(t) - x(t)$ and recall $\tilde{x}_r(t) = \hat{x}(t) - x_r(t)$. The estimation error satisfies $\tilde{x}(t) = \hat{x}(t) - x(t)$. Then it follows

$$\tilde{x}(t) = \hat{x}(t) - x(t) = e^{(b)}(t) + \tilde{x}_r, \ \forall t \geq 0, \tag{5.12}$$

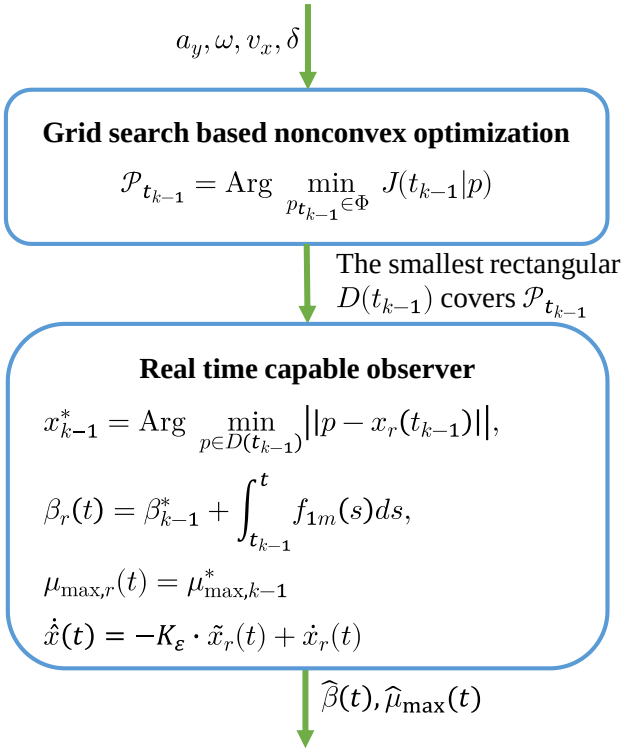

Figure 5.3.: Summary of the proposed observer

$$\dot{x}_r(t) = \dot{x}(t), \ \forall \ t = (t_k, t_{k+1}). \tag{5.13}$$

It follows from 5.13 that for $k \in \mathbb{N}$

$$\dot{e}^{(b)}(t) = 0, \ t \in (t_k, t_{k+1}). \tag{5.14}$$

The following is also true

$$\dot{\tilde{x}}_r(t) = -K_\epsilon \tilde{x}_r(t). \tag{5.15}$$

Since K_ϵ is positive definite, it follows that $\tilde{x}_r = 0$ is globally asymptotically stable.

Let 'diam' denote the diameter of a set. Then we have following properties.

Proposition 5.2.1. *For all $k \in \mathbb{N}^+$, $||e^{(a)}_k|| \leq ||e^{(a)}_{k-1}||$. If there exits a number k_0 such that Diam$(\mathcal{D}(t_{k_0})) \leq r$, where r is some positive constant, then $||e^{(a)}_k|| \leq r$ for any $k > k_0$*

.

Proof. First notice that at any t_{k+1}, the following always holds:

$$x_r(t_{k+1}) = x_k^* + x(t_{k+1}) - x(t_k), \tag{5.16}$$

therefore,

$$e_k^{(a)} = e^{(b)}(t_{k+1}). \tag{5.17}$$

Now consider two situations. In the first situation, suppose $x_r(t_k) \in \mathcal{D}(t_k)$, then according to (5.10), x_k^* is set to $x_r(t_k)$ at $t = t_{k+1}$, which implies $e_k^{(a)} = e^{(b)}(t_k)$. Further using (5.17),

$$e_k^{(a)} = e^{(b)}(t_k) = e_{k-1}^{(a)} \tag{5.18}$$

is obtained. In the second situation, suppose $x_r(t_k) \notin \mathcal{D}(t_k)$, then from (5.10) it is easy to deduce that

$$||x(t_k) - x_k^*|| < ||x(t_k) - x_r(t_k)||,$$

which means that

$$||e_k^{(a)}|| < ||e^{(b)}(t_k)|| = ||e_{k-1}^{(a)}||. \tag{5.19}$$

It follows from (5.18) and (5.19) that the sequence $||e_k^{(a)}||$, $k = 0, 1, ..., +\infty$ is non-increasing.

Suppose k_0 as specified in Proposition 5.2.1 exits. Since both $x(t_{k_0})$ and $x_{k_0}^*$ are in $\mathcal{D}(t_{k_0})$ and $\text{Diam}(\mathcal{D}(t_{k_0})) \leq r$, there is $||e_{k_0}^{(a)}|| \leq r$. Since the sequence $||e_k^{(a)}||$ is non-increasing, $||e_k^{(a)}|| \leq r$ for any $k > k_0$ is deduced. □

Proposition 5.2.2. *The equilibrium $\tilde{x} = 0$ is stable. Furthermore, it is globally asymptotically stable for initial time $t = t_0$ if there exists $t_{k_\epsilon} \geq T + t_0$, such that the system is T-observable w.r.t x at $t = t_{k_\epsilon}$.*

Proof. According to (5.12), there is

$$\tilde{x}(t) \quad = \quad e^{(b)}(t) + \tilde{x}_r.$$

Since the sequence $||e_k^{(a)}||$ is non-increasing, further noticing (5.14), (5.17) and that

$\tilde{x}_r = 0$ is globally asymptotically stable, it can be deduced that $\tilde{x} = 0$ is globally stable.

Furthermore, if the system is T-observable w.r.t x at $t = t_{k_\epsilon}$, there is $||e^{(a)}_{k_\epsilon}|| = 0$, indicating $||e^{(b)}(t_{k_\epsilon+1})|| = 0$. According to Proposition 5.2.1, the sequence $||e^{(b)}(t_k)||$ is also non-increasing, further combining (5.14), it can be thus deduced that the equilibrium $\tilde{x} = 0$ is globally attractive. Since the equilibrium $\tilde{x} = 0$ is also globally stable, it can be concluded that equilibrium $\tilde{x} = 0$ is globally asymptotically stable. □

Proposition 5.2.2 shows that the estimation error of x can be guaranteed not growing even if the system trajectory lacks observability. This can be achieved because the update law for x^*_k specified by (5.10) relies on integration of the sensor information during the period of time when the system trajectory lacks observability. In reality the sensor and computation error is inevitable, so one cannot rely on open-loop integration for too long time. It is crucial that the system recovers observability from time to time for an accurate observation.

It can be noted that while observability is lost, it is usually not easy to guarantee a non-increasing estimation error using some other schemes even without model uncertainties and disturbances. For instance, those methods [101] based on strict Lyapunov functions for time-varying systems usually require persistent excitation conditions. If the persistence of excitation is lost, then the Lyapunov function candidate may have positive time-derivatives, which indicates that the estimation error may actually grow over time.

5.2.2.3. Grid-search based optimization

The optimization problem defined in (5.9) is non-convex in some situations, especially when the vehicle is performing in areas of nonlinear dynamics [8]. As a result, any local optimization methods, such as Sequential Quadratic Programming (SQP) [89], may be trapped in local optima and thus fail to find the global optima. Global non-convex optimization is in general challenging. Stochastic optimization methods, like Differential Evolution [111] (DE), Particle Swarm Optimization [63] (PSO), are possibly good choices. However, if the optimization time or iteration steps are fixed, these methods usually cannot guarantee to output the optimal solution. Therefore, in this work a grid-search method [92] is utilized to approximate the solution of the optimization problem. Grid-search is an exhaustive searching method, so the required search time for obtaining global optima can be calculated. Though it suffers from the curse of dimensionality, there are

only two dimensions in this problem.

The grid-search method is applied as follows:

Considering a balance between numerical precision and computation efficiency, a double discretization is implemented. At first, the parameter domain Φ is discretized into a grid with adaptive resolution and the value of the cost function is evaluated at each vertex of the grid to find the optimal solution. Once the parameter node corresponding to the optimal solution is found, one may choose a smaller region $\Phi_1 \in \Phi$ that contains the best node. A discretization of the region Φ_1 with higher resolution can be made for further searching the final optimal solution. This procedure can be carried out iteratively.

The details of the grid-search algorithm are described in Fig.5.4 and Fig.5.5. In Fig.5.4, the parameter domain Φ is discretized with adaptive resolution. Firstly begin with how the grid is adaptively discretized. As is known, at t_{k-1}, for a fixed $F_{yf}(t_{k-1})$ without being zero, the absolute value of the corresponding $\alpha_{f,l}(t_{k-1})$ based on linear tire model is smaller than $\alpha_f(t_{k-1})$ from nonlinear tire model, see Fig. 5.6. Thus, on the basis of these two front tire slip angles, there are different side slip angles β_{cl} and β shown in the following

$$\beta_{cl}(t_{k-1}) = \alpha_{f,l}(t_{k-1}) - \frac{l_f\omega(t_{k-1})}{v_x(t_{k-1})} + \delta(t_{k-1}), \tag{5.20}$$

$$\beta(t_{k-1}) = \alpha_f(t_{k-1}) - \frac{l_f\omega(t_{k-1})}{v_x(t_{k-1})} + \delta(t_{k-1}), \tag{5.21}$$

where both $\beta_{cl}(t_{k-1})$ and $\beta(t_{k-1})$ are calculated based on single track model. Subsequently, by subtracting (5.21) from (5.20),

$$\beta_{cl}(t_{k-1}) - \beta(t_{k-1}) = \alpha_{f,l}(t_{k-1}) - \alpha_f(t_{k-1}). \tag{5.22}$$

is deduced. The following observer is utilized to estimate $\alpha_{f,l}(t_{k-1})$,

$$\dot{\alpha}_{f,l} = (a-b)(\cos\delta)C_f\alpha_{f,l} + bma_y - \omega - \dot{\delta}, \tag{5.23}$$

which is based on (4.3b) in section 4.2.2, where $C_f\alpha_{f,l}$ is used to replace the front axle lateral force F_{yf}, and C_f refers to front axle cornering stiffness based on linear single track model. Finally, there is following property:

$$\begin{aligned} \beta_{cl}(t_{k-1}) &\leq \beta(t_{k-1}) \quad \alpha_{f,l}(t_{k-1}) \geq 0, \\ \beta_{cl}(t_{k-1}) &> \beta(t_{k-1}) \quad \alpha_{f,l}(t_{k-1}) < 0. \end{aligned} \tag{5.24}$$

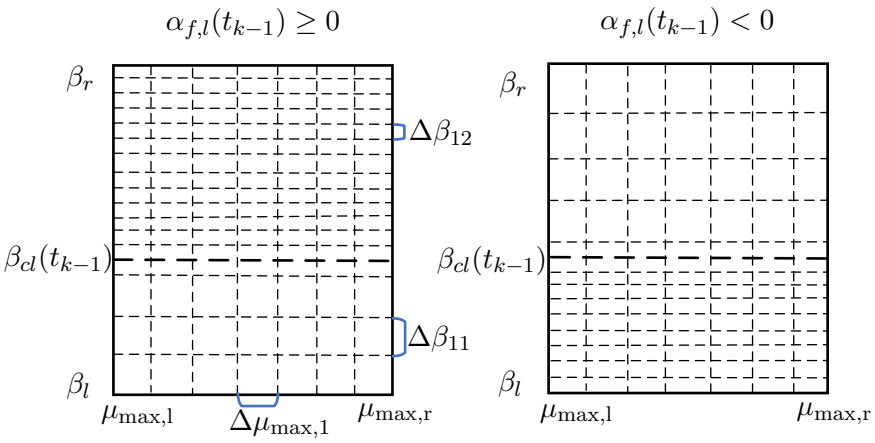

Figure 5.4.: Discretization of Φ with adaptive resolution.

This property is further explained in Appx. D. Therefore, when $\alpha_{f,l}(t_{k-1})$ is larger than or equal to zero, the real side slip angle $\beta(t_{k-1})$ should be also larger than or equal to $\beta_{cl}(t_{k-1})$ and thus the nodes in the corresponding areas with higher resolution ($\Delta\beta_{12}$) are evaluated as shown in Fig. 5.4, and vice versa.

After the parameter node corresponding to the optimal solution in Φ is found, a smaller region $\Phi_1 \in \Phi$ shown in Fig. 5.5 is chosen that contains the best node to further search the more accurate solution with higher resolution ($\Delta\beta_2$, $\Delta\mu_{\max,2}$). Considering the measurement noise, model uncertainty as well as observability influence on the cost evaluations, the whole nodes (within Φ_1) whose costs are smaller than k times of the new evaluated minimum cost are collected. Then, among these nodes the minimum and maximum β as well as $\mu_{\max}$ are chosen, which form the boundary of $\mathcal{D}(t_{k-1}) \in \Phi_1$. Finally, in $\mathcal{D}(t_{k-1})$ the node x^*_{k-1} closest to the $x_r(t_{k-1})$ is chosen which is calculated by integration based on the selected node from last grid-search.

5.3. Simulation and experiment results

5.3.1. Simulation results

In this part, based on a nonlinear single track model including lateral load transfer, four different maneuvers — sinusoidal, step steer, double lane change as well as a random maneuver — are simulated to show the tire-road friction estimation results, which is analogue to the procedure explained in the section 4.5 dealing with methods including

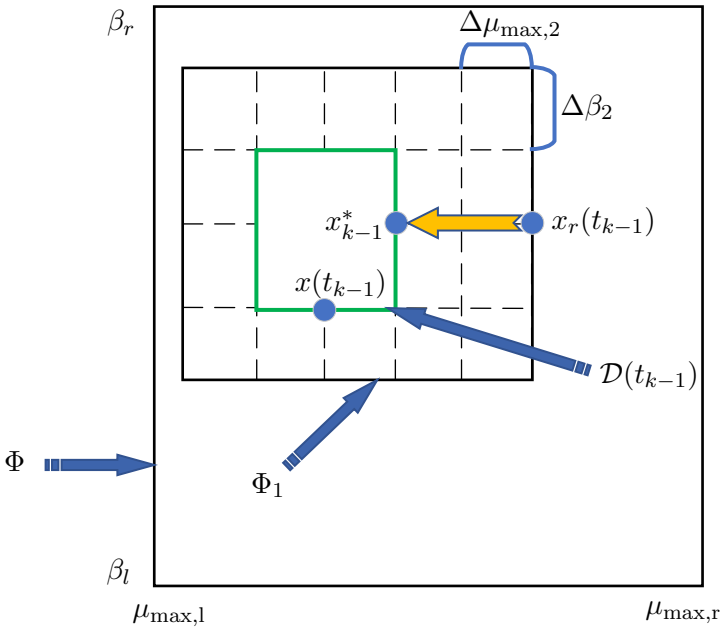

Figure 5.5.: Discretization of Φ_1 with higher resolution.

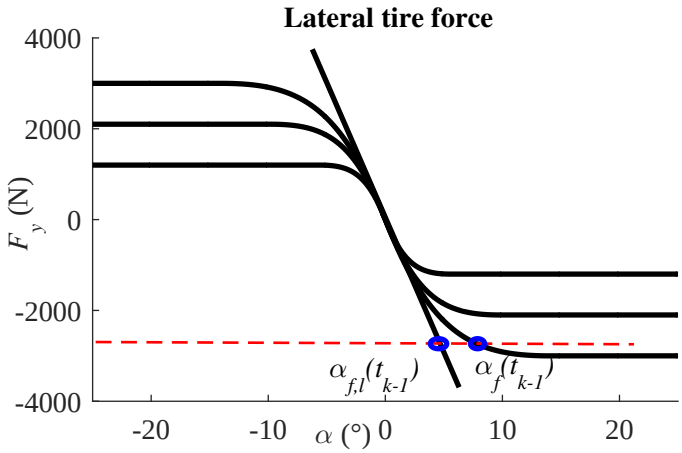

Figure 5.6.: Linear and nonlinear tire model characteristics. For a given tire lateral force, the tire slip angles of the linear tire model are consistently smaller than those of the nonlinear tire model.

the tire self-aligning torque. In the following simulation, the proposed optimization based observer is abbreviated as opti. Besides, a linearization based observer (lbo) [3] from [37] is introduced as a comparison. The settings conducted for the opti and lbo for simulations can refer to Table 5.1 and Table 5.2, separately. It can be noted that the optimization horizon in simulation is 0.35 s, and the update period of the optimization result is 0.1 s, indicating that the grid-search optimization should be finished within 0.1 s. With respect to the discretization in Φ, the length of edge in β direction consist of $\Delta\beta_{11} = 0.015$ rad and $\Delta\beta_{12} = 0.004$ rad, and the length of edge in $\mu_{\max}$ direction is 0.1. It has to be mentioned that search length of β means the diameter of the β set in Φ_1 in the second discretization, so is the search length of $\mu_{\max}$ in Φ_1[4]. Furthermore, the nodes with cost function smaller than k times of the minimum cost[5] constitute $\mathcal{D}(t)$.

The simulation results are illustrated in Fig. 5.7 — Fig. 5.10 for the different maneuvers. Besides, Table 5.3 and Table 5.4 show the statistical analysis (mean value of estimation error (MVE) and root mean square of estimation error (RMS)) of the estimated β and $\mu_{\max}$ from opti and lbo. As can be seen, opti can guarantee stability of $\mu_{\max}$ and β estimation in a wider range of vehicle operations than lbo. Besides, opti can estimate $\mu_{\max}$ and β overall better than lbo (in stable situation) in terms of RMS. In Fig. 5.7, β from opti can converge to the real β within 1 s while β from lbo needs more than 2 s. For $\mu_{\max}$ estimation, opti can estimate the real value much faster than lbo, especially on low friction road condition where opti takes 1 s while lbo up to 8 s. W.r.t. RMS, results from opti are approximately the same (β) and half ($\mu_{\max}$) of those from lbo, respectively, demonstrating the higher accuracy. In Fig. 5.8, the step steer maneuver doesn't offer persistent excitation for lbo, so both β and $\mu_{\max}$ have deviation to the real values. But this excitation is already enough for opti to obtain good estimation results, which is also illustrated by the statistical analysis from Table 5.3 and Table 5.4. In Fig. 5.9, opti estimates β as good as lbo. However, w.r.t. $\mu_{\max}$ estimation, opti can still accurately obtain the real results both on high and low friction road conditions while lbo can not on low friction road condition. Besides, $\mu_{\max}$ from lbo converges slower than that from opti on high friction road condition. What interesting is that RMS of $\mu_{\max}$ from lbo is slightly better than that from opti, this is because between 4.5 s and 6 s both $\mu_{\max}$ estimation results from opti and lbo are frozen and estimated $\mu_{\max}$ from lbo is coincidently close to the real value, leading to lower RMS. In Fig. 5.10, the real $\mu_{\max}$

[3] The lbo is widely implemented for simultaneously side-slip angle and tire-road friction estimation[37, 67, 68].

[4] An example is given to explain the search length in detains: let $\Phi_1 = [\beta_{\epsilon,l}, \beta_{\epsilon,r}] \times [\mu_{\epsilon,l}, \mu_{\epsilon,r}]$, then search length of β and $\mu_{\max}$ in the second discretization are $\beta_{\epsilon,r} - \beta_{\epsilon,l}$ and $\mu_{\epsilon,r} - \mu_{\epsilon,l}$, respectively.

[5] Based on the evaluation of nodes in Φ_1.

changes from high friction to low friction, finally jump to the medium road condition. From 0 to 5 s, both opti and lbo cannot estimate $\mu_{\max}$ accurately, because the excitation is too small, leading to the tire force staying in the quasi-linear region. From 5 s to 12 s, the road condition decrease to 0.3, which brings the tire force into highly nonlinear region, resulting in the instability of lbo. However, opti performs still quite well. Even when the road condition finally jumps to 0.5, lbo is still not able to fast converge to the real $\mu_{\max}$ while opti can always reach the real one quite fast.

Table 5.1.: Parameters for the proposed optimization method.

	Simulation	Experiment
General parameters	Sampling time: 0.01 s Optimization horizon T : 0.35 s Update period Δt : 0.1 s	Sampling time: 0.01 s Optimization horizon T : 1 s Update period Δt : 0.1 s
First discretization in Φ	$\beta_l = -0.15$ rad, $\beta_r = 0.15$ rad $\mu_{\max,l} = 0.05$, $\mu_{\max,r} = 1.15$ $\Delta\beta_{11} = 0.015$ rad, $\Delta\beta_{12} = 0.004$ rad $\Delta\mu_{\max,1} = 0.1$	$\beta_l = -0.15$ rad, $\beta_r = 0.15$ rad $\mu_{\max,l} = 0.05$, $\mu_{\max,r} = 1.15$ $\Delta\beta_{11} = 0.015$ rad, $\Delta\beta_{12} = 0.004$ rad $\Delta\mu_{\max,1} = 0.1$
Second discretization in Φ_1	Search length of β: 0.035 rad Search length of μ_{max}: 0.3 $\Delta\beta_2 = 0.0005$ rad $\Delta\mu_{\max,2} = 0.03$ $k = 1.05$	Search length of β: 0.035 rad Search length of μ_{max}: 0.3 $\Delta\beta_2 = 0.001$ rad $\Delta\mu_{\max,2} = 0.03$ $k = 1.2$
Filter for final results	$K_\epsilon = \begin{bmatrix} \min(10, \frac{0.03\text{sign}(\tilde{\beta}_r)}{\tilde{\beta}_r}) & 0 \\ 0 & 3 \end{bmatrix}$	$K_\epsilon = \begin{bmatrix} \min(10, \frac{0.3\text{sign}(\tilde{\beta}_r)}{\tilde{\beta}_r}) & 0 \\ 0 & 3 \end{bmatrix}$

Table 5.2.: Basic information of observer from [37]

	Observer	Simulation	Experiment
lbo	$\dot{\hat{v}}_y = a_y - \omega v_x + k_{vy}(a_y - \hat{a}_y(\hat{v}_y, \hat{\mu}_{\max}))$ $\dot{\hat{\mu}}_{\max} = k_\mu \frac{\partial \hat{a}_y}{\partial \hat{\mu}_{\max}} (\frac{\partial \hat{a}_y}{\partial \hat{v}_y})^{-1}(a_y - \hat{a}_y(\hat{v}_y, \hat{\mu}_{\max}))$	$k_{vy} = 0.08$ $k_\mu = 7$	$k_{vy} = 0.15$ $k_\mu = 4$

Table 5.3.: Statistical analysis of the estimated side slip angle from opti and lbo in simulations and experiments: MVE means mean value of estimation error and RMS denotes root mean square of estimation error.

		MVE ($\beta°$)		RMS ($\beta°$)	
		opti	lbo	opti	lbo
Simulation	Sinusoidal (mixed $\mu_{\max}$)	-0.029	-0.055	0.150	0.158
	Step steer (mixed $\mu_{\max}$)	-0.015	-0.076	0.065	0.103
	Double lane change (mixed $\mu_{\max}$)	-0.015	-0.012	0.065	0.040
	Random (mixed $\mu_{\max}$)	-0.009	-0.090	0.098	0.212
Experiment	Step steer (high $\mu_{\max}$)	0.101	0.252	0.266	0.319
	Slope steer (high $\mu_{\max}$)	-0.236	-0.206	0.352	0.288
	Random (low $\mu_{\max}$)	0.447	0.159	0.773	0.379
	Slope steer (low $\mu_{\max}$)	-0.376	0.059	0.635	0.191

Table 5.4.: Statistical analysis of the estimated $\mu_{\max}$ from opti and lbo in simulations and experiments: MVE means mean value of estimation error and RMS denotes root mean square of estimation error.

		MVE ($\mu_{\max}$)		RMS ($\mu_{\max}$)	
		opti	lbo	opti	lbo
Simulation	Sinusoidal (mixed $\mu_{\max}$)	-0.004	-0.069	0.126	0.219
	Step steer (mixed $\mu_{\max}$)	-0.008	-0.162	0.166	0.235
	Double lane change (mixed $\mu_{\max}$)	0.042	0.012	0.095	0.076
	Random (mixed $\mu_{\max}$)	0.040	-0.426	0.150	0.582
Experiment	Step steer (high $\mu_{\max}$)	0.155	0.361	0.271	0.400
	Slope steer (high $\mu_{\max}$)	0.424	0.346	0.488	0.438
	Random (low $\mu_{\max}$)	-0.070	-0.479	0.368	0.531
	Slope steer (low $\mu_{\max}$)	-0.255	-0.746	0.488	0.746

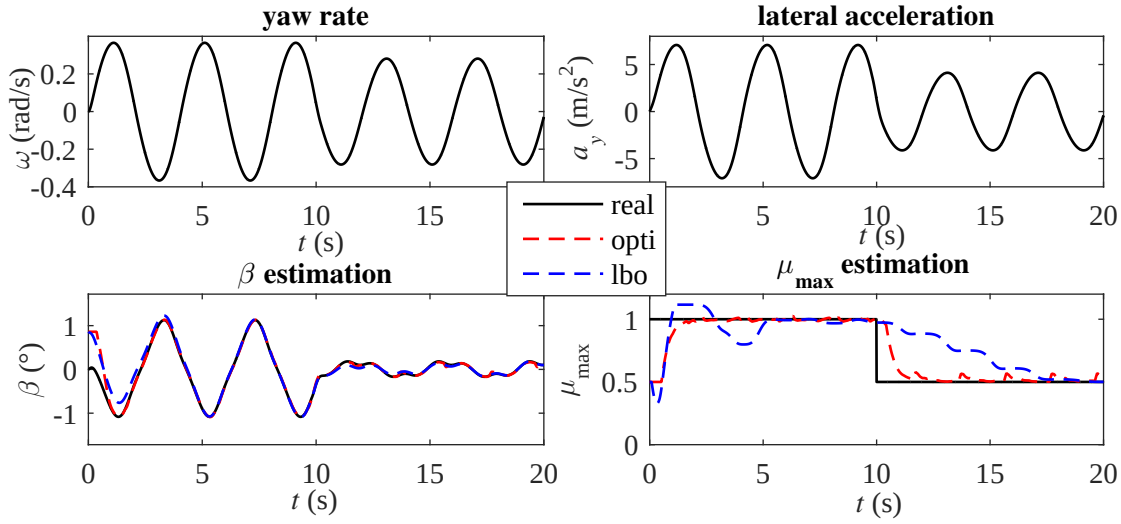

Figure 5.7.: Sinusoidal maneuver from high friction ($v_x = 20$ m/s) to low friction road condition ($v_x = 15$ m/s): wheel steering angle amplitude is 0.05 rad, frequency is 0.25 Hz.

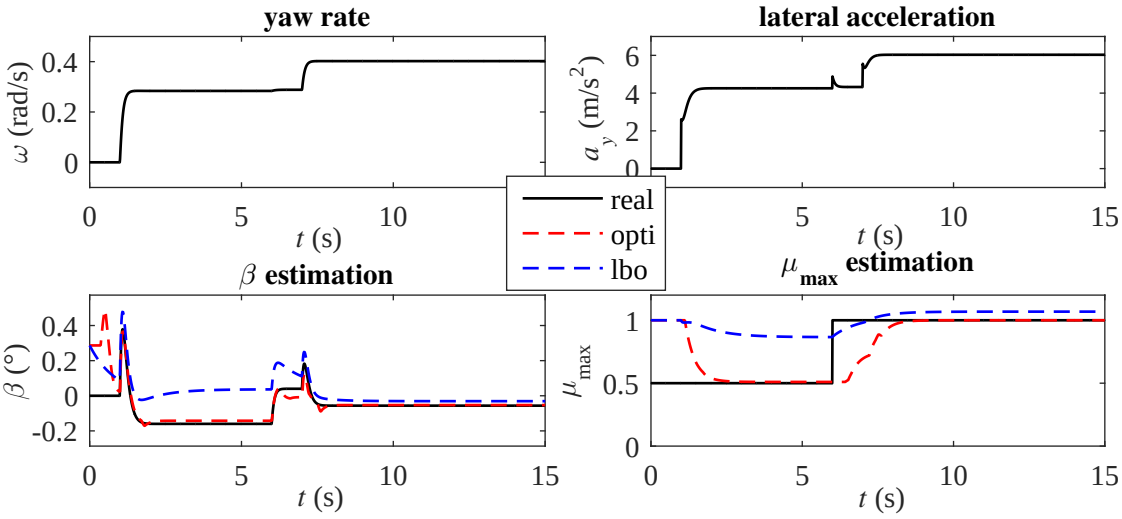

Figure 5.8.: Step steer maneuver from low friction to high friction road condition: $v_x = 15$ m/s. Under low friction road condition, the wheel steering angle jumps from 0 to 0.05 rad and then from 0.05 rad to 0.07 rad under high friction road condition.

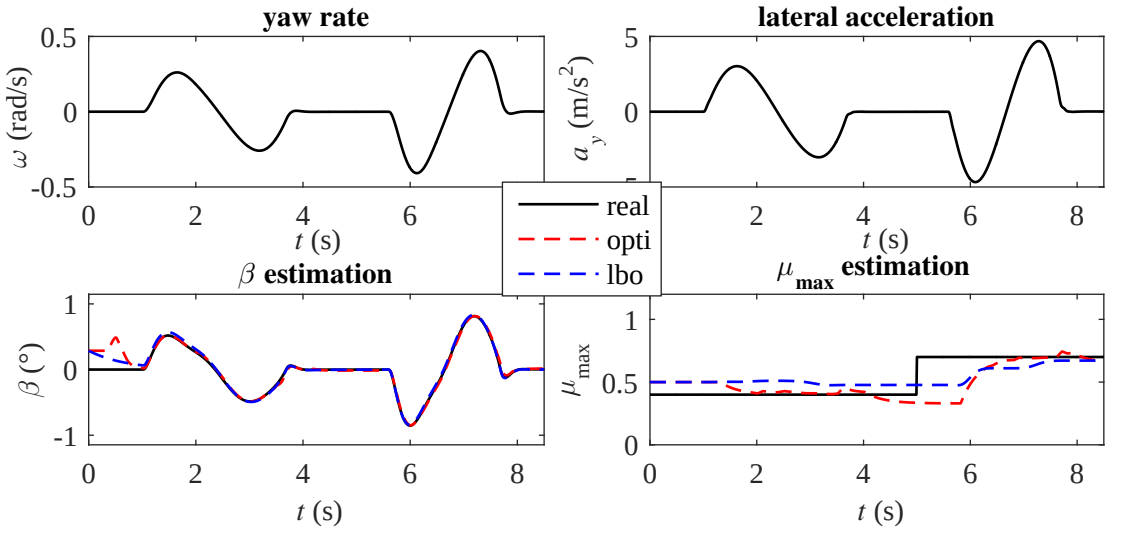

Figure 5.9.: Double lane change maneuver from low friction to medium friction road condition: $v_x = 12$ m/s.

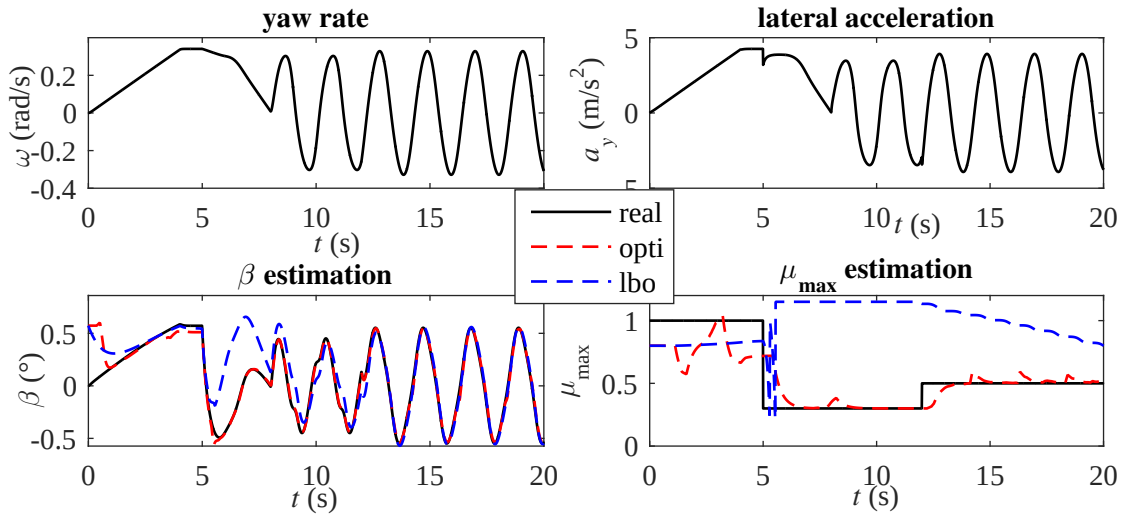

Figure 5.10.: Random maneuver from high friction to low friction, finally to medium road condition: $v_x = 12.5$ m/s.

5.3.2. Experiment results

As explained in section 4.5.2, the vehicle experiments are conducted both in Nardò [5] (concrete test track) and Arjeplog [4] (grinded ice test track) with a racing car called Roding Roadster. The resources of measurements and references as well as other details can be found in section 4.5.2. What has to be mentioned is that, due to the speed sensor failure, the reference lateral veloctiy in the grinded ice test track is replaced by that from a well parametrized nonlinear single track model. The parameters and settings conducted for the opti and lbo for experiments can be found in Table 5.1 and Table 5.2, separately. It can be noted that, compared to the optimization horizon (0.35 s) in simulation, it is set to 1 s in the experiment, such that the influence of model uncertainty and measurement noise on the estimation results can be better reduced. The other settings for optimization in the experiments are similar to those in simulation, except for $\Delta\beta_2 = 0.001$ rad and $k = 1.2$ as well as $K_\epsilon = \begin{bmatrix} \min(10, \frac{0.3\text{sign}(\tilde{\beta}_r)}{\tilde{\beta}_r}) & 0 \\ 0 & 3 \end{bmatrix}$. The reasons for the setting differences are as follows: W.r.t. $\Delta\beta_2$, it is set in experiments larger than that in simulations for reducing calculation burden caused by the long optimization horizon, such that the estimated side slip angle and $\mu_{\max}$ from optimization can be updated in each Δt; For k, theoretically speaking, even it is set to 1, the real $(\beta, \mu_{\max})$ should be

within the region $\mathcal{D}(t)$. However, due to the influence of the measurement noise and model uncertainty, the real $(\beta, \mu_{\max})$ may jump out of the region $\mathcal{D}(t)$ if k is 1 or set too small. Thus in the experiments, k is set larger than that in simulations for guaranteeing $\mathcal{D}(t)$ to contain the real $(\beta, \mu_{\max})$; W.r.t. K_ϵ as gain matrix for observer, the settings in K_ϵ should be correspondingly adapted for better estimation considering the measurement noise and model uncertainty.

The experimental results are depicted in Fig. 5.11 and Fig. 5.12 for the concrete test track, and Fig. 5.13 and Fig. 5.14 for the grinded ice test track. Besides, Table 5.3 and Table 5.4 show the statistical analysis (mean value of estimation error (MVE) and root mean square of estimation error (RMS)) of β and $\mu_{\max}$ estimation results from opti and lbo, respectively. It can be concluded that opti can guarantee stability in a wider range of vehicle operations than lbo. Besides, in terms of RMS, opti can estimate tire-road friction coefficient much better than lbo both on high and low friction road condition; On the contrary, opti performs overall similar as lbo in side slip angle estimation on high friction road condition but worse than lbo on grinded ice test track. On the concrete test track, in Fig. 5.11, opti can estimate tire-road friction (RMS 0.271) and side slip angle (RMS 0.266°) better than those (RMS 0.400 ($\mu_{\max}$) and 0.319° (β)) from lbo, especially from 8 s to 12 s, during which the tire-road friction estimation from opti is still good while that from lbo becomes inferior. In Fig. 5.12, both opti and lbo perform well. From 10 s on, lbo illustrates even slightly faster convergent ratio than opti in tire-road friction estimation. On the grinded ice test track, in Fig. 5.13, opti can always output a stable tire-road friction coefficient while lbo cannot. Around 20 s, estimation result of $\mu_{\max}$ in lbo diverges and doesn't converge to vicinity of real value until at 40 s. What interesting is lbo with RMS (0.379°) can estimate side slip angle better than opti with RMS (0.773°). A possible explanation is that, when the tires come into highly saturate region, the cost function (5.8) is sensitive to the variation of the tire-road friction while robust to the tire slip angle (so is the side slip angle). Consequently, combined with model uncertainty and measurement noise, the size of $\mathcal{D}(t)$ in opti may be augmented, especially the length of β, leading to the increase of estimation error in β. In Fig. 5.14, similar performance like in Fig. 5.13 is shown, i.e. opti can estimate tire road friction better than lbo, while lbo can observe side slip angle better than opti.

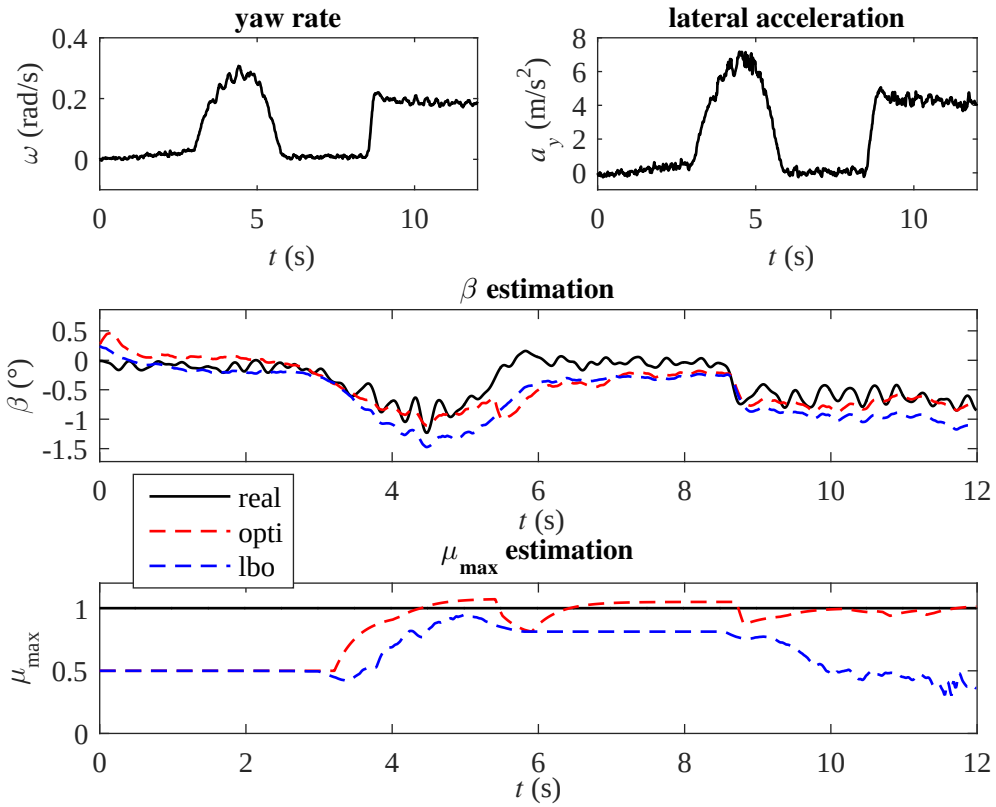

Figure 5.11.: Step steer maneuver on high friction road condition: $v_x = 25$ m/s.

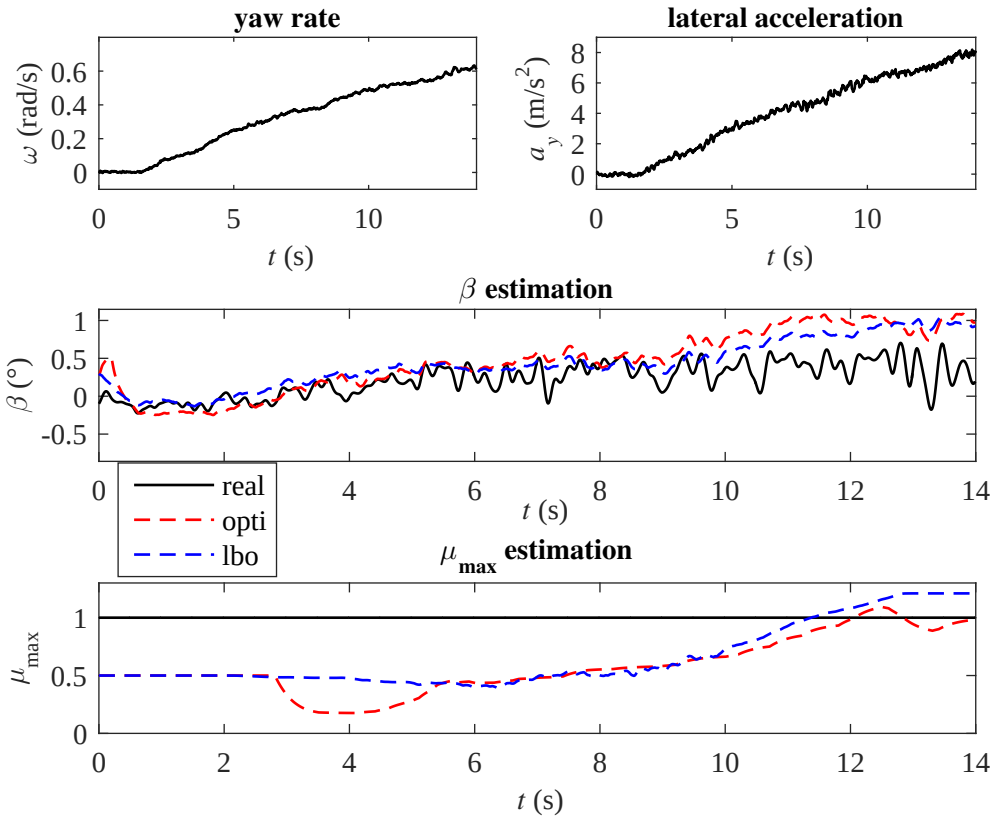

Figure 5.12.: Slope steer on high friction road condition: $v_x = 12.5$ m/s.

5.4. Discussion

In this chapter, a method (**method III**) was proposed for estimating $\mu_{\max}$ based on vehicle lateral dynamics without self-aligning torque information. When the system is T-observable from time to time (much weaker condition than traditional observable definition), the estimation error of side-slip angle and tire-road friction coefficient is globally asymptotically stable, demonstrating that the observer works in a wide range of vehicle operations. Besides, under no model uncertainty and measurement noise influence, the estimation error does not grow even when the system lacks observability. Furthermore, the proposed framework of this observer guarantee that it is able to run in real time. Moreover, the sensors applied for the observer design are from mass produced vehicles. Finally, by comparing the **method III** with a linearization based observer (lbo)

under various simulations and experiments, it is demonstrated that: 1) the **method III** can guarantee stability of estimation in a wider range of vehicle operations than lbo; 2) W.r.t. root mean square of estimation error (RMS), the performance from method III is overall better than that from lbo in $\mu_{\max}$ estimation. Therefore, the criteria presented in the objective for tire-road friction estimation algorithms in this thesis are satisfied.

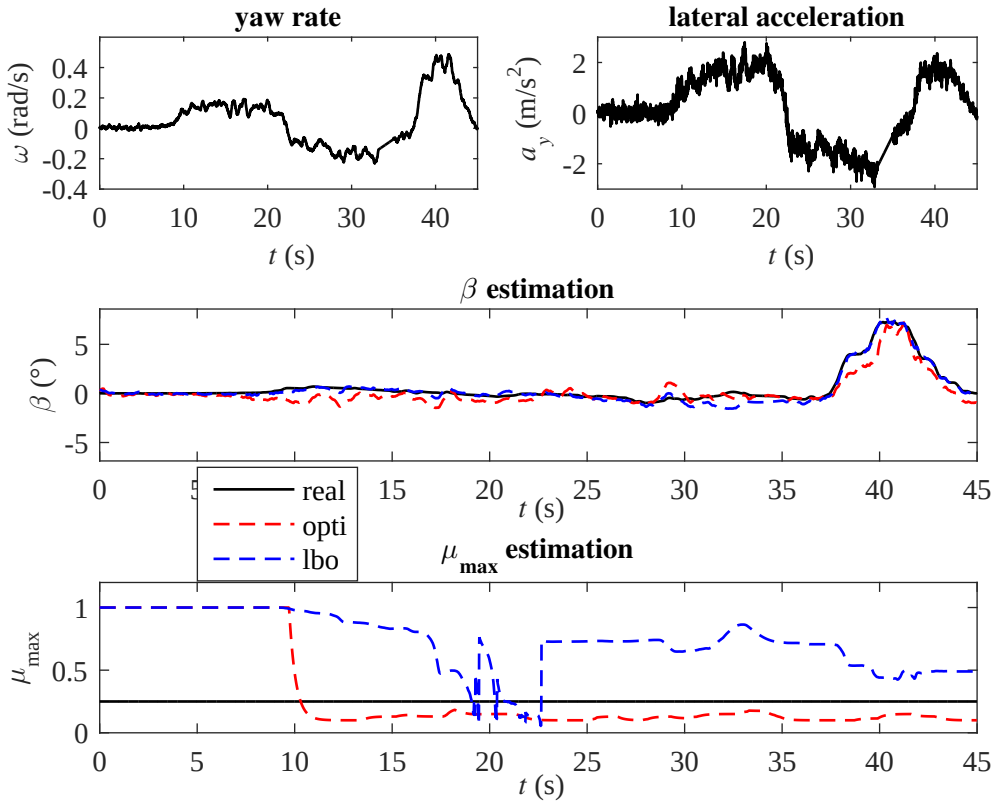

Figure 5.13.: Random steering maneuver on low friction road condition: v_x is slow varying around 12 m/s from 0 to 25 s, then changes to 7 m/s and stay around it.

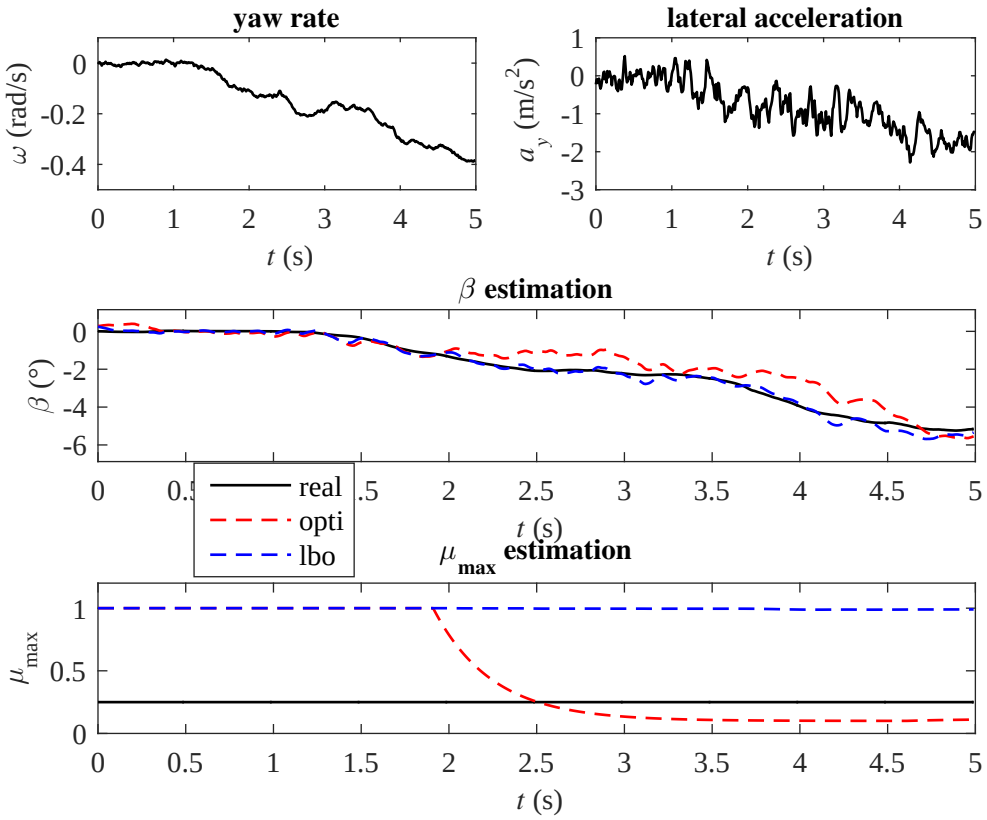

Figure 5.14.: Slope steer on low friction road condition: $v_x = 5.5$ m/s.

6. Summary

6.1. Conclusion

The acquisition of an accurate tire-road friction coefficient can significantly augment the performance and reliability of the existing vehicle dynamics control like ABS, ESC, offering the potential to further decrease loss-of-control accidents. Moreover, as the automation of driving advances, the automated system needs to take the responsibility from the driver to adapt the driving style to the change of road conditions. However, as presented in the state of the art, it is extremely difficult to estimate TRFC accurately and reliably in real time based on vehicle systems. One drawback of TRFC estimation is the need of installing additional sensors which gain costs of vehicles (mainly for cause-based methods). Another shortcoming is that few methods can mathematically guarantee the stability of $\mu_{\max}$ estimation in wide range of vehicle operations, leading to no guarantee of accuracy and reliability in $\mu_{\max}$ estimation (mainly for effect-based methods).

The presented research deals with developing observers for estimating TRFC based on vehicle lateral dynamics with sensors available on the current mass produced vehicles. The observers are real time capable and asymptotically stable in a wide range of vehicle operations. Besides, they were validated by simulations and experiments in various maneuvers. The proposed observers can be classified into two branches of methods for TRFC estimation depending on the availability of tire self-aligning torque (TSAT). The first branch contains two methods with TSAT information: the **method I** is a nonlinear adaptive observer with an indirect measurement based on estimated total aligning torque and front axle lateral force, while the **method II** proposed a more advanced nonlinear adaptive observer with no need to estimate front axle lateral force. In the second branch, a **method III** without TSAT information is presented. This method proposed an optimization based observer, with guarantee on real time capability and finding the global optima. The more detailed summary of the whole research is as follows:

The **chapter 1** (Introduction) initially introduced current situations of road traffic fatalities and its influence on the victims and world economics. Then, the significance of TRFC estimation for conventional and automated vehicles in improving road safety was discussed. Finally, the objective, outline and contributions of this research was presented.

The **chapter 2** (Background) started to describe some basics about TRFC. Then the state of the art of TRFC estimation was provided. Emphasis was laid on the effect-based methods, especially on the vehicle dynamics based methods and then it was concluded that the TRFC estimation based on vehicle lateral dynamics is actually a nonlinear observer design problem. Thus, methods for nonlinear state and parameter estimation, focusing on nonlinear adaptive observers, were subsequently summarized. Therein, different nonlinear adaptive observers were introduced based on the structure of dynamic systems and the other observers were briefly reviewed with their mechanism, pros and cons. Afterwords, why it is difficult to design observers for TRFC estimation was explained. Finally, the key ideas of how to tackle this nonlinear parameter estimation problem in this research were presented.

The **chapter 3** (Vehicle model) introduced a nonlinear single track model with a steering system utilized for TRFC estimation. The single track model was expressed with yaw rate and lateral velocity as state variables considering lateral load transfer. Besides, the tire model TMsimple and TMeasy were chosen to model tire lateral force and tire self-aligning torque, respectively, based on the comparison among magic formula, brush model as well as TMsimple/TMeasy. Furthermore, the steering system was modelled by a second order differential equation with available tie rod force measured by steering gauge sensors. Finally, the process of how to utilize the tie rod force to estimate front axle total aligning torque was demonstrated.

The **chapter 4** (Tire-road friction coefficient estimation with tire self-aligning torque) demonstrated two methods.

In **method I**, a framework was proposed to estimate TRFC with asymptotic stability and robustness guarantee using total aligning torque (including self-aligning torque) in the vehicle front axle during steering. Firstly, a novel strategy was proposed to estimate the front axle tire lateral force which performs better than the classical unknown input observer (UIO). Then, combined with an indirect measurement based on the estimated total aligning torque and front axle tire lateral force, a nonlinear adaptive observer was designed to estimate TRFC with asymptotic stability guarantee. To increase the

robustness of the estimation result, criteria were proposed to decide when to update the estimated TRFC.

Though method I is simple to implement, the indirect measurement is singular when total aligning torque approaches zero. Meanwhile, front axle lateral force needs to be extra estimated. Therefore, a method II, aiming at eliminating aforementioned shortcomings, is proposed. It presented a nonlinear adaptive observer to estimate TRFC with no need to estimate front axle lateral force. Firstly, the vehicle lateral dynamics model is transformed into a lower-triangular form with yaw rate, x_f (front axle tire slip angle above TRFC) and TRFC as state variables. Then, for non-affine parametrized systems in such a form, a nonlinear adaptive observer was proposed and its estimation error was proved to be exponentially stable by constructing a strict Lyapunov function. Finally, the design procedure was applied to the TRFC estimation problem with proper modifications. It has to be mentioned that the proposed nonlinear adaptive observer is universally applicable if other dynamic systems featuring the same system form (a lower-triangular form) satisfy the corresponding assumptions for this observer.

The TRFC estimation results among **method I** and **method II** as well as Extended Kalman Filter (EKF) were demonstrated and compared in both simulations and experiments. The results showed that both **method I** and **method II** can guarantee stability of TRFC estimation in a wider range of vehicle operations than EKF. Furthermore, in terms of root mean square of TRFC estimation error (RMS), the performance from **method I**, **method II** and EKF (in stable situation) is overall similar. Moreover, **method I** and **method II** are both real time capable.

The **chapter 5** (Tire-road friction coefficient estimation without tire self-aligning torque) proposed a method without utilizing tire self-aligning torque. Though estimating TRFC with tire self-aligning torque is attractive, the availability and signal quality of tire self-aligning torque cannot always be assured. Hence, the identification of TRFC without tire self-aligning torque was also investigated. A **method III** was thus introduced:

Method III is an optimization based observer. This observer proposed an innovative scheme consisting of a non-convex optimization part and an integration part. The non-convex optimization is only utilized to estimate side slip angle and TRFC as initial value for integration, thus, there is sufficient time left for finding the global optima through adaptive resolution based grid-search. During the search of the global optima, the integration was applied based on previously obtained initial value to calculate side slip angle and TRFC. This can be realized since the derivative of side slip angle is measurable

and the derivative of TRFC is assumed to be zero. Therefore, by interweaving discrete time solution of the optimization and continuous integration of derivatives from sensor data, the scheme allows for sufficient time for finding the global optima. Meanwhile, despite of the non-convex optimization, the observation scheme is able to run in real time. One advantage of the proposed observer is that, under no model uncertainty and measurement noise influence, the estimation error does not grow even when the system lacks observability. When observability requirement is satisfied, global asymptotic stability of the observer can also be guaranteed. The estimation results from the proposed observer and a linearization based observer (lbo) were finally compared under various road conditions with simulations and experiments. The results showed that **method III** performs better than lbo (in stable situations) w.r.t. root mean square of TRFC estimation error and can always guarantee stability in a wide range of vehicle operations while lbo cannot.

In summary, the present research proposed three different methods to estimate tire-road friction coefficient based on the sensors from mass produced vehicles. These methods can be divided into two branches depending on the availability of tire self-aligning torque which can support estimating TRFC with less excitation requirement from driver compared with purely tire lateral force. All these methods can work in real time and operate in a wide range of vehicle states with accuracy and reliability guarantee. Therefore, these algorithms may be applied for increasing the performance and reliability of the existing vehicle dynamics control and advanced functions in the automated vehicles, and thus accelerate the progress of bringing automated vehicles on the market.

6.2. Outlook

Based on the presented research, the following advices could further improve the tire-road friction coefficient estimation results.

6.2.1. Consideration of uncertainty in tire cornering stiffness

The presented research assumed the tire cornering stiffness is accurately known and only related to tire normal force. Actually, it is highly influenced by tire inflation pressure, tire tread-depth and tire temperature as well as other factors [106], which will affect the TRFC estimation result [101]. According to [101], 10% under- or overestimation of tire cornering stiffness brings about roughly 10% estimation error of TRFC. Therefore,

in future work, it is necessary to propose a real time capable and reliable method for updating the tire cornering stiffness. For this, an expression, to account for its variations in the tire inflation pressure, tire tread-depth, tire temperature as well as some other factors measured by tire based sensors [106], should be investigated. Some maneuver-dependent adaptive observers may be a good compensation for better accuracy of tire cornering stiffness [104, 82].

6.2.2. Combination of longitudinal and lateral dynamics

For TRFC estimation, the researchers usually only focus on maneuvers with purely longitudinal and lateral dynamics, which already cover many situations. However, combined longitudinal and lateral dynamics exists, for instance, during aggressive lane change, the driver may not only steer the wheels but also brake, resulting in highly combined vehicle dynamics. In this situation, the tire model for purely lateral dynamics does not hold anymore, because the generated tire slip ratio in longitudinal dynamics will already highly affect the tire characteristics in the lateral force. Besides, the longitudinal force during steering will also exert extra lateral force and yaw moment on vehicle, leading to variation of lateral dynamics. Omitting these influences may bring estimation errors of TRFC. Therefore, combined vehicle dynamics in TRFC estimation will be also considered for the future work.

6.2.3. Introduction of more sensors and techniques

With the development of automated vehicles, more sensors, such as GPS, tire force sensors, camera, will be installed on the car. Based on these information, the velocity estimation process is independent of the tire model, eliminating the largest uncertainties in the real application[88]. Therefore, the tire model is only used to fit the obtained tire slips and forces for tire-road friction estimation. Besides, the Car-to-X techniques are able to receive historical friction data from the connected cars and data from weather stations[91], which can offer relative reliable friction condition of the current road when there are not enough excitation for vehicle-dynamics based TRFC estimation. Meanwhile, with this technology it will be possible to predict the TRFC of the oncoming road, allowing for modification of the driving style. Therefore, introducing these sensors and new techniques will significantly enhance the TRFC estimation accuracy and reliability in the future.

List of Figures

List of Tables

Bibliography

[1] Road vehicles - lateral transient response test methods. ISO 7401: 2011(en), International Organization for Standardization, 2011.

[2] Global status report on road safety 2015. Technical report, World Health Organization, 2015.

[3] Transforming our world: The 2030 agenda for sustainable development. Technical report, United Nations, 2015.

[4] http://atmab.com/. Accessed on 13.07.2018, Arjeplog Test Management, 2018.

[5] https://www.porscheengineering.com/nardo/en/. Accessed on 13.07.2018, Nardò Technical Center, 2018.

[6] I. Abdić, L. Fridman, D. E. Brown, W. Angell, B. Reimer, E. Marchi, and B. Schuller. Detecting road surface wetness from audio: A deep learning approach. In *23rd International Conference on Pattern Recognition (ICPR)*, pages 3458–3463, Dec 2016.

[7] M. Acosta, S. Kanarachos, and M. Blundell. Road friction virtual sensing: A review of estimation techniques with emphasis on low excitation approaches. *MDPI Applied Sciences*, 7(12):1–47, 11 2017.

[8] C. Ahn. *Robust Estimation of Road Friction Coefficient for Vehicle Active Safety Systems*. doctoral dissertation, University of Michigan, Ann Arbor (USA), 2011.

[9] C. Ahn, H. Peng, and H. E. Tseng. Estimation of road friction for enhanced active safety systems: Algebraic approach. In *ACC'09*, pages 1104–1109, St. Louis, Missouri, USA, 2009.

[10] C. Ahn, H. Peng, and H. E. Tseng. Robust estimation of road frictional coefficient. *IEEE Transactions On Control Systems Technology*, 21:1–13, 2013.

[11] A. Albinsson, F. Bruzelius, B. Jacobson, T. Gustafsson, and M. Jonasson. Identification of tyre characteristics using active force excitation. In *the 24th of Dynamics*

of vehicles on roads and tracks (IAVSD) 2015. Graz, Austria, 17-21 August 2015, pages 501–510, 2015.

[12] A. Alessandri, M. Baglietto, and G. Battistelli. Moving-horizon state estimation for nonlinear discrete-time systems: New stability results and approximation schemes. *Automatica*, 44(7):1753 – 1765, 2008.

[13] J. Alonso, J.M. López, I. Pavón, M. Recuero, C. Asensio, G. Arcas, and A. Bravo. On-board wet road surface identification using tyre/road noise and support vector machines. *Applied Acoustics*, 76:407 – 415, 2014.

[14] M. Andersson et al. Road friction estimation. Technical report, Saab Automobile AB, 2007.

[15] A. M. Annaswamy, F. P. Skantze, and A. Loh. Adaptive control of continuous time systems with convex/concave parametrization. *Automatica*, 34(1):33 – 49, 1998.

[16] M. Arcak and P. Kokotović. Nonlinear observers: a circle criterion design and robustness analysis. *Automatica*, 37(12):1923 – 1930, 2001.

[17] J. Autioniemi, M. Autioniemi, et al. Intelligent road. Technical report, Lapland university of Applied Sciences, Luleå University of Technology, Finnish Meteorological institute, Finland, 2015.

[18] VBOX Automotive. https://www.vboxautomotive.co.uk/index.php/en/. Accessed on 04.02.2018., VBOX Automotive, 2018.

[19] T. Bachmann. *Literaturrecherche zum Reibwert zwischen Reifen und Fahrbahn*, volume 286. VDI Verlag, 1996.

[20] G. Baffet, A. Charara, and J. Stephant. Sideslip angle, lateral tire force and road friction estimation in simulations and experiments. In *2006 IEEE International Conference on Control Applications*, pages 903–908, Munich, Germany, Oct 2006.

[21] G. Bastin and M. R. Gevers. Stable adaptive observers for nonlinear time-varying systems. *IEEE Transactions on Automatic Control*, 33(7):650–658, Jul 1988.

[22] G. Besançon. Remarks on nonlinear adaptive observer design. *Systems & Control Letters*, 41(4):271 – 280, 2000.

[23] G. Besançon, Q.H. Zhang, and H. Hammouri. High-gain observer based state and parameter estimation in nonlinear systems. *IFAC Proceedings Volumes*, 37(13):327 – 332, 2004.

[24] M.C. Best, T.J. Gordon, and P.J. Dixon. An extended adaptive kalman filter for real-time state estimation of vehicle handling dynamics. *Vehicle System Dynamics*, 34(1):57–75, 2000.

[25] B. Boßdorf-Zimmer, L. Frömmig, R. Henze, and F. Kücükay. Real-time processing vehicle state estimation. In *Chassis Tech*, Munich, Germany, 2007.

[26] P. Boyraz and D. Dogan. Intelligent traction control in electric vehicles using an acoustic approach for online estimation of road-tire friction. In *2013 IEEE Intelligent Vehicles Symposium (IV)*, Gold Coast, Australia, 2013.

[27] B. Breuer, T. Bachmann, S. Ernesti, and J. Stöcker. Methods and Instruments for On-Board Measurement of Tyre/Road Friction. Sae technical paper 942470, Society of Automotive Engineers (SAE), 1994.

[28] C. Canudas de Wit, R. Horowitz, and P. Tsiotras. Model-based observers for tire/road contact friction prediction. In H. Nijmeijer and T.I. Fossen, editors, *New Directions in nonlinear observer design*, pages 23–42, London, 1999. Springer London.

[29] Z. Chen. Bayesian filtering: From kalman filters to particle filters, and beyond. *Statistics*, 182(1):1–69, 2003.

[30] O. Derbel, M. L. Cherif, and R. J. Landry. Driver behavior assessment based on loosely coupled gps/ins integration in harsh environment. In *2018 IEEE/ION Position, Location and Navigation Symposium (PLANS)*, pages 1362–1367, April 2018.

[31] N. Ding and S. Taheri. Application of recursive least square algorithm on estimation of vehicle sideslip angle and road friction. *Mathematical Problems in Engineering*, 2010, 2010.

[32] H. Dugoff, P. Fancher, and L. Segel. *Tire Performance Characteristics Affecting Vehicle Response to Steering and Braking Control Inputs: Final Report.* Highway Safety Research Institute, University of Michigan, 1969.

[33] U Eichhorn and J. Roth. Prediction and monitoring of tyre/road friction. In *24th Fisita Congress*, pages 67–74, London, England, 1992.

[34] X. Fan and M. Arcak. Observer design for systems with multivariable monotone nonlinearities. *Systems & Control Letters*, 50(4):319 – 330, 2003.

[35] Y. Fukada. Slip-angle estimation for vehicle stability control. *Vehicle System Dynamics*, 32(4-5):375–388, 1999.

[36] H. Grip. *Topics in State and Parameter Estimation for Nonlinear and Uncertain Systems*. doctoral dissertation, Norwegian University of Science and Technology, Trondheim (Norway), 2010.

[37] H. F. Grip, L. Imsland, T. A. Johansen, T. I. Fossen, J. C. Kalkkuhl, and A. Suissa. Nonlinear vehicle velocity observer with road-tire friction adaptation. In *Proceedings of the 45th IEEE Conference on Decision and Control*, pages 3603–3608, San Diego, CA, USA, Dec 2006.

[38] H. F. Grip, L. Imsland, T. A. Johansen, T. I. Fossen, J. C. Kalkkuhl, and A. Suissa. Nonlinear vehicle side-slip estimation with friction adaptation. *Automatica*, 44(3):611 – 622, 2008.

[39] H. F. Grip, L. Imsland, T. A. Johansen, J. C. Kalkkuhl, and A. Suissa. Estimation of road inclination and bank angle in automotive vehicles. In *2009 American Control Conference*, pages 426–432, St. Louis, Missouri, USA, June 2009.

[40] H. F. Grip, T. A. Johansen, L. Imsland, and G. Kaasa. Parameter estimation and compensation in systems with nonlinearly parameterized perturbations. *Automatica*, 46:19–28, 2010.

[41] H. F. Grip, A. Saberi, and T. A. Johansen. State and parameter estimation for linear systems with nonlinearly parameterized perturbations. In *Proceedings of the 48h IEEE Conference on Decision and Control (CDC) held jointly with 2009 28th Chinese Control Conference*, pages 8218–8225, Shanghai, China, Dec 2009.

[42] S. Gupta, J. Funke, and T. Lipp. Estimating road friction for autonomous vehicles. Technical report, Stanford University, 2011.

[43] F. Gustafsson. Slip-based tire-road friction estimation. *Automatica*, 33(6):1087 – 1099, 1997.

[44] A. Hac and M. Simpson. Estimation of vehicle side slip angle and yaw rate. In *SAE Technical Paper*. SAE International, 03 2000.

[45] J. Hahn, R. Rajamani, and L. Alexander. Gps-based real-time identification of tire-road friction coefficient. *IEEE Transactions on Control Systems Technology*, 10(3):331–343, May 2002.

[46] L. Hartikainen, F. Petry, and S. Westermann. Frequency-wise correlation of the

power spectral density of asphalt surface roughness and tire wet friction. *Wear*, 317(1):111 – 119, 2014.

[47] W. Hirschberg. Fahrzeugdynamik. Lecture notes, Graz University of Technology, Austria, 2014.

[48] F. Holzmann, M. Bellino, R. Siegwart, and H. Bubb. Predictive estimation of the road-tire friction coefficient. In *2006 IEEE International Conference on Control Applications*, pages 885–890, Munich, Germany, 2006.

[49] A. Howard and H. Seraji. Vision-based terrain characterization and traversability assessment. *Journal of Robotic Systems*, 18(10):577–587, 2001.

[50] T. Hsiao. Robust estimation and control of tire traction forces. *IEEE Transactions on Vehicular Technology*, 62(3):1378–1383, March 2013.

[51] J. Hsu. *Estimation and control of lateral tire forces using steering torque.* Doctoral dissertation, Stanford University, California (USA), 2007.

[52] Y.-J. Hsu, S. Laws, C. Gadda, and J. C. Gerdes. A method to estimate the friction coefficient and tire slip angle using steering torque. In *ASME 2006 International Mechanical Engineering Congress and Exposition*, pages 515–524, Chicago, Illinois, USA, 2006.

[53] W. Hwang and B. Song. Road condition monitoring system using tireroad friction estimation. In *AVEC'2000*, pages 437–442, Michigan, USA, Aug 2000.

[54] L. Imsland, H. F. Grip, T. A. Johansen, T. I. Fossen, J. C. Kalkkuhl, and A. Suissa. Nonlinear observer for vehicle velocity with friction and road bank angle adaptationvalidation and comparison with an extended kalman filter. In *SAE World Congress*, Detroit, USA, 2007.

[55] A. P. Ioannou and J Sun. Robust adaptive control. chapter 5. Prentice Hall, 1996.

[56] A. H. Jazwinski. *Stochastic processes and filtering theory.* Number 64 in Mathematics in science and engineering. Acad. Press, New York, USA, 1970.

[57] M. Jokela, M. Kutila, and L. Le. Road condition monitoring system based on a stereo camera. In *2009 IEEE 5th International Conference on Intelligent Computer Communication and Processing*, pages 423–428, Cluj-Napoca, Romania, 2009.

[58] S. J. Julier and J. K. Uhlmann. A new extension of the kalman filter to nonlinear systems. In *Proc. SPIE 3068, Signal Processing, Sensor Fusion, and Target Recognition VI*, pages 182–193, Orlando, FL, United States, 1997.

[59] S. J. Julier and J. K. Uhlmann. Unscented filtering and nonlinear estimation. *Proceedings of the IEEE*, 92(3):401–422, Mar 2004.

[60] D. Karagiannis and A. Astolfi. Nonlinear observer design using invariant manifolds and applications. In *Proceedings of the 44th IEEE Conference on Decision and Control*, pages 7775–7780, Seville, Spain, Dec 2005.

[61] D. Karagiannis, D. Carnevale, and A. Astolfi. Invariant manifold based reduced-order observer design for nonlinear systems. *IEEE Transactions on Automatic Control*, 53(11):2602–2614, Dec 2008.

[62] N. Kazantzis and C. Kravaris. Nonlinear observer design using lyapunov's auxiliary theorem. *Systems & Control Letters*, 34(5):241 – 247, 1998.

[63] J. Kennedy and R. C. Eberhart. Particle swarm optimization. In *Proceedings of the IEEE International Conference on Neural Networks*, pages 1942–1948, Perth, Western Australia, 1995.

[64] S Khaleghian, A Emami, and S Taheri. A technical survey on tire-road friction estimation. *Friction*, 5(2):123–146, Jun 2017.

[65] H. Khalil. High-gain observers in nonlinear feedback control. In H. Nijmeijer and T.I. Fossen, editors, *New Directions in nonlinear observer design*, pages 249–268. Springer London, London, 1999.

[66] H. Khalil. Nonlinear systems. chapter 4. Prentice Hall, Upper Saddle River, NJ, USA, 3nd edition, 2002.

[67] U. Kiencke and A. Daiß. Observation of lateral vehicle dynamics. *Control Engineering Practice*, 5(8):1145 – 1150, 1997.

[68] U. Kiencke and L. Nielsen. *Automotive Control Systems: For Engine, Driveline and Vehicle*. Springer-Verlag New York, Inc., Secaucus, NJ, USA, 1st edition, 2000.

[69] S. Koskinen. *Sensor Data Fusion Based Estimation of Tyre-Road Friction to Enhance Collision Avoidance*. Doctoral dissertation, Tampere University of Technology, Tampere (Finland), 2010.

[70] S. Koskinen and P. Peussa. FRICTI@N. Final Report - Public. Deliverable 13 for the european commission, Technical Research Centre (VTT), 2009. Tampere, Finland.

[71] C. Kravaris, V. Sotiropoulos, C. Georgiou, N. Kazantzis, M.Q. Xiao, and A. J.

Krener. Nonlinear observer design for state and disturbance estimation. *Systems & Control Letters*, 56(11):730 – 735, 2007.

[72] A. J. Krener and A. Isidori. Linearization by output injection and nonlinear observers. *Systems & Control Letters*, 3(1):47 – 52, 1983.

[73] A. J. Krener and W. Respondek. Nonlinear observers with linearizable error dynamics. *SIAM Journal on Control and Optimization*, 23(2):197–216, 1985.

[74] A. J. Krener and M.Q. Xiao. Erratum: Nonlinear observer design in the siegel domain. *SIAM Journal on Control and Optimization*, 43(1):377–378, 2004.

[75] M. Krstic. *Nonlinear and adaptive control design*. Wiley, New York, 1995.

[76] T. Kuno and H. Sugiura. Detection of road conditions with ccd cameras mounted on a vehicle. *Systems and Computers in Japan*, 30(14):88–99, 1999.

[77] J. Langheim, R. Divko, et al. Sensing of car environment at low speed driving. In *7th World Congress on Intelligent Transport Systems*, Torino, Italia, 2000.

[78] C. Lex. *Estimation of the Maximum Coefficient of Friction between Tire and Road Based on Vehicle State Measurements*. Doctoral dissertation, Graz University of Technology, Graz (Austria), 2015.

[79] W. Liang, H. Yu, R. McGee, M. Kuang, and J. Medanic. Vehicle pure yaw moment control using differential tire slip. In *Proceedings of the 2009 Conference on American Control Conference*, pages 3331–3336, St. Louis, Missouri, USA, 2009.

[80] C. Liu and H. Peng. Road friction coefficient estimation for vehicle path prediction. *Vehicle System Dynamics*, 25(sup1):413–425, 1996.

[81] A. Loria and E. Panteley. Uniformly exponential stability of linear time-varying systems: revisited. *Systems & Control Letters*, 47:13–24, 2002.

[82] C. Lundquist and T.B. schön. Recursive identification of cornering stiffness parameters for an enhanced single track model. Technical report, Linköpings Universitet, 2009.

[83] J. Masino, J. Pinay, M. Reischl, and F. Gauterin. Road surface prediction from acoustical measurements in the tire cavity using support vector machine. *Applied Acoustics*, 125:41 – 48, 2017.

[84] M. J. Matilainen and A. J. Tuononen. Tire friction potential estimation from measured tie rod forces. In *2011 IEEE Intelligent Vehicles Symposium (IV)*, pages 320–325, Baden-Baden, Germany, June 2011.

[85] T. Matsuda, S. Jo, h. Nishira, and Y. Deguchi. Instantaneous estimation of road friction based on front tire sat using kalman filter. *SAE Int. J. Passeng. Cars - Mech. Syst.*, 6:147–153, 2013.

[86] M. Mitschke and H. Wallentowitz. *Dynamik der Kraftfahrzeuge*. Springer, 2014.

[87] A. Mitterrutzner. Development and validation of a vehicle model for real time application on a steer-by-wire prototype. Master's thesis, Technical University Graz, Austria, 2015.

[88] F. Naets, S. van Aalst, B. Boulkroune, N. E. Ghouti, and W. Desmet. Design and experimental validation of a stable two-stage estimator for automotive sideslip angle and tire parameters. *IEEE Transactions on Vehicular Technology*, 66(11):9727–9742, Nov 2017.

[89] J. Nocedal and S. J. Wright. Numerical optimization, second edition. World Scientific, 2006.

[90] H. B. Pacejka. Tyre and vehicle dynamics. chapter 4. Butterworth-Heinemann, Oxford, second edition, 2006.

[91] G. Panahandeh, E. Ek, and N. Mohammadiha. Road friction estimation for connected vehicles using supervised machine learning. In *2017 IEEE Intelligent Vehicles Symposium (IV)*, pages 1262–1267, June 2017.

[92] F. Pedregosa, G. Varoquaux, A. Gramfort, et al. Scikit-learn: Machine learning in python. *The Journal of Machine Learning Research*, 12:2825–2830, November 2011.

[93] D. Piyabongkarn, R. Rajamani, J.A. Grogg, and J.Y. Lew. Development and experimental evaluation of a slip angle estimator for vehicle stability control. *IEEE Transactions on Control System Technology*, 17:78–88, 2009.

[94] A. Radke and Z. Gao. A survey of state and disturbance observers for practitioners. In *2006 American Control Conference*, pages 5183–5188, Minneapolis, MN,USA, 2006.

[95] S. Raghavan and J. K. Hedrick. Observer design for a class of nonlinear systems. *International Journal of Control*, 59(2):515–528, 1994.

[96] R. Rajamani. Observers for lipschitz nonlinear systems. *IEEE Transactions on Automatic Control*, 43(3):397–401, Mar 1998.

[97] R. Rajamani, N. Piyabongkarn, J. Lew, K. Yi, and G. Phanomchoeng. Tire-road friction-coefficient estimation. *IEEE Control Systems*, 30(4):54–69, Aug 2010.

[98] C. V. Rao, J. B. Rawlings, and D. Q. Mayne. Constrained state estimation for nonlinear discrete-time systems: stability and moving horizon approximations. *IEEE Transactions on Automatic Control*, 48(2):246–258, Feb 2003.

[99] L. R. Ray. Nonlinear tire force estimation and road friction identification: Simulation and experiments. *Automatica*, 33:1819–1833, 1997.

[100] G. Rill. Road vehicle dynamics, fundamentals and modeling. chapter 3. Taylor & Francis Group, Boca Raton, 2012.

[101] L. Shao, C. Jin, C. Lex, and A. Eichberger. Nonlinear adaptive observer for side slip angle and road friction estimation. In *2016 IEEE 55th Conference on Decision and Control (CDC)*, pages 6258–6265, Las Vegas, NV, USA, Dec 2016.

[102] L. Shao, C. Lex, A. Hackl, and A. Eichberger. Estimation of tire road friction during vehicle steering. In *13th International Symposium on Advanced Vehicle Control*, Munich, Germany, 2016.

[103] L. Shao, C. Lex, A. Hackl, and A. Eichberger. Road friction estimation using recursive total least squares. In *IEEE intelligent Vehicle Symposium*, Gothenberg, Sweden, 2016.

[104] C. Sierra, E. Tseng, A. Jain, and H. Peng. Cornering stiffness estimation based on vehicle lateral dynamics. *Vehicle System Dynamics*, 44(sup1):24–38, 2006.

[105] D. Simon. Optimal state estimation: Kalman, h infinity, and nonlinear approaches. chapter 15. Wiley-Interscience, 2006.

[106] K. Singh and S. Sivaramakrishnan. An adaptive tire model for enhanced vehicle control systems. *SAE Int. J. Passeng. Cars - Mech. Syst.*, 8(1):128–145, 2015.

[107] J. J. E. Slotine, J. K. Hedrick, and E. A. Misawa. On sliding observers for nonlinear systems. In *1986 American Control Conference*, pages 1794–1800, Seattle, WA, USA, June 1986.

[108] E. Sontag. *Mathematical Control Theory: Deterministic Finite Dimensional Systems (2Nd Ed.)*. Springer-Verlag, Berlin, Heidelberg, 1998.

[109] S. K. Spurgeon. Sliding mode observers: a survey. *International Journal of Systems Science*, 39(8):751–764, 2008.

[110] Ø. N. Stamnes, O. M. Aamo, and G. O. Kaasa. Adaptive redesign of nonlinear observers. *IEEE Transactions on Automatic Control*, 56(5):1152–1157, May 2011.

[111] R. Storn and K. Price. Differential evolution – a simple and efficient heuristic for global optimization over continuous spaces. *Journal of Global Optimization*, 11(4):341–359, Dec 1997.

[112] D. Sui and T. A. Johansen. Moving horizon estimation for tire-road friction during braking. In *2010 IEEE International Conference on Control Applications*, pages 1379–1384, Yokohama, Japan, Sept 2010.

[113] D. Sui and T. A. Johansen. Moving horizon observer with regularisation for detectable systems without persistence of excitation. *Int. J. Control*, 84:1041–1054, 2011.

[114] J. Svendenius. *Tire Modeling and Friction Estimation*. Doctoral dissertation, Department of Automatic Control, Lund Institute of Technology, Lund University, 2007.

[115] F. Takagi. An estimation method of the maximum tire road friction coefficient using an electric power assist steering. In *AVEC'10*, pages 13–15, Loughborough, UK, 2010.

[116] F. E. Thau. Observing the state of non-linear dynamic systems. *International Journal of Control*, 17(3):471–479, 1973.

[117] S. Torbrügge. Testing and understanding of tire-road interaction on wet roads. In *13th Symposium Reifen und Fahrwerk*, Vienna, 2015.

[118] A. Tuononen. On-board estimation of dynamic tyre forces from optically measured tyre carcass deflections. *International Journal of Heavy Vehicle Systems*, 16(3):362–378, 2009.

[119] A.J. Tuononen. Optical position detection to measure tyre carcass deflections. *Vehicle System Dynamics*, 46(6):471–481, 2008.

[120] I. Y. Tyukin, D. V. Prokhorov, and C. V. Leeuwen. Adaptation and parameter estimation in systems with unstable target dynamics and nonlinear parametrization. *IEEE Transactions on Automatic Control*, 52(9):1543–1559, Sept 2007.

[121] I. Y. Tyukin, E. Steur, H. Nijmeijer, and C. v. Leeuwen. Adaptive observers and parameter estimation for a class of systems nonlinear in the parameters. *Automatica*, 49(8):2409 – 2423, 2013.

[122] M. R. Uchanski. *Road Friction Estimation for Automobiles Using Digital Signal Processing Methods*. doctoral dissertation, University of California, Berkeley, Berkeley (USA), 2001.

[123] J. Villagra, B. ḋAndréa-Novel, M. Fliess, and H. Mounier. A diagnosis-based approach for tire road forces and maximum friction estimation. *Control Engineering Practice*, 19(2):174 – 184, 2011.

[124] C.G. Wallman and H. Aström. Friction measurement methods and the correlation between road friction and traffic safety. a literature review. Technical report, Swedish National Road and Transport Research Institute, Linköping, Sweden, 2001.

[125] J.M. Wang and R. G. Longoria. Coordinated vehicle dynamics control with control distribution. In *2006 American Control Conference*, pages 5348–5353, Minneapolis, MN, USA, June 2006.

[126] H. Winner and W. Wachenfeld. Absicherung automatischen fahrens. In *Proceedings of 6. Tagung Fahrerassistenz*, Munich, Germany, November 2013.

[127] K. Yi, K. Hedrick, and S. Lee. Estimation of tire-road friction using observer based identifiers. *Vehicle System Dynamics*, 31(4):233–261, 1999.

[128] M. Zanon, J. V. Frasch, and M. Diehl. Nonlinear moving horizon estimation for combined state and friction coefficient estimation in autonomous driving. In *2013 European Control Conference (ECC)*, pages 4130–4135, Zurich, Switzerland, July 2013.

[129] A. V. Zanten. Evolution of electronic control systems for improving the vehicle dynamic behavior. In *Proceedings of the International Symposium on Advanced Vehicle Control (AVEC)*, 2002.

[130] Q.H. Zhang and A. Clavel. Adaptive observer with exponential forgetting factor for linear time varying systems. In *Proceedings of the 40th IEEE Conference on Decision and Control*, pages 3886–3891, Orlando, Florida, USA, 2001.

A. Vehicle and tire parameters identification and validation

The vehicle utilized in this research is a racing car called Roding Roadster, see fig. A.1. Its parameters presented in Table A.1 (except for steering system parameters) and Table A.2 (except for tire self-aligning torque parameters of front tires) are identified and validated in a previous projects with the industrial partner thyssenkrupp presta [87]. Therein, the parameters of the lateral tire forces in front and rear axles are obtained by a test truck called "Mobile Tire Testing Laboratory" at the University of Applied Science Biel in Switzerland, see Fig. A.2. In this section, based on vehicle dynamics test in Nardò, the parameters of steering system and front tires' self-aligning torque will be identified and validated.

Figure A.1.: test racing car Roding Roadster. ©Foto: thyssenkrupp.

Table A.1.: Vehicle parameters (except for steering system parameters) identified by Andreas Mitterrutzner [87]

Parameters	**Symbol**	**Value**	**Unit**
Vehicle mass	m	1376	kg
Vehicle's moment of inertial (round z axle)	I_z	1900	kgm^2
Wheel base	l	2.495	m
Front track	w_f	1.62	m
Rear track	w_r	1.61	m
Distance of front axle to center of gravity	l_f	1.384	m
Distance of rear axle to center of gravity	l_r	1.111	m
Height of centre of gravity	h_g	0.415	m
Rotational inertial coefficient of steering system	J_s	1.1	kgm^2
Damping coefficient of steering system	k_s	26.9	Nm/(rad/s)
Mechanical trail	d_c	0.0339	m

Figure A.2.: test truck for lateral tire force parametrization [87].

Table A.2.: Tire parameters of Roding Roadster, front tires: Michelin 225/40/ZR18, rear tires: Michelin 265/35/ZR18. The identification and validation of the lateral tire force parameters for front and rear tires are conducted in [87] while the parameters of self-aligning torque in front tires are carried out in this study.

Parameters	**Symbol**	**Front tires**	**Rear tires**
Nominal tire load	$F_{z,nom}$	2500 N	3000 N
Extra tire load	$F_{z,2nom}$	4858 N	4926 N
Peak force	$Y_{max}(F_{z,nom}, \mu_0)$	3380 N	4300 N
Nominal tire-road friction coefficient	μ_0	1	1
Peak force	$Y_{max}(F_{z,2nom}, \mu_0)$	5700 N	6110 N
Initial stiffness	$d_{Y0}(F_{z,nom})$	55200 N/rad	73950 N/rad
Initial stiffness	$d_{Y0}(F_{z,2nom})$	96000 N/rad	107900 N/rad
Saturation force	$Y_{inf}(F_{z,nom}, \mu_0)$	2600 N	2900 N
Saturation force	$Y_{inf}(F_{z,2nom}, \mu_0)$	4000 N	4100 N
Initial normalized pneumatic trail	$(\frac{n}{L})_0(F_{z,nom})$	0.3355	no data
Initial normalized pneumatic trail	$(\frac{n}{L})_0(F_{z,2nom})$	0.3627	no data
Overshot wheel slip angle	$s_y^0(F_{z,nom}, \mu_0)$	0.1219 rad	no data
Overshot wheel wheel angle	$s_y^0(F_{z,2nom}, \mu_0)$	0.128 rad	no data
Saturated wheel slip angle	$s_y^E(F_{z,nom}, \mu_0)$	0.25 rad	no data
Saturated wheel slip angle	$s_y^E(F_{z,2nom}, \mu_0)$	0.225 rad	no data
Vertical stiffness	c_z	295000 N/m	no data
Unloaded tire radius	r_0	0.3186 m	no data

A.1. Tire self-aligning torque, steering system parameters identification and validation

Three steps are taken to identify and validate the tire self-aligning torque and steering system parameters based on the steering system shown in Fig. A.3 and its state equations[1] in (A.1).

$$\begin{aligned} J_s\ddot{\delta} + k_s\dot{\delta} &= \tau_g(t) - \tau_{zf}(t), \\ \tau_g(t) &= F_l(t)L_l(\delta) - F_r(t)L_r(\delta), \\ \tau_{zf}(t) &= M_{zfl} + M_{zfr} + (F_{yfl} + F_{yfr})d_c, \end{aligned} \tag{A.1}$$

where J_s is the rotational inertia coefficient, k_s the damping coefficient, δ the front wheel steering angle, $\tau_{zf}(t)$ the total aligning torque, $\tau_g(t)$ the aligning torque caused by $F_l(t)$ and $F_r(t)$ which are the tie rod forces on the left and right sides measured by strain gauge sensors, $L_l(\delta)$ and $L_r(\delta)$ are the vertical distances between the tie rod to the kingpin separately which vary with steering angle and a lookup table is already pre-created, M_{zfl} and M_{zfr} the front left and right tire self-aligning torque separately, F_{yfl} the front left tire lateral force, F_{yfr} the front right tire lateral force, d_c the mechanical trail of front tires which is assumed to be the same for both front left and right tires and is measured in advance. It has to be mentioned that the contribution of jacking torque coefficient here can be omitted since the jacking torque caused by the vertical load on the right and left wheels are mutually cancelled [85].

The three steps are as follow:

1. A steady state maneuver — constant circular radius driving (30 m) with slowly increasing longitudinal velocity — is conducted to identify the parameters of front tires' self-aligning torque. This will work because the dynamics of steering system is not activated under steady state maneuver;
2. After obtaining the parameters of front tires' self-aligning torque, several dynamic maneuvers are carried out to parametrize the steering system;
3. Finally, several dynamic maneuvers are implemented to validate the parametrization results performed in the above two steps.

The maneuvers for identifying and validating the tire self-aligning torque and steering system parameters are listed in Table A.3.

[1] These state equations or similar ones are utilized by many other work, such as in [10].

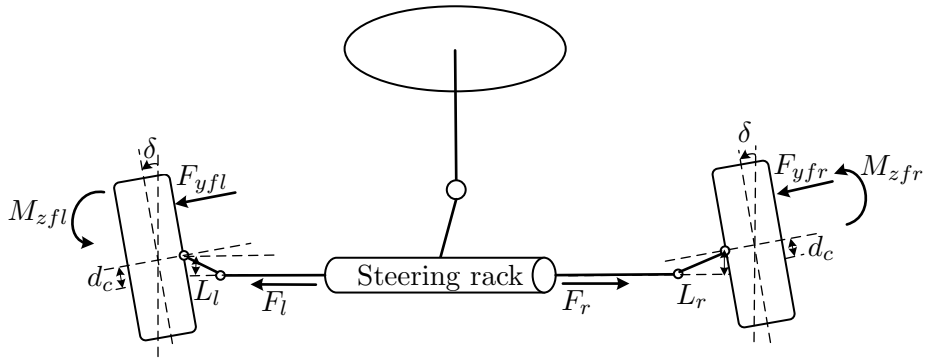

Figure A.3.: Steering system

Table A.3.: list of maneuvers for identifying and validating self-aligning torque and steering system parameters.

Maneuver Number	**Description**	**Purpose**	**Road Condition**
Cr-30m-lft-MD-001	steady state steer	tire self-aligning torque parametrization	nominal μ_0
Oc-90-06g-02	sinusoidal steer	steering system parametrization	nominal μ_0
StepRight-70-04g-01	step steer		
OC-50-04g-02	sinusoidal steer	model validation	nominal μ_0
StepLeft-70-04g-01	step steer		

A.1.1. Tire self-aligning torque parameters identification

Firstly a constant circular radius (30 m) maneuver is utilized with slowly increasing longitudinal velocity shown in Fig. A.4 to identify the tire self-aligning torque parameters. With this steady state maneuver, the steering system in (A.1) can be simplified into

$$\begin{aligned} 0 &= \tau_g(t) - \tau_{zf}(t), \\ \tau_g(t) &= F_l(t) * L_l(\delta) - F_r(t) * Lr(\delta), \\ \tau_{zf}(t) &= M_{zfl} + M_{zfr} + (F_{yfl} + F_{yfr})d_c. \end{aligned} \tag{A.2}$$

Here, $F_l(t)$ and $F_r(t)$ can be directly measured and a table of $L_l(\delta)$ and $L_r(\delta)$ varying

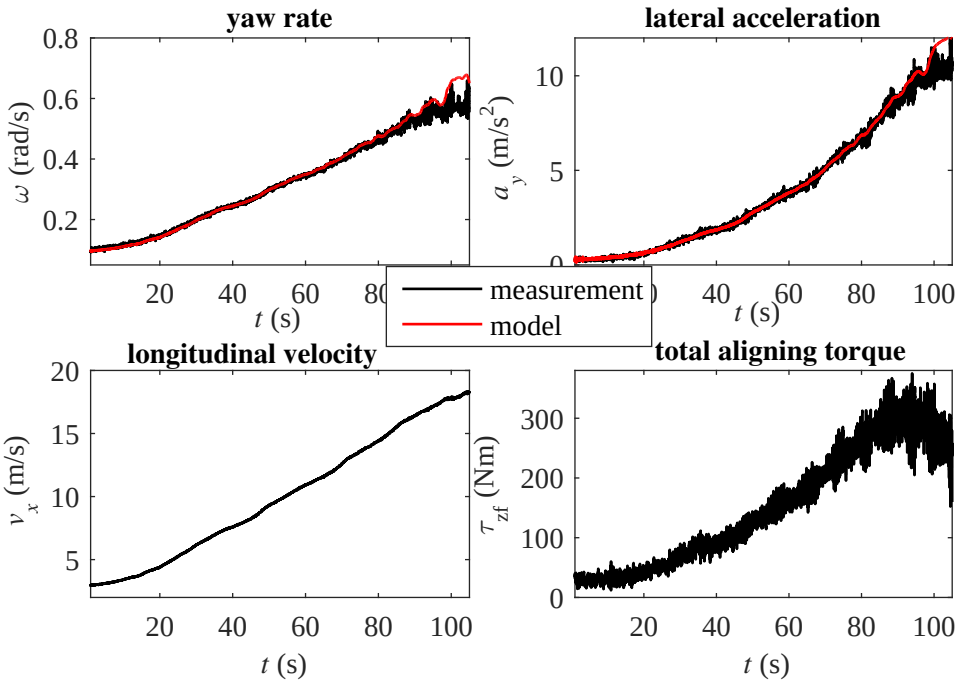

Figure A.4.: Vehicle states for self-aligning torque parametrization with a constant radius circular driving maneuver. Maneuver Number: Cr-30m-lft-MD-001

with the wheel steering angle is used, thus $\tau_g(t)$ can be directly calculated. Based on (3.1a) and $F_{yr} = ma_y - F_{yf}\cos(\delta)$, $F_{yf}(= F_{yfl} + F_{yfr})$ can be obtained with

$$F_{yf} = \frac{l_r m a_y + I_z \dot{\omega}}{(l_f + l_r)\cos(\delta)}, \tag{A.3}$$

where l_f and l_r are the distance between front and rear axle to vehicle center of gravity (CoG) , m is the vehicle mass, a_y the lateral acceleration, I_z the vehicle inertial moment, ω the yaw rate, F_{yr} the rear axle tire lateral force.

After obtaining F_{yf}, front axle tire self-aligning torque ($M_{zf} = M_{zfl} + M_{zfr}$) is acquired based on eq.(A.2). Subsequently, front left and right tire self-aligning torque is calculated

as follows:

$$\begin{aligned} M_{zfl} &= \frac{F_{zfl}^{3/2}}{F_{zfl}^{3/2}+F_{zfr}^{3/2}} M_{zf}, \\ M_{zfr} &= \frac{F_{zfr}^{3/2}}{F_{zfl}^{3/2}+F_{zfr}^{3/2}} M_{zf}, \end{aligned} \tag{A.4}$$

where F_{zfl} and F_{zfr} are the front left and front right tires' normal force calculated based on (3.5) and (3.6a).

In the following, why the front left and right tire self-aligning torque can be calculated with (A.4) will be explained. In the front axle, for the same tire slip angle and tire-road friction coefficient, M_{zfl} and M_{zfr} can be expressed as

$$\begin{aligned} M_{zfl} &= F_{yfl}(\alpha_f, \mu_{max}, F_{zfl}) \cdot L_l(F_{zfl}) \cdot (\frac{n}{L})_l(\alpha_f, \mu_{max}, F_{zfl}), \\ M_{zfr} &= F_{yfr}(\alpha_f, \mu_{max}, F_{zfr}) \cdot L_r(F_{zfr}) \cdot (\frac{n}{L})_r(\alpha_f, \mu_{max}, F_{zfr}), \end{aligned} \tag{A.5}$$

with following assumptions

$$\begin{aligned} \frac{F_{yfl}(\alpha_f, \mu_{max}, F_{zfl})}{F_{yfr}(\alpha_f, \mu_{max}, F_{zfr})} &\approx \frac{F_{zfl}}{F_{zfr}}, \\ \frac{L_l(F_{yfl})}{L_r(F_{yfr})} &= \frac{F_{zfl}^{\frac{1}{2}}}{F_{zfr}^{\frac{1}{2}}}, \\ \frac{(\frac{n}{L})_l(\alpha_f, \mu_{max}, F_{zfl})}{(\frac{n}{L})_r(\alpha_f, \mu_{max}, F_{zfr})} &\approx 1, \end{aligned} \tag{A.6}$$

It has to be mentioned that though normal force will influence $(\frac{n}{L})_l(\alpha_f, \mu_{max}, F_{zfl})$ and $(\frac{n}{L})_r(\alpha_f, \mu_{max}, F_{zfr})$, the affect is actually very small [100]. Therefore, the ratio of front left to front right tire self-aligning torque can be represented as

$$\frac{M_{zfl}(\alpha_f, \mu_{max}, F_{zfl})}{M_{zfr}(\alpha_f, \mu_{max}, F_{zfr})} \approx \frac{F_{zfl}^{3/2}}{F_{zfr}^{3/2}}, \tag{A.7}$$

which deduces (A.4).

After obtaining M_{zfl} and M_{zfr}, they are normalized to the corresponding values under nominal normal force (2500 N) and extra normal force 4858 N based on (A.7), separately. Finally, combined with measured tire slip angle, tire self-aligning torque of the front tires

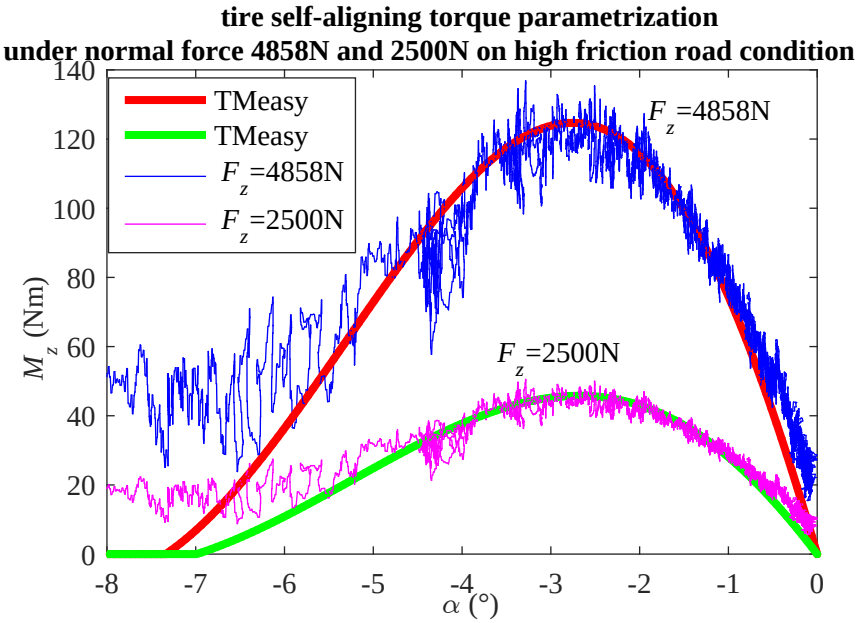

Figure A.5.: Tire self-aligning torque parametrization for normal forces 4858 N and 2500 N on nominal tire-road condition $\mu_0 = 1$ with a constant radius (30 m) circular driving maneuver.

is parametrized, which is shown in Fig.A.5. The corresponding parameters can refer to Table.A.2.

A.1.2. Steering system parameters identification

After parametrizing the tire self-aligning torque, several dynamic maneuvers (a sinusoidal and a step steer maneuver) listed in Table. A.3 are performed to identify steering system parameters. At first, the dynamic steering system in (A.1) can be re-formulated as

$$A(t)\Theta = y(t), \tag{A.8}$$

with

$$\begin{aligned} A(t) &= (\ddot{\delta}, \dot{\delta}), \\ \Theta &= (J_s, k_s)^T, \\ y(t) &= \big(F_l(t) * L_l(\delta) - F_r(t) * L_r(\delta)\big) - \big(F_{yf}(\alpha_f, \mu_0) * d_c + M_{zf}(\alpha_f, \mu_0)\big), \end{aligned}$$

where $F_{yf}(\alpha_f, \mu_0)$ and $M_{zf}(\alpha_f, \mu_0)$ are calculated based on parametrized TMsimple ($F_{yf}(\alpha_f, \mu_0)$) and TMeasy ($M_{zf}(\alpha_f, \mu_0)$) with measured α_f under nominal μ_0.

Therefore, with least squares method, these two parameters are obtained which are $J_s = 1.1$ kg.m^2 and $k_s = 26.9$ Nm/(rad/s).

A.1.3. Self-aligning torque and steering system validation

After identification of tire self-aligning torque and steering system parameters, several maneuvers are performed to validate the parametrization quality. In Fig.A.6 and Fig.A.7, it can be noticed that the total aligning torques (τ_{zf}), yaw rate as well as lateral acceleration from vehicle model and measured values conform to each other well, which demonstrates accurate parametrization of tire self-aligning torque and steering system, and again shows the well parametrization of vehicle and tire lateral force model from [87].

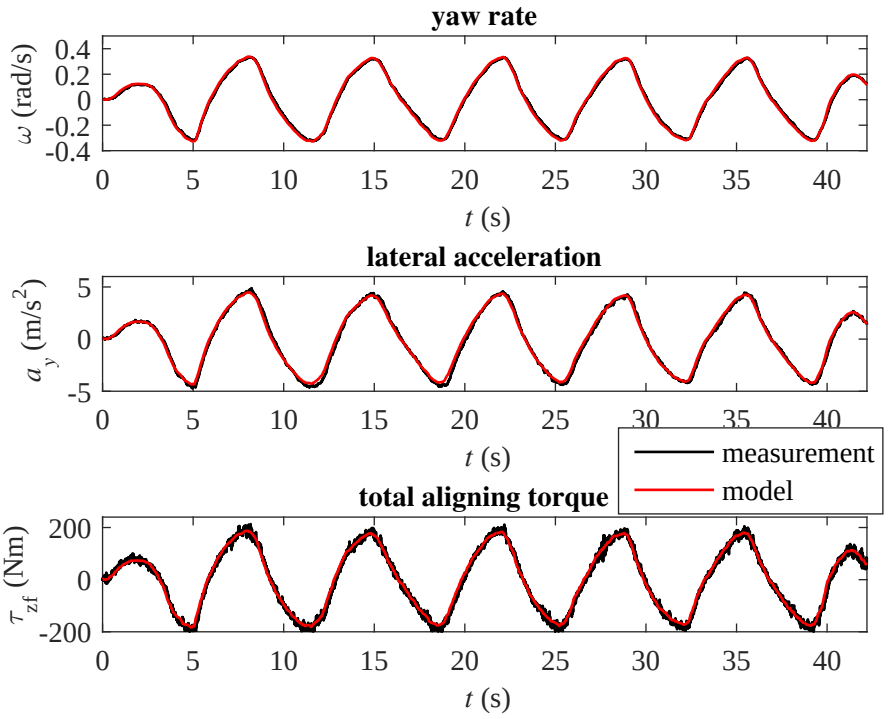

Figure A.6.: Validation of tire parameters and steering system with sinusoidal maneuver.

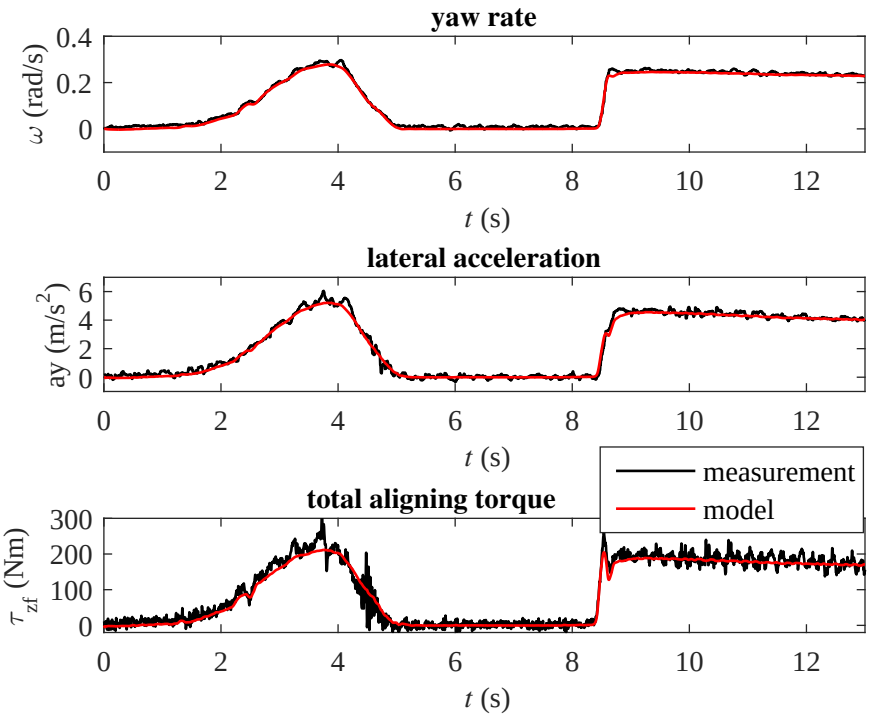

Figure A.7.: Validation of tire parameters and steering system with step steer maneuver.

B. Vehicle model transformation

According to (4.3), there are

$$\dot{\omega} = \frac{lF_{yf}\cos\delta}{I_z} - \frac{l_r m a_y}{I_z}, \tag{B.1}$$

$$\dot{\alpha}_f = (a-b)(cos\delta)F_{yf} + bma_y - \omega - \dot{\delta}, \tag{B.2}$$

where $a = \frac{1}{mv_x} + \frac{l_f^2}{I_z v_x}$, $b = \frac{1}{mv_x} - \frac{l_f l_r}{I_z v_x}$. Then, by introducing (4.5),

$$F_{yf} = \frac{\tau_{zf}}{g_f(x_f) + f_f(x_f)d_c} \cdot f_f(x_f) \tag{B.3}$$

is deduced. Subsequently, F_{yf} is reformulated as

$$F_{yf} = -|\tau_{zf}|\text{sign}(x_f) \cdot \big(\frac{f_f(x_f)}{g_f(x_f) + f_f(x_f)d_c} - m_v\big) + \tau_{zf} m_v, \tag{B.4}$$

where $m_v = \lim_{x_f \to 0} \frac{f_f(x_f)}{g_f(x_f)+f_f(x_f)d_c}$ and $|\tau_{zf}|\text{sign}(x_f) = -\tau_{zf}$, such that a monotonic continuous term with respect to x_f in F_{yf} is generated, which is $-|\tau_{zf}|\text{sign}(x_f)\cdot\big(\frac{f_f(x_f)}{g_f(x_f)+f_f(x_f)d_c} - m_v\big)$.

Finally, replacing the F_{yf} in B.1 with B.4 and dividing the both side of B.2 by $\mu_{\max}$,

$$\dot{\omega} = \frac{l\tau_{zf}m_v\cos(\delta) - l_r m a_y}{I_z} + \frac{-|\tau_{zf}|l\cos(\delta)}{I_z}\big(\frac{f_f(x_f)}{g_f(x_f) + f_f(x_f)d_c} - m_v\big)\text{sign}(x_f)$$

$$\dot{x}_f = (a-b)(cos\delta)f_f(x_f) + (bma_y - \omega - \dot{\delta})\frac{1}{\mu_{\max}}$$

are obtained.

C. Some notes for method II

C.1. Parameter projection

Let the set of possible parameters be defined by $\Pi := \{\hat{\theta} \in \mathbb{R}^r | P(\hat{\theta}) \leq 0\}$, where $P : \mathbb{R}^r \to \mathbb{R}$ is a smooth, convex function. Let Π^0 denote the interior of Π, and let Π^ϵ be defined by $\Pi^\epsilon = \{P(\hat{\theta}) \leq \epsilon\}$, where ϵ is a small positive value, making Π^ϵ a slightly larger superset of Π. Consider the update function $u_{\hat{\theta}}(t, \hat{x}, \hat{\varphi}_2, \hat{\theta}) = \text{Proj}(\tau(t, \hat{x}, \hat{\varphi}_2, \hat{\theta})) = \rho(t, \hat{x}, \hat{\varphi}_2, \hat{\theta})\tau(t, \hat{x}, \hat{\varphi}_2, \hat{\theta})$, with $\rho(t, \hat{x}, \hat{\varphi}_2, \hat{\theta})$ given by

- $\rho(t, \hat{x}, \hat{\varphi}_2, \hat{\theta}) = I$ if $\hat{\theta} \in \Pi^0$ or $\nabla_{\hat{\theta}} P^T \tau(t, \hat{x}, \hat{\varphi}_2, \hat{\theta}) \leq 0$,
- $\rho(t, \hat{x}, \hat{\varphi}_2, \hat{\theta}) = \big(I - c(\hat{\theta})\Gamma_2 \nabla_{\hat{\theta}} P \nabla_{\hat{\theta}} P^T / (\nabla_{\hat{\theta}} P^T \Gamma_2 \nabla_{\hat{\theta}} P)\big)$
  if $\hat{\theta} \in \Pi^\epsilon \backslash \Pi^0$ and $\nabla_{\hat{\theta}} P^T \tau(t, \hat{x}, \hat{\varphi}_2, \hat{\theta}) > 0$,

where $c(\hat{\theta}) = \min\{1, P(\hat{\theta})/\epsilon\}$, $\nabla_{\hat{\theta}} P = \frac{\partial P(\hat{\theta})}{\partial \hat{\theta}}$, Γ_2 is the symmetric positive-definite matrix corresponding to the gain matrix in the update law.

C.2. Details in error dynamics

The deduction process of error dynamics for designed observer is as follows:

$$
\begin{aligned}
\dot{\tilde{\varphi}}_1 &= \dot{\varphi}_1 - \dot{\hat{\varphi}}_1 \\
&= B_1(t,\omega)\frac{\partial g_1(\omega,x)}{\partial x}\big(f_2(t,x) + B_2(t,x)g_2(x,\theta)\big) + \frac{\partial B_1(t,\omega)}{\partial t}g_1(\omega,x) + \frac{\partial (B_1(t,\omega)g_1(\omega,x))}{\partial \omega}\dot{\omega} \\
&\quad + K_{\varphi_1}(f_1(t,\omega) + \hat{\varphi}_1) + B_1(t,\omega)\frac{\partial g_1(\omega,\hat{x})}{\partial \hat{x}}\big(u_\tau - f_2(t,\hat{x}) - B_2(t,\hat{x})g_2(\hat{x},\hat{\theta})\big) \\
&\quad - K_{\varphi_1}\dot{\omega} - B_1(t,\omega)\frac{\partial g_1(\omega,\hat{x})}{\partial \hat{x}}u_\tau - \frac{\partial B_1(t,\omega)}{\partial t}g_1(\omega,\hat{x}) - \frac{\partial (B_1(t,\omega)g_1(\omega,\hat{x}))}{\partial \omega}\dot{\omega} \\
&= -K_{\varphi_1}\tilde{\varphi}_1 + d_1(t,\omega,\theta,\tilde{x}) + d_3(t,\omega,\hat{x},\tilde{\theta}) \\
\dot{\tilde{x}} &= \dot{x} - \dot{\hat{x}} \\
&= f_2(t,x) + B_2(t,x)g_2(x,\theta) - u_\tau(t,\omega,\hat{x},\varphi_1,\theta) + d_4(t,\omega,\hat{x},\tilde{\varphi}_1,\theta) + d_5(t,\omega,\hat{x},\hat{\varphi}_1,\tilde{\theta})
\end{aligned}
$$

$$
\begin{aligned}
\dot{\tilde{\varphi}}_2 &= \dot{\varphi}_2 - \dot{\hat{\varphi}}_2 \\
&= \frac{\partial B_2(t,x)}{\partial t} g_2(x,\theta) + \frac{\partial B_2(t,x) g_2(x,\theta)}{\partial x}\dot{x} + K_{\varphi_2}(f_2(t,\hat{x}) + \hat{\varphi}_2) \\
&\quad + B_2(t,\hat{x})\frac{\partial g_2(\hat{x},\hat{\theta})}{\partial \hat{\theta}} u_\theta(t,\hat{x},\hat{\varphi}_2,\hat{\theta}) - K_{\varphi_2}\dot{x} - \frac{\partial B_2(t,x)}{\partial t} g_2(x,\hat{\theta}) \\
&\quad - \frac{\partial B_2(t,x) g_2(x,\hat{\theta})}{\partial x}\dot{x} - B_2(t,x)\frac{\partial g_2(x,\hat{\theta})}{\partial \hat{\theta}} u_\theta(t,\hat{x},\hat{\varphi}_2,\hat{\theta}) \\
&= -K_{\varphi_2}\tilde{\varphi}_2 + d_2(t,x,\tilde{\theta}) + d_6(t,\tilde{x},\hat{\varphi}_2,\hat{\theta}) \\
\dot{\tilde{\theta}} &= \dot{\theta} - \dot{\hat{\theta}} \\
&= -u_\theta(t,x,\varphi_2,\hat{\theta}) + d_7(t,x,\tilde{\varphi}_2,\hat{\theta}) + d_8(t,\tilde{x},\bar{\varphi}_2,\hat{x},\hat{\theta}),
\end{aligned}
$$

where

$$
\begin{aligned}
d_1(t,\omega,\theta,\tilde{x}) &= B_1(t,\omega)\Big(\frac{\partial g_1(\omega,x)}{\partial x} f_2(t,x) - \frac{\partial g_1(\omega,\hat{x})}{\partial \hat{x}} f_2(t,\hat{x})\Big) \\
&\quad + \frac{\partial B_1(t,\omega)}{\partial t}\Big(g_1(\omega,x) - g_1(\omega,\hat{x})\Big) \\
&\quad + B_1\Big(\frac{\partial g_1(\omega,x)}{\partial x} B_2(t,x) g_2(x,\theta) - \frac{\partial g_1(\omega,\hat{x})}{\partial \hat{x}} B_2(t,\hat{x}) g_2(\hat{x},\theta)\Big) \\
&\quad + \Big(\frac{\partial (B_1(t,\omega) g_1(\omega,x))}{\partial \omega} - \frac{\partial (B_1(t,\omega) g_1(\omega,\hat{x}))}{\partial \omega}\Big)\dot{\omega} \\
d_2(t,x,\tilde{\theta}) &= \Big(\frac{\partial B_2(t,x) g_2(x,\theta)}{\partial x} - \frac{\partial B_2(t,x) g_2(x,\hat{\theta})}{\partial x}\Big)\dot{x} \\
&\quad + \frac{\partial B_2(t,x)}{\partial t}(g_2(x,\theta) - g_2(x,\hat{\theta})) \\
d_3(t,\omega,\hat{x},\tilde{\theta}) &= B_1(t,\omega)\frac{\partial g_1(\omega,\hat{x})}{\partial \hat{x}} B_2(t,\hat{x})(g_2(\hat{x},\theta) - g_2(\hat{x},\hat{\theta})) \\
d_4(t,\omega,\hat{x},\tilde{\varphi}_1,\theta) &= u_\tau(t,\omega,\hat{x},\varphi_1,\theta) - u_\tau(t,\omega,\hat{x},\hat{\varphi}_1,\theta) \\
d_5(t,\omega,\hat{x},\hat{\varphi}_1,\tilde{\theta}) &= u_\tau(t,\omega,\hat{x},\hat{\varphi}_1,\theta) - u_\tau(t,\omega,\hat{x},\hat{\varphi}_1,\hat{\theta}) \\
d_6(t,\tilde{x},\hat{\varphi}_2,\hat{\theta}) &= -K_{\varphi_2}\big(K_{\varphi_2}x - K_{\varphi_2}\hat{x} + f_2(t,x) - f_2(t,\hat{x})\big) \\
&\quad + K_{\varphi_2}\big(B_2(t,\hat{x}) g_2(\hat{x},\hat{\theta}) - B_2(t,x) g_2(x,\hat{\theta})\big) \\
&\quad + \Big(B_2(t,\hat{x})\frac{\partial g_2(\hat{x},\hat{\theta})}{\partial \hat{\theta}} - B_2(t,x)\frac{\partial g_2(x,\hat{\theta})}{\partial \hat{\theta}}\Big) u_\theta(t,\hat{x},\hat{\varphi}_2,\hat{\theta}) \\
d_7(t,x,\tilde{\varphi}_2,\hat{\theta}) &= u_\theta(t,x,\varphi_2,\hat{\theta}) - u_\theta(t,x,\bar{\varphi}_2,\hat{\theta}) \\
d_8(t,\tilde{x},\bar{\varphi}_2,\hat{x},\hat{\theta}) &= u_\theta(t,x,\bar{\varphi}_2,\hat{\theta}) - u_\theta(t,\hat{x},\bar{\varphi}_2,\hat{\theta}) + u_\theta(t,\hat{x},\bar{\varphi}_2,\hat{\theta}) - u_\theta(t,\hat{x},\hat{\varphi}_2,\hat{\theta})
\end{aligned}
$$

C.3. Proof of Proposition 4.4.1

Choose Lyapunov function

$$V_x(t,\tilde{x}) \;=\; \frac{1}{2}\tilde{x}^T\Gamma_1^{-1}\tilde{x},$$

with which

$$\frac{1}{2}\lambda_{\min}(\Gamma_1^{-1})||\tilde{x}||^2 \;\leq\; V_x(t,\tilde{x}) \;\leq\; \frac{1}{2}\lambda_{\max}(\Gamma_1^{-1})||\tilde{x}||^2$$

is deduced, indicating $V_x(t,\tilde{x})$ being radially unbounded. Then there is

$$\begin{aligned}
\dot{V}_x(t,\tilde{x}) &= \frac{1}{2}\tilde{x}^T\Gamma_1^{-1}\dot{\tilde{x}} + \frac{1}{2}\dot{\tilde{x}}^T\Gamma_1^{-1}\tilde{x} \\
&\leq -\frac{k_1}{2}\Big(\big(g_1(\omega,x)-g_1(\omega,\hat{x})\big)^T B_1^T M_1^T\tilde{x} + \tilde{x}^T M_1 B_1\big(g_1(\omega,x)-g_1(\omega,\hat{x})\big) \\
&\quad -\tilde{x}^T\frac{1}{k_1}\Gamma_1^{-1}\big(f_2(t,x)-f_2(t,\hat{x})+B_2(t,x)g_2(x,\theta)-B_2(t,\hat{x})g_2(\hat{x},\theta)\big) \\
&\quad -\big(f_2(t,x)-f_2(t,\hat{x})+B_2(t,x)g_2(x,\theta)-B_2(t,\hat{x})g_2(\hat{x},\theta)\big)^T\frac{1}{k_1}\Gamma_1^{-1}\tilde{x}\Big) \\
&\quad +\Delta(\tilde{x},\tilde{\varphi}_1,\tilde{\theta}) \\
&\leq -k_1 p_1^*||\tilde{x}||^2 + (l_4(\Gamma_1,k_1)||\tilde{\varphi}_1||||\tilde{x}|| + l_5||\tilde{\theta}||||\tilde{x}||)||\Gamma_1^{-1}|| \\
&= -\alpha_1||\tilde{x}||^2 + \beta_2(\tilde{\varphi}_1,\tilde{\theta})||\tilde{x}||
\end{aligned}$$

where $\Delta(\tilde{x},\tilde{\varphi}_1,\tilde{\theta}) = \big(d_4(t,\omega,\hat{x},\tilde{\varphi}_1,\theta)+d_5(t,\omega,\hat{x},\hat{\varphi}_1,\tilde{\theta})\big)^T\Gamma_1^{-1}\tilde{x}$, $\alpha_1 = k_1 p_1^*$, which is a positive scalar, $\beta_2(\tilde{\varphi}_1,\tilde{\theta}) = ||\Gamma_1^{-1}||\big(l_4(\Gamma_1,k_1)||\tilde{\varphi}_1|| + l_5||\tilde{\theta}||\big)$.

To derive the forementioned inequations, a projection property in Lemma E.1 of [75] is applied, which is

$$\begin{aligned}
&-\tilde{x}^T\Gamma_1^{-1}u_\tau(t,\omega,\hat{x},\varphi_1,\theta) \\
=\;& -\tilde{x}^T\Gamma_1^{-1}\,\mathrm{Proj}\Big(k_1\Gamma_1 M_1\big(\varphi_1 - B_1(t,\omega)g_1(\omega,\hat{x})\big) + f_2(t,\hat{x}) + B_2(t,\hat{x})g_2(\hat{x},\theta)\Big) \\
\leq\;& -\tilde{x}\Gamma_1^{-1}\Big(k_1\Gamma_1 M_1\big(\varphi_1 - B_1(t,\omega)g_1(\omega,\hat{x})\big) + f_2(t,\hat{x}) + B_2(t,\hat{x})g_2(\hat{x},\theta)\Big)
\end{aligned}$$

Besides, the following inequality

$$\begin{aligned}
& \tilde{x}^T M_1 B_1 \big(g_1(\omega, x) - g_1(\omega, \hat{x})\big) + \big(g_1(\omega, x) - g_1(\omega, \hat{x})\big)^T B_1^T M_1^T \tilde{x} \\
& -\tilde{x}^T \frac{1}{k_1} \Gamma_1^{-1} \Big(f_2(x) - f_2(\hat{x}) + B_2(x) g_2(x, \theta) - B_2(\hat{x}) g_2(\hat{x}, \theta) \Big) \\
& -\Big(f_2(x) - f_2(\hat{x}) + B_2(x) g_2(x, \theta) - B_2(\hat{x}) g_2(\hat{x}, \theta) \Big)^T \frac{1}{k_1} \Gamma_1^{-1} \tilde{x} \\
= & \int_0^1 \tilde{x}^T \Big(M_1 B_1 \frac{\partial g_1(\omega, \hat{x} + p\tilde{x})}{x} + \frac{\partial g_1^T(\omega, \hat{x} + p\tilde{x})}{x} B_1^T M_1^T \\
& -\frac{1}{k_1} \Gamma_1^{-1} \frac{\partial (f_2(t, \hat{x} + p\tilde{x}) + B_2(t, \hat{x} + p\tilde{x}) g_2(\hat{x} + p\tilde{x}, \theta))}{\partial x} \\
& -\frac{1}{k_1} \frac{\partial (f_2(t, \hat{x} + p\tilde{x}) + B_2(t, \hat{x} + p\tilde{x}) g_2(\hat{x} + p\tilde{x}, \theta))^T}{\partial x} \Gamma_1^{-1} \Big) \tilde{x} dp \\
\geq & \int_0^1 \tilde{x}^T 2 p_1(t, \omega) \tilde{x} dp \quad = \quad 2\tilde{x}^T p_1(t, \omega) \tilde{x} \quad \geq \quad 2 p_1^* \tilde{x}^T \tilde{x},
\end{aligned}$$

from [89] is also applied.

D. Property for adaptive resolution in method III

For the nonlinear single track model, there is following dynamic equation

$$\dot{\alpha}_f = (a-b)(cos\delta)F_{yf}(\alpha_f, \mu_{\max}) + bma_y - \omega - \dot{\delta}, \tag{D.1}$$

which is already shown in (4.3b) by assuming a constant longitudinal velocity, where $a = \frac{1}{mv_x} + \frac{l_f^2}{I_z v_x}$, $b = \frac{1}{mv_x} - \frac{l_f l_r}{I_z v_x}$. Now, use $C_f\alpha_{f,l}$ to replace $F_{yf}(\alpha_f, \mu_{\max})$, a linear observer with $\alpha_{f,l}$ as the state is obtained:

$$\dot{\alpha}_{f,l} = (a-b)(cos\delta)C_f\alpha_{f,l} + bma_y - \omega - \dot{\delta}, \tag{D.2}$$

where $(a-b)(cos\delta) > 0$. Based on (D.1) and (D.2), the following property is proved:

Property D.0.1.

$$\begin{aligned} \beta_{cl} &\leq \beta \quad \textit{if} \;\; \alpha_{f,l} \geq 0, \\ \beta_{cl} &> \beta \quad \textit{if} \;\; \alpha_{f,l} < 0, \end{aligned} \tag{D.3}$$

where $\beta_{cl} = \alpha_{f,l} - \frac{l_f\omega}{v_x} + \delta$ *and* $\beta = \alpha_f - \frac{l_f\omega}{v_x} + \delta$

Proof. By subtracting (D.2) from (D.1),

$$\dot{\tilde{\alpha}}_{f,e} = (a-b)(\cos\delta)(F_{yf}(\alpha_f, \mu_{\max}) - C_f\alpha_{f,l}) \tag{D.4}$$

is deduced, where $\tilde{\alpha}_{f,e} = \alpha_f - \alpha_{f,l}$. As is known, $F_{yf}(\alpha_f, \mu_{\max})$ can be expressed as $\bar{C}(\alpha_f, \mu_{\max})\alpha_f$, where $C_f \leq \bar{C}_f(\alpha_f, \mu_{\max}) < 0$. Therefore, (D.4) can be rewritten as

$$\dot{\tilde{\alpha}}_{f,e} = (a-b)(\cos\delta)(\bar{C}_f\alpha_f - \bar{C}_f\alpha_{f,l}) + (a-b)(\cos\delta)(\bar{C}_f\alpha_{f,l} - C_f\alpha_{f,l}). \tag{D.5}$$

Subsequently,

$$\dot{\tilde{\alpha}}_{f,e} = (a-b)(\cos\delta)\bar{C}_f\tilde{\alpha}_{f,e} + (a-b)(\cos\delta)(\bar{C}_f - C_f)\alpha_{f,l}. \tag{D.6}$$

is deduced. The equilibrium point of (D.6) is $\tilde{\alpha}_{f,e} = (C_f/\bar{C}_f - 1)\alpha_{f,l}$, where $C_f/\bar{C}_f - 1 > 0$ if $\alpha_{f,l} \neq 0$, otherwise, $C_f/\bar{C}_f - 1 = 0$. Thus, it can be deduced that $\text{sign}(\tilde{\alpha}_{f,e}) = \text{sign}(\alpha_{f,l})$. Combined with $\text{sign}(\tilde{\alpha}_{f,e}) = \text{sign}(\beta - \beta_{cl})$, Property D.0.1 is proved. □